CROSS-SHORE MORPHODYNAMICS OF COARSE GRAINED BEACHES AND BEACH/STRUCTURE INTERACTION: NUMERICAL MODELLING AND LARGE SCALE MEASUREMENTS

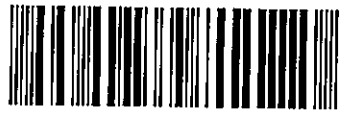

Cross-shore morphodynamics of coarse grained beaches and beach/structure interaction: Numerical modelling and large scale measurements

John Lawrence

A thesis submitted to the University of Plymouth

in partial fulfilment for the degree of

Doctor of Philosophy

School of Engineering

Faculty of Technology

October 2005

John Lawrence - Cross-shore morphodynamics of coarse grained beaches and beach/structure interaction: Numerical modelling and large scale measurements

Abstract

Coastal defence systems are implemented in many countries for the stability of coastlines and prevention of erosion and flooding. The maintenance of such schemes includes the use of 'soft' engineering techniques, which require accurate predictions of sediment transport and profile change. This thesis describes the development of a numerical model for coarse-grained cross-shore transport for use in such schemes. The model combines a hydrodynamic model based on weakly non-linear Boussinesq equations, coupled to a sediment transport module and a morphology change module. Studies have been performed on the hydrodynamic and sediment models to assess the performance of the components for this purpose.

The 1-D Boussinesq model has been validated with physical wave flume data. The model is shown to provide good predictions for shoaling and breaking waves near the coastline, and is also shown to provide good predictions for the properties of a reflected wave field. The model is then used to perform a study on the nature of wave shoaling and reflection with regard to the velocity field, and the development of the velocity skewness pattern is discussed. Recent sediment transport formulae have been reviewed, and a bed-load sediment transport model has been developed. A model for differential transport of different grain sized material has also been introduced. Developed from a river sediment model, this is able to predict sorting of grain sizes over the cross-shore profile. Results of the combined model are shown for natural plane beaches, and for beaches coupled with sea walls. The model predicts reduced erosion patterns for irregular wave fields compared to regular waves, and for mixed sediment composition sea beds compared to homogeneous sea beds. These findings show agreement with features found in previous physical studies. A series of sensitivity studies has also been performed with respect to hydrodynamic and sediment properties. The model shows a high degree of sensitivity for the profile changes to these parameters. The ability of the model to show predictions for an evolving beach profile subject to tidal water depth variation is also introduced.

Contents

List of Symbols

A	wave amplitude
A_e	wave semi orbital excursion at the bed
$A(d)$	depth dependent wave amplitude
a_t	wave trough water depth
α_ψ	critical slope correction factor
B	Boussinesq linear dispersion parameter
β	sediment angle of repose
c	wave celerity
C	dimensionless wave celerity
d	water depth
d_{50}	sediment median grain size
d_{50f}	sediment median grain size for grain fraction f
d_*	dimensionless sediment grain size
δ	wave breaker roller thickness
$E(m)$	complete elliptic integral of the second kind
ε	$=A/h$, ratio of wave amplitude and water depth
η	surface elevation
f	sediment grain fraction index
f_{wr}	wave friction factor
Φ	dimensionless sediment transport rate
ϕ	velocity potential
g	gravitational acceleration
γ	$= k.h$, scaling variable
$\gamma(z)$	slot shape function
H	wave height

h	still water depth
k	wave number
$k(d)$	depth dependent wave number
k_s	Nikuradse equivalent sand grain roughness
$K(m)$	complete elliptic integral of the first kind
λ	wavelength
m	elliptic modulus
M	momentum flux (depth integral of horizontal velocity squared)
μ	$=(h/\lambda)^2$, square of ratio of water depth and wavelength
n	Manning's n
n	sediment porosity
n	Dean's profile shape parameter
ω	wave angular frequency
P	volume flux (depth integral of horizontal velocity)
p	pressure
q_s	sediment volume transport rate
q_{sf}	sediment fraction volume transport rate for fraction f
ρ	density of water
ρ_s	density of sediment
θ	Shields parameter
θ_{cr}	critical mobility value of Shields parameter
S_u	velocity skewness (over wave period)
σ	scale transform variable
σ_u^2	velocity variance (over wave period)
t	time
T	wave period
T	scaled time variable

τ	scale transform variable
τ_b	bed shear stress
τ_{cr}	critical bed shear stress
u	(horizontal) velocity
$\overline{u}$	period mean velocity
$\hat{u}$	depth mean velocity
$\check{u}$	depth mean velocity excluding wave roller
u_b	bed velocity
u_*	friction velocity
w	vertical velocity
x	cross shore distance, horizontal space coordinate
X	scaled horizontal space coordinate
Y	Dean's profile dissipation parameter
Ψ	Boussinesq dispersion term
ψ	angle of local bed slope
z	vertical space coordinate
Z	elevation of sea bed
ζ	transform coordinate

List of Figures

Acknowledgements

I would like to thank Professors Andrew Chadwick and Chris Fleming for their support and encouragement over the years.

I would also like to thank Dr. David Simmonds for helpful discussion and advice.

I am grateful to Dr. Charlie Obhrai and Dr. Francis Ting for the use of their data.

Authors declaration

At no time during the registration for the degree of Doctor of Philosophy has the author been registered for any other University award.

The study was partly financed by the Engineering and Physical Research Council under grant award GR/L 82625.

Relevant scientific seminars and conferences were attended at which work was often presented. In the course of this work journal and conference papers have been prepared for publication.

Word count of main body of thesis: 15,391

Signed 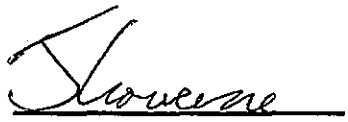

Date 24/7/06

Journal papers published

Ozanne,F., Chadwick,A.J., Huntley,D.A., Simmonds,D.J., and Lawrence,J., 2000. Velocity predictions for shoaling and breaking waves with a Boussinesq-type model, *Coastal Engineering*, **41**: pp361-397.

The author contributed the model validation for velocity profiles and velocity statistics.

Lawrence,J. and Chadwick,A.J., 2005. Modelling wave reflection on sloping foreshores with sea walls, *Proceedings of the ICE - Maritime Engineering*, **158**: pp15-24.

Karunarathna,H., Chadwick,A.J., and Lawrence,J., 2005. Numerical experiments of swash oscillations on steep and gentle beaches, *Coastal Engineering*, **52**(6): pp497-511.

The author implemented the swash zone boundary for the model.

Conference papers presented

Lawrence,J., Chadwick,A.J., and Fleming,C., 2001. A phase-resolving model of sediment transport on coarse grained beaches, *Coastal Engineering 2000*, Proceedings of the 27th International Conference, Vol. 1.

Lawrence,J., Karunarathna,H., Chadwick,A.J., and Fleming,C., 2003. Cross-shore sediment transport on mixed coarse grain sized beaches: Modeling and measurements, Smith, J. M. *Coastal Engineering 2002: Proceedings of the 28th International Conference, Vol 3*, pp2565-2577. Cardiff, World Scientific.

Lawrence,J., and Chadwick,A.J., 2005. Scour of mixed beaches near a sea wall: cross shore morphodynamic modelling and measurements. *Proceedings of the Coastal Dynamics Conference (in press)*

1. Introduction

1.1. Background

The current philosophy of the coastal engineering profession for the construction and maintenance of coastal defence systems is to use soft engineering techniques where appropriate. In the UK, and elsewhere, increasing use is made of coarse grained sediment (shingle) to replenish eroding beaches, often in conjunction with groynes or breakwaters. Accurate, predictive models for both long-shore and cross-shore sediment transport are therefore needed for the use of such systems. Beach failures often occur during storm events, so the behaviour of a beach system during a storm is of particular interest.

Most numerical models used to predict cross-shore beach evolution have concentrated on sand sized sediment. However, the particular properties of a shingle beach have a number of consequences for the processes of sediment transport, which mean that the sediment transport characteristics of a shingle beach are very different to those of a sand beach. Most notably, shingle can support a steep gradient (frequently as steep as 1:8) which allows waves to progress much closer inshore before breaking. Consequently, energy dissipation through breaking is concentrated over a much narrower region than on a sand beach. On plane beaches this results in an unsaturated breaker zone and a swash zone of similar width to the surf zone (see e.g. Baldock *et al.*,1998). Accordingly, the sediment transport within the swash zone is of more significance on a shingle beach than on a sand beach.

Where a beach is terminated by a sea wall, there will be no swash zone, but still a narrow breaker zone. To reliably simulate the movement of sediment under these conditions, it is first necessary to have a sufficiently accurate hydrodynamic description of the motions of breaking waves. The wave model must then drive a mobile sediment model to determine the beach morphological evolutions for a particular case.

Earlier morphology models were simple empirical fits of beach profile to an equilibrium shape. Bruun, (1954) found the general shape of

$$h = Yx^n \tag{1}$$

where h is the sea bed level and x is the cross shore distance from the still water line, for two parameters Y,n. This profile was later confirmed by Dean, (1977), who found the best fit for this profile was obtained using n = 2/3, with Y as a sediment dependent dissipation parameter.

This concept was then extended to consider in an empirical manner the evolution of the beach profile towards the equilibrium. Kriebel and Dean, (1985) developed a time-varying model where the cross shore transport rate was a function of the deviation of the wave dissipation rate from its equilibrium value. As time evolved, this model was found to converge onto Dean's profile. Larson, (1988) was able to extend this concept to include barred profiles. Such models can be used to evaluate damage from storms of a limited duration.

The next generation of models is the so-called *process based* model. These account for individual physical processes involved in morphological change. The first group of these models relied on phase-averaged numerical wave models for hydrodynamic information, rather than considering detailed intra-wave behaviour. Five such models are reviewed by Roelvink and Brøker, (1993). Phase-averaged models must treat long waves and wave asymmetry in an approximate manner. These earlier models also had poor descriptions of waves on steep slopes and did not incorporate swash processes.

Later process-based models have sought to improve the wave-sediment representation by explicit determination of quantities, rather than using averaged properties. A more recent model is given in Rakha *et al.*, (1997), which includes a model of an evolving, variable thickness boundary layer. The majority of effort in this field however has still been in the direction of sand transport.

A particular feature of most coastlines in the UK is the existence of significant tidal ranges. An equilibrium profile does not really exist, as the sea bed is continually moving to adjust to the present tidal height. Sea levels may also be affected by storm surges. Therefore a model should seek to incorporate long term sea level adjustments in its predictions.

A predictive tool for engineers must be convenient to use. One measure of convenience is the time taken for a simulation. Therefore one goal of this study is to develop a model that can be run in a relatively short time. In this thesis the development of a coarse-grained sediment transport model in conjunction with a phase resolving hydrodynamic model is presented. The model is intended to simulate beach beviour during a nominal storm/tide event.

1.2. Hydrodynamics

Various techniques have been investigated in recent years to develop the understanding of near-shore wave fields. Approaches that study the depth-mean flow include the use of the non-linear shallow water (NLSW) equations as used by Glaister, (1987), Dodd, (1998), and Hudson *et al.*, (2005), and the Bousssinesq equations (e.g. Madsen *et al.*, (1991), Schäffer *et al.*,1993, Madsen *et al.*,1997a, Kennedy *et al.*,2000). Studies of the full vertical flow include those using a Navier-Stokes solver, (e.g. Kothe *et al.*,1991 and Barr *et al.*,2004) and more generally, approximate solutions of the Laplacian potential flow may be found, such as the Local Polynomial Approximation (e.g. Kennedy and Fenton,1997).

Each of these types of solver has its own limitations. The NLSW equations for example are only useful inside the breaker zone, and have poor dispersion characteristics. Boussinesq equations of low order can be computationally cheap to solve, but lose accuracy in highly non-linear situations (such as close to the breaker line). Higher order Boussinesq equations (e.g. Wei *et al.*, (1995), Madsen *et al.*, (2002)) are more

accurate but expensive. Navier-Stokes solvers and potential flow solvers again provide higher accuracy, but are computationally even more expensive.

In fact, Boussinesq, (1872) first introduced his equations a number of years ago. The equations are derived by incorporating low order dispersive effects in shallow water wave propagation. The first numerical implementation however was not until Peregrine, (1967). Abbott and Rodenhuis, (1972) studied the sensitivity of the equations to numerical errors, and established the need for high accuracy difference schemes. Subsequently, Abbott *et al.*, (1978) and Abbott *et al.*, (1984) introduced a third order accurate scheme for a modified version of Peregrine's equations. Initial tests of these equations against analytical solutions and experimental data were also made, such as Abbott *et al.*, (1978) and Madsen and Warren, (1984). These showed satisfactory performance for the prediction of wave height for wave shoaling, and also in 2D models, refraction and diffraction. Accordingly Boussinesq equations have now been used for many years for the simulation of harbour conditions due to incident waves.

The study of wave-wave interactions in Boussinesq equations was first made by Freilich and Guza, (1984). They derived a set of spectral evolution equations from the original Boussinesq equations, that contained quadratic interaction terms. These terms allowed energy transfer through the wave spectrum over short distances in shallow water. Tests of this model showed that the evolution of power spectra of shoaling waves could be accurately predicted.

Early versions of Boussinesq equations were only weakly nonlinear, and only applicable for relatively long waves, and significant effort has been made in extending the applicability of the equations into shorter waves/deeper water Such efforts include Witting, (1984),McCowan, (1987), Madsen *et al.*, (1991) and Nwogu, (1996). Boussinesq equations may be derived for different choices of velocity variable, and a 'tuning' process may be applied to making this choice to make these deep water extensions. Dingemans, (1997) gives a good discussion of this process. Improved deep water performance is also

obtained by manipulation of the higher order terms of the equations, and again applying a 'tuning' process.

More recently, higher order Boussinesq equations have been obtained by retaining more terms of the dispersive effects. Examples may be found in Wei and Kirby, (1995), Gobbi and Kirby, (1999), Agnon *et al.*, (1999) and Madsen *et al.*, (2002). Gobbi and Kirby introduce a second velocity variable, thus considering some variation in the vertical profile, and Agnon *et al.*, (1999) decouple the equation system into separate linear and nonlinear problems. Each improvement introduces more dependent variables to the equation set and therefore requires the use of more computational resources to provide a numerical solution.

Ozanne, (1998) implemented a model after Madsen *et al.*, (1991), and showed that while a low order model, it provided good representation of wave energy transfer in low order harmonics. Ozanne *et al.*, (2000) subsequently showed the model provided good predictions of velocity statistics in the surf zone. This model was therefore chosen for this study as a base for a sediment transport model. This model has dispersion properties that are generally acceptable in the water depths considered. The numerical scheme of this model is also simple enough for the simulation of long periods of wave actions in a computationally acceptable time. Continual advances in computer speed may be expected to allow the use of the higher order models in a similar manner before long.

1.3. Sediment transport

The motion of sea bed sediments under wave action has also been the subject of much study over the years. Bagnold, (1963) suggested the immersed weight bedload sediment transport rate in a stream flow was proportional to the time averaged energy dissipation rate. In oscillatory flow this may actually be restated that the sediment transport rate is proportional to the energy dissipation rate times the ratio of the net current velocity and the wave orbital velocity. Inman and Bowen, (1963) found the transport over a rippled bottom was rather more complex than this, probably due to phase

relationships between the waves and the sediments. However, the model has still been useful, with extensions by Bailard and Inman, (1981) and Bailard, (1981) in the study of longshore transport. Later McDowell, (1989) incorporated a fuller treatment of bed friction coefficient, bed shear stress, particle properties and unsteady flow properties. Chadwick, (1991) used this theory in a numerical model of wave driven sediment transport. All such energetics models however rely on a coefficient of proportionality between the dissipation rate and the transport rate, which can only be determined empirically.

Previously, Shields, (1936) studied the mobilisation of sediment particles and introduced the well known mobility parameter. This work was parameterised and also extended for very fine grains by Soulsby and Whitehouse, (1997). Various transport formulae have been proposed, from Meyer-Peter and Müller, (1948) to Engelund and Fredsøe, (1976), to Nielsen, (1992) as examples. These all derive a transport rate from the difference of the flow Shield's parameter to the critical Shield's parameter. Such formulae require a calculation of bed shear stress to determine the Shield's parameter.

In fact, the majority of these transport formulae were originally developed for steady flow in channels. To apply them to oscillatory flow such as in waves, a wave oscillatory friction formulation must be found instead of a time independent channel friction formula. Reviews of these models and others are in Fredsøe and Deigaard, (1992) and van Rijn, (1993). A good summary also exists in Soulsby, (1997).

Another feature of earlier models is that they are formulated for a homogeneous mix of sediment. In reality, sediment grains of a variety of sizes may be present in a sea bed. Studies of steady flow in river channels have explored the differential transport rates that occur when such a mixed sediment exists. An early example is found in Armanini and Di Silvio, (1988). Another study of the differential flow rates is found in Pender and Li, (1995) and an example of a numerical model of channel mixed sediment transport is found in Pender and Li, (1996). The different sized sediment fractions have separate (and varying) sediment flow rates. Modelling the fractions individually then allows numerical sediment sorting, which determines the time-varying composition of the sediment mix.

More information is available in Kleinhans and van Rijn, (2002). Since the mixed sediment formulae are derived from the homogeneous channel formulae described above, it is expected that they may extend to oscillatory flow in the same way. The development of mixed grain models in coastal studies is desirable, and such an approach is made in this thesis.

In general, sediment may be transported in two modes. The first mode is the movement of sediment particles in contact with the bed, and is known as *bed load*. This mode has a fast response to the hydrodynamic motions. The second mode is the transport of particles moving through the water column, and is known as the *suspended load*. One characteristic that governs this mode is the *fall velocity* of the sediment, and lighter sediments, having a lower fall velocity will spend more time in suspension. This can lead to sediment being mobilised while the fluid moves in one direction, but then being actually transported after the fluid changes direction. This study is concerned with coarse grained sediments, which are sufficiently heavy that no suspended load transport occurs.

Since shingle beaches sustain a steep beach face, the sediment transport procedures are further modified by the beach slope. Material close to the angle of repose is likely to move down the slope more readily than material moving across a horizontal surface, because of the assistance of gravity. Similarly, movement up a slope is retarded by the same process. This can be modelled by a variation in the critical fluid stress required to move a sediment particle, as found in Soulsby (1997). Material lying on a slope of half the angle of repose may in fact see a change in the critical stress of approximately 50%. Furthermore, material deposited such that the beach slope is greater than the critical angle will slump under gravity until a stable beach slope is regained. The model also includes these processes.

Some studies of sediment transport on the beach face have suggested that in/exfiltration of sea water through the beach face may modify the sediment processes there. During infiltration events, the bed velocity may be increased, increasing the potential for sediment transport. An alternative mechanism is that excess pressure during

an uprush event may increase the effective weight of sediment, enhancing beach stability, while upwards pressure gradients during downwash exfiltration may reduce the effective sediment weight, destabilising the bed. A sufficiently large gradient may lead to bed fluidising. Experiments including Horn *et al.*, (1998),Butt and Russell, (1999), and Román-Blanco and Holmes, (2003) have studied some of these effects. Attempts to model the effect of in/exfiltration include Masselink and Li, (2001) and Acuña, (2005). Masselink and Li suggest another mechanism, that the infiltration causes a change in the velocity asymmetry, which promotes onshore sediment transport, and that this can only happen for a sufficiently high beach permeability. Acuña parameterised the infiltration by two different methods, firstly to enhance the bed friction during uprush, and secondly to include an *efficiency factor* in the sediment transport calculations, which differed for uprush and downwash stages Neither method could fully explain observed profile responses. Butt *et al.*, (2001) find there is considerable uncertainty in the relative magnitude of the various mechanisms, finding that in/exfiltration can promote beach stability or instability depending on a number of factors. In the light of this uncertainty, the present study has not considered this further.

1.4. Objectives

In this thesis the applicability of the low order Boussinesq model for driving sediment and morphology models of coarse-grained beaches is considered. This includes a study of the hydrodynamic mechanisms that drive morphology changes.

In this thesis the applicability of recent sediment studies to include a sediment transport module and a morphology module is considered. The variability of the sediment models is also explored.

In this thesis the ability of the model to respond to tidal changes is evaluated.

In Chapter 2, a description of the hydrodynamic model will be given. A theoretical basis for validating some hydrodynamic results will be set out. In Chapter 3 the performance of the Boussinesq model will be assessed against theoretical and

experimental data. The hydrodynamics of wave reflection in varying depth channels is also considered. In Chapter 4 a brief review of recent wave friction and sediment transport formulae is given. The coupling of the Boussinesq model to the sediment model is described, and the mixed sediment differential transport model is introduced. In Chapter 5, the performance of the model on plane beaches is assessed, and the sediment sorting model is introduced. In Chapter 6, the performance of the model on beaches with sea walls is assessed. The ability of the model to simulate tidal changes is also demonstrated. In Chapter 7 a final discussion and conclusions are given.

2. Hydrodynamic Modelling

2.1. Boussinesq equations

The motion of an inviscid, incompressible Newtonian fluid may be described by the Euler equations, expressing the conservation of mass and momentum. Consider a channel containing fluid. Then x,y,z are the conventional space coordinates with an origin somewhere on the still water line, h is the still water depth at a point and η is the instantaneous elevation at a point.

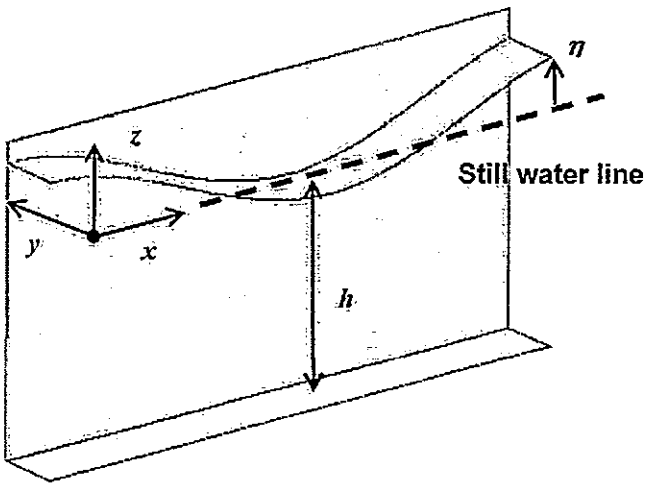

Figure 1 Axes and depths

Since flow is being considered in the cross shore (x) direction, variation in the y direction will not be considered, and the model will be considered as a 2-dimensional system.

There are many forms of Boussinesq type equations available. This is because there are multiple choices available for selecting dependent variables. The velocity variable for example may be chosen as the surface velocity, the bed velocity, or the depth mean velocity. A good discussion of the choices available is found in Dingemans (1997). Early forms of the equations, such as Peregrine (1967), were limited in application to relatively shallow water. McCowan (1987) and Madsen *et al.*, (1991) evaluated various forms of the equations for the ability to propagate waves with the correct celerity, and

found the best performance in this respect was found with the depth mean velocity as the variable of choice.

For the two-dimensional flow in a vertical plane the equations are:

$$\frac{\partial u}{\partial x}+\frac{\partial w}{\partial z}=0 \tag{2.a}$$

$$\frac{\partial u}{\partial t}+u\frac{\partial u}{\partial x}+w\frac{\partial u}{\partial z}+\frac{1}{\rho}\frac{\partial p}{\partial x}=0 \tag{2.b}$$

$$\frac{\partial w}{\partial t}+u\frac{\partial w}{\partial x}+w\frac{\partial w}{\partial z}+\frac{1}{\rho}\frac{\partial p}{\partial z}+g=0 \tag{2.c}$$

where u,v,w are the fluid velocities in the corresponding directions, t is time, p is pressure, ρ is the fluid density and g is the acceleration due to gravity.

For a model of cross-shore flow (or flow in a 2D channel) on a horizontal bed, the full system is a free-surface problem since the upper boundary of the flow is not fixed in space. The relevant boundary conditions that must be applied are

$$w\big|_{surface}=\frac{\partial \eta}{\partial t}+u\big|_{surface}\frac{\partial \eta}{\partial x}\,\text{at}\,z=\eta \tag{2.d}$$

$$p\big|_{surface}=0\,\text{at}\,z=\eta \tag{2.e}$$

$$w\big|_{bed}=-u\big|_{bed}\,\text{at}\,z=-h \tag{2.f}$$

where η is the free surface elevation.

This leads to a highly complex system. Computational solutions of the full set of Euler equations are computationally expensive. To reduce expense, a method of reducing the system is sought. One approach (e.g. Kennedy and Fenton, (1997)) is to approximate the velocity profile in the vertical to a sum of a series of shape functions. This is still a complex system, but brings some advantages. To seek a faster solution, the vertical variation of the flow may be approximated by some means, and the profile then described as some function of the depth mean flow.

The vertical flow can be isolated by integrating through the vertical. Such a procedure is described by Schäffer *et al.*, (1993). It is followed here in a dimensional form. Use is made of Leibniz's rule to transform integral properties:

$$\frac{\partial}{\partial x}\int_{A(x)}^{B(x)}\Gamma(x,z)dz=\int_{A(x)}^{B(x)}\frac{\partial}{\partial x}\Gamma(x,z)dz+\Gamma(x,B)\frac{\partial B}{\partial x}-\Gamma(x,A)\frac{\partial A}{\partial x} \tag{3}$$

The scaling quantities ε, μ will also be used, where

$$\varepsilon = A/h \tag{4}$$

$$\mu = (h/L)^2 \tag{5}$$

ε, is the ratio of wave amplitude A to water depth h, and is a measure of wave nonlinearity. μ is the square of the ratio of water depth h to wavelength L, and is a measure of the degree of dispersion of the wave.

Firstly the continuity equation is integrated throughout the vertical. The boundary conditions (Equations 2.d,2.f) are applied to the resulting vertical velocities

$$\begin{aligned}\int_{-h}^{\eta}\left\{\frac{\partial u}{\partial x}+\frac{\partial w}{\partial z}\right\}dz &= \int_{-h}^{\eta}\frac{\partial u}{\partial x}dz+\int_{-h}^{\eta}\frac{\partial w}{\partial z}dz \\ &= \frac{\partial}{\partial x}\int_{-h}^{\eta}udz-u(\eta)\frac{\partial \eta}{\partial x}-u(-h)\frac{\partial h}{\partial x}+\left[w(\eta)-w(-h)\right] \\ &= \frac{\partial}{\partial x}\int_{-h}^{\eta}udz+\frac{\partial \eta}{\partial t}=0\end{aligned} \tag{6}$$

The horizontal momentum equation is similarly treated, applying all the boundary conditions. The continuity equation is used to transform quantities of $\partial w/\partial z$ to $-\partial u/\partial x$: -

$$\begin{aligned}\int_{-h}^{\eta}\left\{\frac{\partial u}{\partial t}+u\frac{\partial u}{\partial x}+w\frac{\partial u}{\partial z}+\frac{1}{\rho}\frac{\partial p}{\partial x}\right\}dz &= \int_{-h}^{\eta}\frac{\partial u}{\partial t}dz+\int_{-h}^{\eta}u\frac{\partial u}{\partial x}dz+\int_{-h}^{\eta}w\frac{\partial u}{\partial z}dz \\ &\quad+\int_{-h}^{\eta}\frac{1}{\rho}\frac{\partial p}{\partial x}dz \\ &= \frac{\partial}{\partial t}\int_{-h}^{\eta}udz+\frac{\partial}{\partial x}\int_{-h}^{\eta}u^2dz+\frac{1}{\rho}\frac{\partial}{\partial x}\int_{-h}^{\eta}pdz \\ &\quad-\frac{1}{\rho}p(-h)\frac{\partial h}{\partial x}=0\end{aligned} \tag{7}$$

If the hydrostatic pressure condition $p(z) = \rho.g(\eta - z)$ is substituted in this equation, the non-linear shallow water (NLSW) equations may be recovered. To develop the Boussinesq equations however, the vertical momentum equation is also integrated:

$$\int_z^\eta \left\{ \frac{\partial w}{\partial t} + u\frac{\partial w}{\partial x} + w\frac{\partial w}{\partial z} + \frac{1}{\rho}\frac{\partial p}{\partial z} + g \right\} dz = \int_z^\eta \frac{\partial w}{\partial t} dz + \int_z^\eta u\frac{\partial w}{\partial x} dz + \int_z^\eta w\frac{\partial w}{\partial z} dz + \int_z^\eta \frac{1}{\rho}\frac{\partial p}{\partial z} dz + \int_z^\eta g dz \quad (8)$$

leading to a pressure equation:

$$p(z) = \rho\left[g(\eta - z) + \frac{\partial}{\partial t}\int_z^\eta w dz + \frac{\partial}{\partial x}\int_z^\eta uw dz - w^2(z) \right] \quad (9)$$

It may be seen that the hydrostatic assumption of the NLSW equation is simply the first term of this expression. This in fact is assuming that all terms of vertical acceleration (which are of $O(\mu)$ or smaller) may be neglected. The NLSW equations do not admit a permanent wave solution. The phase celerity formula for these equations is $c^2 = g(h+\eta)$ which is independent of the wave number. Wave crests therefore travel faster than troughs, and a propagating wave continually steepens as it travels.

The Boussinesq equations are obtained by retaining the first acceleration term of the pressure equation,

$$p(z) = \rho\left[g(\eta - z) + \frac{\partial}{\partial t}\int_z^\eta w dz \right] \quad (10)$$

which is equivalent to retaining terms of $O(\varepsilon)$ and $O(\mu)$. An integration of the continuity equation through a vertical section of a lower layer of water results in an expression for w:

$$\int_{-h}^z \left\{ \frac{\partial u}{\partial x} + \frac{\partial w}{\partial z'} \right\} dz' \Rightarrow w(z) = -\frac{\partial}{\partial x}\int_{-h}^z u dz' \quad (11)$$

Equations 10 and 11 are substituted into Equation 7, and the following expression is now obtained:

$$\frac{\partial}{\partial t}\int_{-h}^\eta u dz + \frac{\partial}{\partial x}\int_{-h}^\eta u^2 dz + gh\frac{\partial \eta}{\partial x} + \psi = 0 \quad (12)$$

where

$$\psi = \int_{-h}^{0} \frac{\partial^2}{\partial x \partial t} \int_{z}^{0} \frac{\partial}{\partial x} \int_{-h}^{z} u dz dz dz \tag{13}$$

with all non-linear contributions to ψ being neglected. ψ is the dispersive contribution to the momentum equation.

The depth integrated velocity P and the momentum flux M are now defined:

$$P = \int_{-h}^{\eta} u dz, M = \int_{-h}^{\eta} u^2 dz = \frac{P^2}{d} \tag{14}$$

where d is the total water depth, $h+\eta$. To evaluate ψ, a uniform vertical distribution of horizontal velocity is assumed. This results in

$$\psi = \frac{h^3}{6} \frac{\partial^3 u}{\partial x^2 \partial t} - \frac{h^2}{2} \frac{\partial^3 (uh)}{\partial x^2 \partial t} \tag{15}$$

Since ψ is taken to be linear, differences between d and h are neglected, so the term may also be expressed as

$$\psi = \frac{h^3}{6} \frac{\partial^3 (P/h)}{\partial x^2 \partial t} - \frac{h^2}{2} \frac{\partial^3 (P)}{\partial x^2 \partial t} \tag{16}$$

This gives the final form of the Boussinesq Equations:

$$\frac{\partial \eta}{\partial t} + \frac{\partial P}{\partial x} = 0 \tag{17.a}$$

$$\frac{\partial P}{\partial t} + \frac{\partial P^2 / d}{\partial x} + gh \frac{\partial \eta}{\partial x} + \frac{h^3}{6} \frac{\partial^3 (P/h)}{\partial x^2 \partial t} - \frac{h^2}{2} \frac{\partial^3 P}{\partial x^2 \partial t} = 0 \tag{17.b}$$

On a horizontal bed, these equations now describe a system where a permanent progressive wave is possible. For a slowly varying horizontal bed, higher order spatial derivatives of the bathymetry may be ignored, and the system further reduces to:

$$\frac{\partial \eta}{\partial t} + \frac{\partial P}{\partial x} = 0 \tag{18.a}$$

$$\frac{\partial P}{\partial t} + \frac{\partial P^2 / d}{\partial x} + gh \frac{\partial \eta}{\partial x} - \frac{h^2}{3} \frac{\partial^3 P}{\partial x^2 \partial t} - \frac{1}{3} h \frac{\partial h}{\partial x} \frac{\partial P}{\partial x \partial t} = 0 \tag{18.b}$$

This set of equations can be shown to have a permanent wave solution. Full details of this are shown in the appendix A.1. The form of this wave may be described by the formula

$$\eta = \eta_2 + H\,\mathrm{Cn}^2\left(\frac{2K}{\lambda}(x-ct), m\right) \qquad 19$$

where η_2 is depth of water under a wave trough, H is the wave height and λ is the wavelength. Cn is the (periodic) Jacobi elliptic function and K,m are wave dependent properties as shown in the appendix. The Cn function was named *Cnoidal* by Korteweg and de Vries, (1895). Hence the waveform described by Equation 19 is now called the *Cnoidal wave*. Some examples of the wave profile are shown in Figure 2

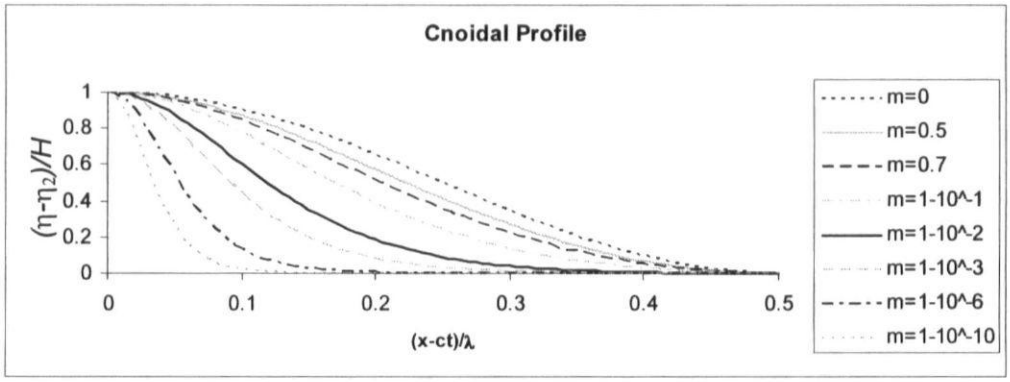

Figure 2 Cnoidal wave profiles

The existence of this permanent wave provides a basis for verifying the performance of a hydrodynamic model.

2.2. Boussinesq modelling

The Boussinesq equations now derived are only accurate to the order (ε,μ^2), and so are only weakly non-linear. A finite difference scheme is used to provide a numerical solution. Previous implementations of weakly non-linear equations have been made by Madsen *et al.*, (1991), and Wei and Kirby, (1995). Madsen *et al.*, (1991) followed the second order scheme of Abbott and Basco, (1989), and subsequent additions such as wave-breaking have later been included. The scheme is time centred implicit and spatially staggered. An update of the solution requires a single previous time-step, so its requires a low usage of computing resources.

Wei and Kirby implemented a fourth-order predictor-corrector method for the Boussinesq equations. The grid used here is non-staggered, and uses the information

from three previous time-steps to update the solution. Other more recent implementations are of higher order Boussinesq models, e.g. Wei *et al.*, (1995).In general, the use of higher order schemes or higher order equations requires the use of more computer resources, either processing time or storage.

Ozanne *et al.*, (2000) showed the predictions of the Madsen *et al.*, (1991) scheme gave acceptable predictions for velocity skewness, and as a computationally 'cheap' scheme it was used for this study. A schematic of the computational grid is shown in Figure 3

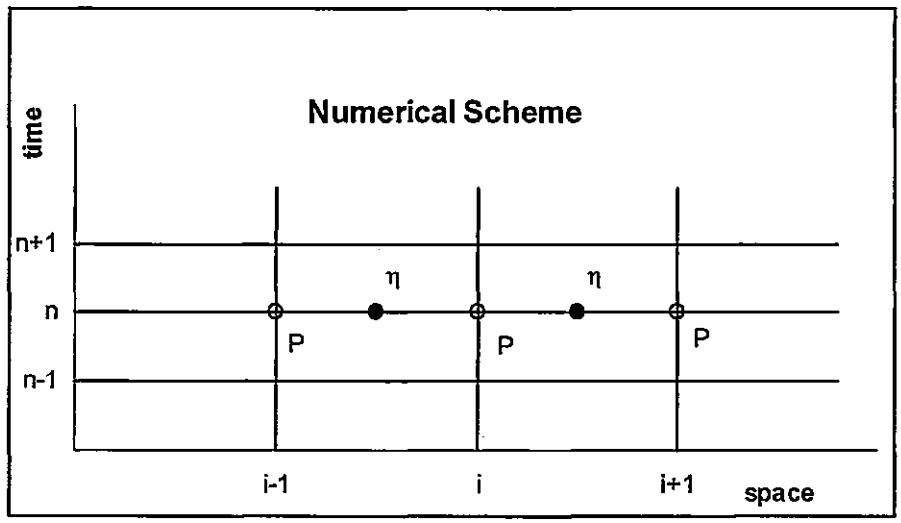

Figure 3 Computational grid

Subscript i will be used to denote the spatial discretisation, thus $x_i = i.\Delta x$, and superscript n to denote the time discretisation, thus $x^n = n.\Delta t$. The full numerical scheme corresponding to Equation 18 is then:

$$\frac{\eta_i^{n+1}-\eta_i^n}{\Delta t}+\frac{1}{\Delta x}\left(\frac{P_{i+1}^{n+1}+P_{i+1}^n}{2}-\frac{P_i^{n+1}+P_i^n}{2}\right)=0$$

$$\frac{P_i^{n+1}-P_i^n}{\Delta t}+\frac{1}{\Delta x}\left(\frac{P_{i+1}^{n+1}+P_i^{n+1}}{2}\cdot\frac{P_{i+1}^n+P_i^n}{2d_i^{n+1/2}}-\frac{P_i^{n+1}+P_{i-1}^{n+1}}{2}\cdot\frac{P_i^n+P_{i-1}^n}{2d_{i-1}^{n+1/2}}\right)+$$

$$g\frac{d_i^{n+1/2}+d_{i-1}^{n+1/2}}{2\Delta x}\left(\frac{\eta_i^{n+1}+\eta_i^n}{2}-\frac{\eta_{i-1}^{n+1}+h_{i-1}^n}{2}\right)- \qquad (20)$$

$$\frac{1}{3}\left(\frac{h_i+h_{i-1}}{2}\right)^2\frac{1}{\Delta t(\Delta x)^2}\left(P_{i+1}^{n+1}-2P_i^{n+1}+P_{i-1}^{n+1}-P_{i+1}^n+2P_i^n-P_{i-1}^n\right)-$$

$$\frac{1}{3}\frac{h_i+h_{i-1}}{2\Delta x}\frac{h_i-h_{i-1}}{2\Delta x}\frac{1}{\Delta t}\left(\frac{P_{i+1}^{n+1}-P_{i-1}^{n+1}}{2\Delta x}-\frac{P_{i+1}^n-P_{i-1}^n}{2\Delta x}\right)=0$$

In fact the Taylor series that approximate flux and elevation variation in this numerical scheme are truncated after the 2nd order terms. The error introduced by this is of the same order of magnitude as the dispersion terms. Abbott *et al.*, (1984) show that extra terms need to be added to the momentum scheme to eliminate these errors, and Ozanne (1998) finds these terms to be

$$-\frac{(\Delta t)^2}{24}\frac{\partial^3 P}{\partial t^3}-gd\frac{(\Delta x)^2}{24}\frac{\partial^3\eta}{\partial x^3}-gd\frac{(\Delta t)^2}{8}\frac{\partial^3\eta}{\partial x\partial t^2} \qquad (21)$$

which after manipulation by the long wave equation (see Mei,1989) are:

$$\left(gd\frac{(\Delta t)^2}{12}+\frac{(\Delta x)^2}{24}\right)\frac{\partial^3 P}{\partial x^2\partial t} \qquad (22)$$

This is in a similar form to the fourth term in the momentum equation in Equation 20, and may be discretised in the same manner.

The full system of equations may be written in the following form,

$$\begin{aligned} &a_k P_i^{n+1}+b_k\eta_i^{n+1}+c_k P_{i-1}^{n+1}=d_k \\ &q_{k+1}P_{i-1}^{n+1}+a_{k+1}\eta_{i-1}^{n+1}+b_{k+1}P_i^{n+1}+c_{k+1}\eta_i^{n+1}+r_{k+1}P_{i+1}^{n+1}=d_{k+1} \end{aligned} \qquad (23)$$

which may be assembled as a matrix equation. This may be easily transformed into a form with a tri-diagonal matrix and has been solved by a double sweep method (a particular implementation of Gaussian elimination.) An explanation may be found in Abbott and Basco, (1989)

The model is implicit, and nominally stable for any time step. In fact, the presence of intermediate terms in Equation 20 means that too high a time step leads to attenuation of wave energy at high μ. Further details may be found in Madsen *et al.*, (1991).

The model may be run in three modes. The offshore boundary is implemented as a source generating function as described by Kennedy *et al.*, (2000) in all these modes, to provide the wave input. The first mode replaces the near-shore boundary with a run-off zone into a numerical sponge layer. This represents a transmissive flow in an open region. The second mode consists of a shoreline tracking algorithm with a moving shoreline, representing a wave runup/down on a (gentle) beach. The third mode consists of fixed shoreward reflective (vertical) boundary, representing a reflecting flow against a solid structure such as a sea wall.

In fact the source generating boundary requires a sponge layer offshore from the model in all three modes. The sponge layer absorbs numerically all input waves, with no (or negligible) reflection. The elevation and flow fields are numerically damped by division by a series of coefficients μ_i in the sponge layer at every time step. Larsen and Dancy, (1983) derived the damping field of the form:

$$\mu_i = (\mu_{\max} - 1)\left(\frac{N+1-i}{N}\right)^p + 1 \qquad (24)$$

where μ_{max}, p are constants, N is the number of grid cells in the sponge layer, and i is an index where i=1 is the terminal boundary cell. The general form of these damping coefficients is shown in Figure 4. For the model runs in this thesis, the parameter values of 1.8, 1.3 were found to be suitable for μ_{max} and p respectively. The length of the sponge layer is required to be of the order of two wavelengths, and care should be taken when choosing parameter values.

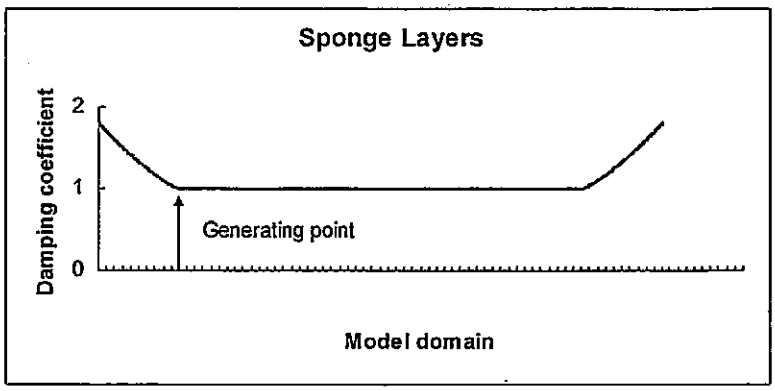

Figure 4 Sponge Layer Coefficients

For the shoreline tracking boundary, the *slot method* of Kennedy *et al.*, (2000) has been implemented. The Boussinesq equations are modified by a parameter representing the water depth at each point as follows: introduce a function γ such that

$$\gamma(z)=\begin{cases}1, & z\geq z_L \\ \varepsilon+(1-\varepsilon)e^{\beta\left(\frac{z-z_L}{z_B-z_L}\right)}, & z_L>z\geq z_B\end{cases} \tag{25}$$

where z_L is the physical sea bed depth, and z_B is the datum depth of the slot. The slot represents a region of decreasing porosity below the sea bed, and the datum is usually fixed to be the toe of the slope. γ is unity in clear water. β is a parameter that governs the rate of decrease of porosity, and ε is the minimum porosity. This function may now be used to compute an effective water depth A such that:

$$\mathrm{A}(x,y,t)=\int_{z_B}^{\eta}\gamma(z)dz \tag{26}$$

The porosity γ is now used in the continuity equation, and the effective depth A is substituted for the original depth in the momentum equation thus:

$$\gamma(\eta)\frac{\partial\eta}{\partial t}+\frac{\partial P}{\partial x}=0 \tag{27.a}$$

$$\frac{\partial P}{\partial t}+\frac{\partial P^2/A}{\partial x}+gA\frac{\partial\eta}{\partial x}+\ldots=0 \tag{27.b}$$

Near the shoreline the Boussinesq terms are also switched off, the equation set reducing to the NLSW equation. In practice damping filters are also required to prevent

the growth of spurious oscillations in the solution. Further details may be found in, e.g. Kennedy *et al.*, (2000) or Karunarathna *et al.*, (2005).

The third mode is included into the numerical model by applying the boundary condition of $P=0$ at the sea wall boundary.

2.3. Frequency dispersion improvement

Other forms of the Boussinesq equations may be developed, by using different reference velocities such as the bottom velocity u_{bed} or mean sea level velocity u_{mwl} instead of the depth mean velocity $\hat{u}$ in Equation 14. Further details may be found in Madsen *et al.*, (1991). These forms lead to the following formulation of the dispersion relation:

$$\frac{c^2}{gh} = \frac{1 + Bk^2h^2}{1 + \left(B + \frac{1}{3}\right)k^2h^2} \tag{28}$$

with B = {0, 1/6, -1/3} for equations in { $\hat{u}$, u_{bed}, u_{mwl}} respectively.

These are illustrated in Figure 5, and are compared against the exact linear wave solution

$$\frac{c^2}{gh} = \frac{\tanh(kh)}{kh} \tag{29}$$

It can be seen that errors in the dispersion relation increase with increasing kh. Since B appears to be an adjustable parameter, it may be chosen to give the closest relation between Equation 28 and the exact relation. Witting (1984) took a Padé approximant of Equation 29 and compared it against Equation 28. For the [2,2] Padé expansion of Equation 29, the form is in fact of Equation 28, with B=1/15. This line is included in Figure 5, and shows good agreement with the linear relation.

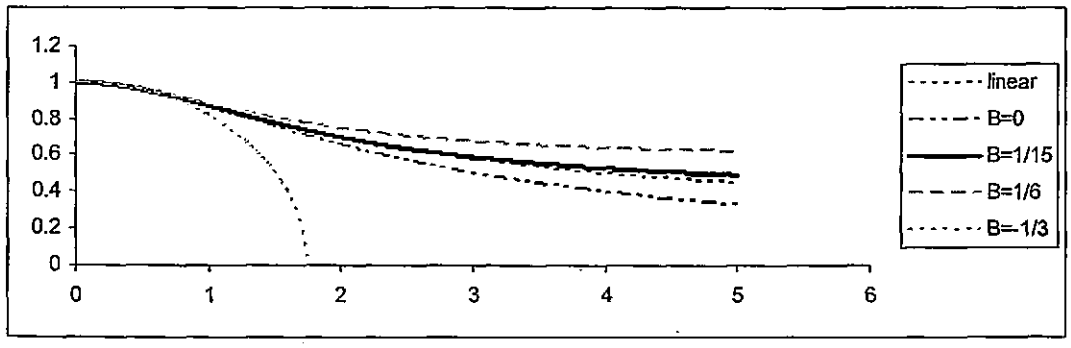

Figure 5 Comparison of dispersion relationships

Madsen *et al.*, (1991) found that the higher terms of the Boussinesq equation may be manipulated, so that the dispersion relation of the set in question may be adjusted to fit this form. The linear long wave relation

$$\frac{\partial P}{\partial t}+gh\frac{\partial \eta}{\partial x}=0 \qquad 30$$

may used to manipulate higher order terms. Differentiating twice with respect to x, and ignoring higher terms, this yields

$$\frac{\partial^3 P}{\partial x^2 \partial t}+2g\frac{\partial h}{\partial x}\frac{\partial^2 \eta}{\partial x^2}+gh\frac{\partial^3 \eta}{\partial x^3}=0 \qquad (31)$$

Adding Bh^2 times the LHS of Equation 31 to Equation 18.b yields the set of equations:

$$\begin{aligned}&\frac{\partial \eta}{\partial t}+\frac{\partial P}{\partial x}=0\\&\frac{\partial P}{\partial t}+\frac{\partial P^2/d}{\partial x}+gh\frac{\partial \eta}{\partial x}=\left(\frac{1}{3}+B\right)h^2\frac{\partial^3 P}{\partial x^2\partial t}+Bgh\frac{\partial^3 \eta}{\partial x^3}+\\&\qquad h\frac{\partial h}{\partial x}\left[\frac{1}{3}\frac{\partial^2 P}{\partial x\partial t}+2Bgh\frac{\partial^2 \eta}{\partial x^2}\right]\end{aligned} \qquad (32)$$

This new set has the dispersion relation required in Equation 28, and so a choice of B may be made in the equation to obtain the desired frequency response. The extra, higher order derivative terms are of a similar nature to the dispersive terms in the original equations, and their inclusion into the numerical scheme is made in a similar manner:

$$Bh^2\frac{\partial^3 P}{\partial x^2\partial t}+Bgh\frac{\partial^3\eta}{\partial x^3}+2Bgh^2\frac{\partial h}{\partial x}.\frac{\partial^2\eta}{\partial x^2}\approx$$
$$B\left(\frac{h_i+h_{i-1}}{2}\right)^2\frac{1}{\Delta t(\Delta x)^2}\left(P_{i+1}^{n+1}-2P_i^{n+1}+P_{i-1}^{n+1}-P_{i+1}^n+2P_i^n-P_{i-1}^n\right)-$$
$$Bg\left(\frac{h_i+h_{i-1}}{2}\right)^3\frac{1}{(\Delta x)^3}\left(\eta_{i+1}-3\eta_i+3\eta_{i-1}-\eta_{i-2}\right)^{n+1/2}- \qquad (33)$$
$$2Bg\left(\frac{h_i+h_{i-1}}{2}\right)^2\left(\frac{h_i-h_{i-1}}{\Delta x}\right)\frac{1}{2(\Delta x)^2}\left(\eta_{i+1}-\eta_i-\eta_{i-1}+\eta_{i-2}\right)^{n+1/2}$$

2.4. Wave reflection

According to linear wave theory, a travelling wave may be described by the expression $A(d)\cos(k(d).x-\omega t)$, noting that in general A and k are depth dependent. If a wave is then fully reflected from a wall, a returning wave takes the form $A(d)\cos(k(d).x+\omega t)$. The principal of superposition says the standing wave so formed may then be written as $2A(d).\cos(k(d).x).\cos(\omega t)$. Isolating time and space dependencies, the standing wave is then of the form $\chi(x,d).\cos(\omega t)$ for some function χ.

On a flat bed, A,k become constant, and so is $\chi(d)$. It is therefore apparent that at times for which $\omega t=\pi/2,3\pi/2,5\pi/2,$ the surface of the standing wave system will be horizontal. Comparable behaviour in the Boussinesq system is sought, and the Cnoidal wave is found to have a comparable standing wave solution. This solution is again the simple sum of left and right travelling Cnoidal waves. The full derivation is given in the appendix A.2.

A time series of such profiles through a half wave period is shown in figures 6 to 9, and compared to the comparable standing sinusoidal wave. The peaked nature of the Cnoidal standing wave relative to the sinusoidal wave can be seen. Figure 8 at the quarter wave period also shows the absence of the level water surface compared to the sinusoidal wave, and there is not a true nodal point for the Cnoidal type wave. Again, the existence of the standing wave profile is used as a basis for verification of the hydrodynamic model.

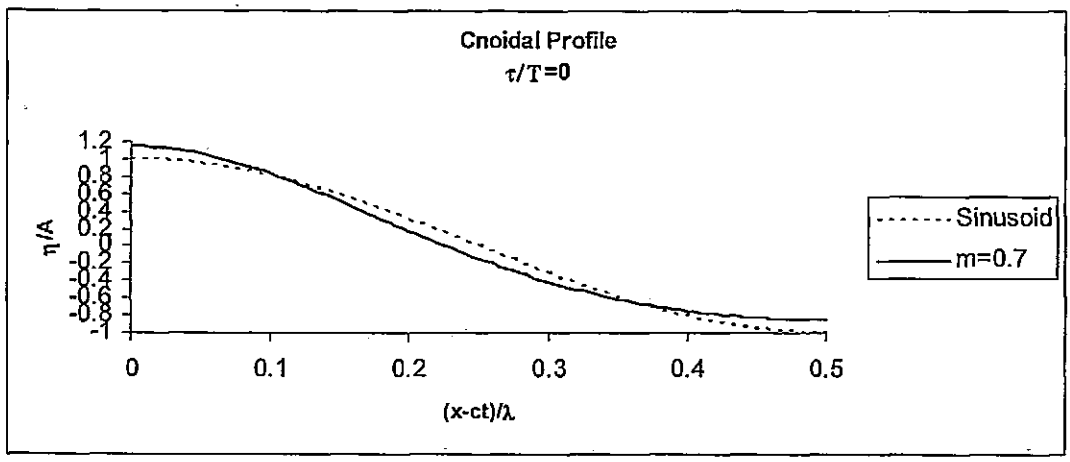

Figure 6 Comparison of sinusoidal and Cnoidal standing wave profiles (a)

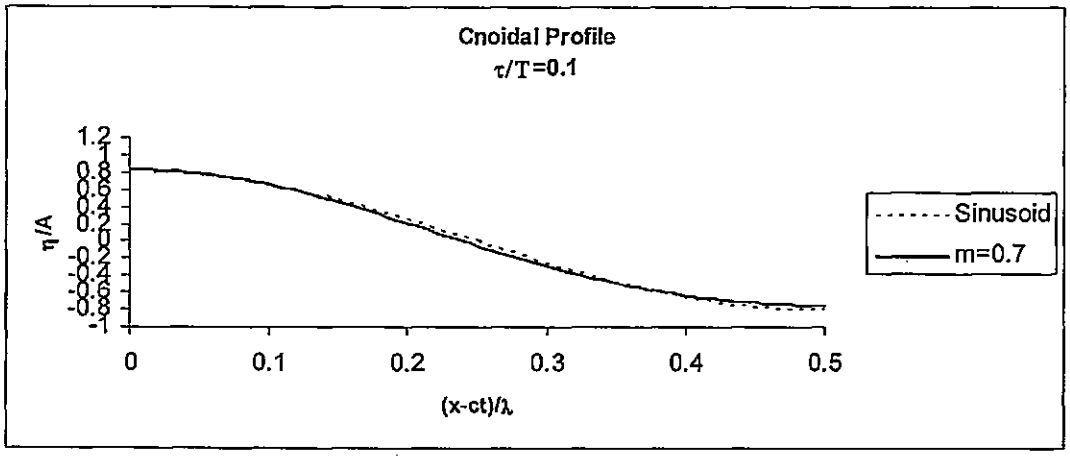

Figure 7 Comparison of sinusoidal and Cnoidal standing wave profiles (b)

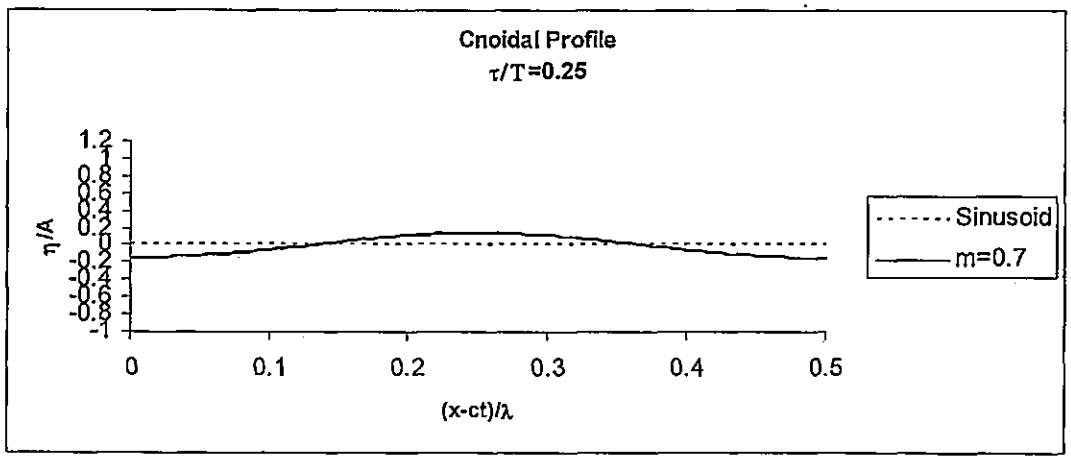

Figure 8 Comparison of sinusoidal and Cnoidal standing wave profiles (c)

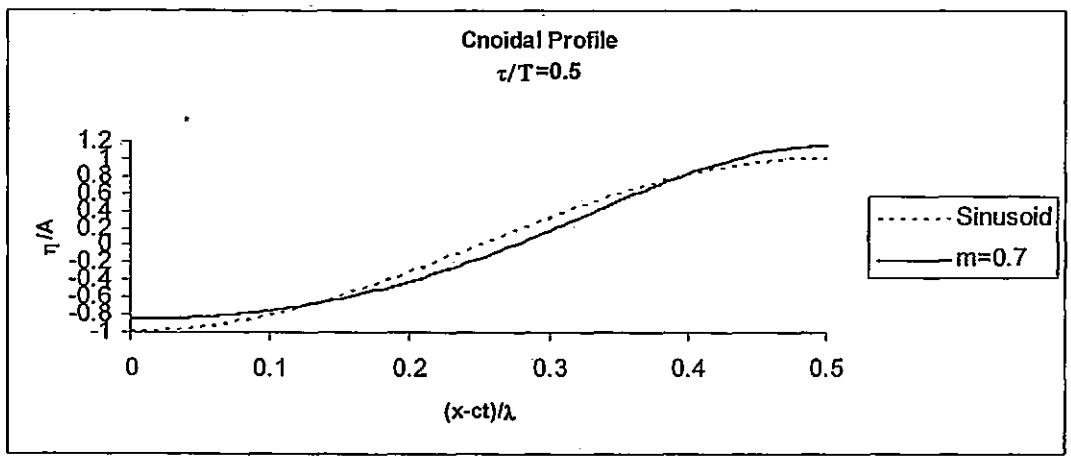

Figure 9 Comparison of sinusoidal and Cnoidal standing wave profiles (d)

2.5. Wave breaking

As natural waves shoal, the crest accelerates and the wave steepens. If the water depth becomes sufficiently shallow, the wave crest then breaks and dissipates. A simple numerical simulation of this effect is also incorporated into the model. Schäffer *et al.*, (1993) proposes a numerical roller of the following form.

The principal wave consists of a body of water moving at a uniform velocity. The broken part of the wave consists of a significantly smaller body of water, 'riding' the wave crest, and known as the *roller*. The roller travels at the wave speed. The velocity profile this indicates is given in Figure 10

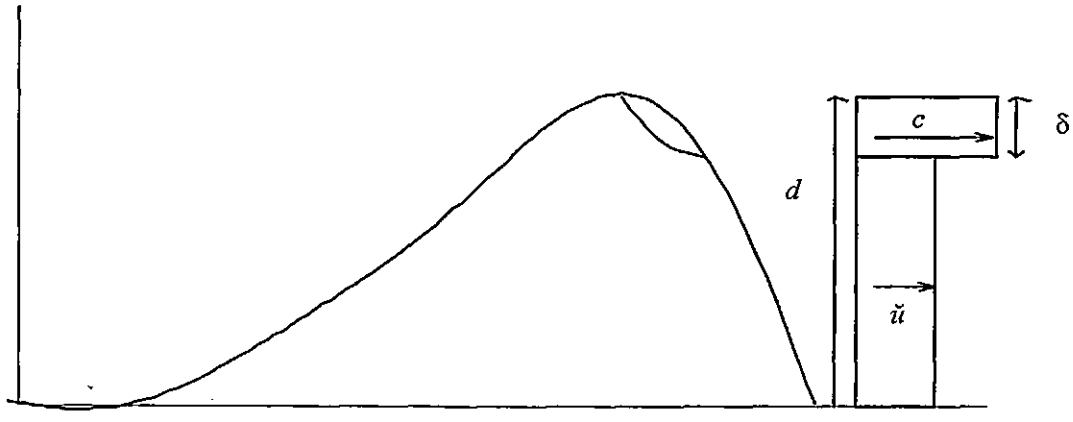

Figure 10 Schematic of breaking wave and roller profile

Since the velocity profile under the roller is constant, the depth integrated velocity and momentum flux in Equation 14 may be written as:

$$P = \int_{-h}^{\eta} u dz = \breve{u}(d-\delta) + c\delta, \tag{34.a}$$

$$M = \int_{-h}^{\eta} u^2 dz = \breve{u}^2(d-\delta) + c^2\delta \tag{34.b}$$

Rearranging Equation 34.a yields

$$u = \frac{P - c\delta}{d-\delta} \tag{35}$$

and substituting this into Equation 34.b with further re-arranging yields

$$M = \frac{P^2}{d} + R$$
$$R = \delta\left(c - \frac{P}{d}\right)^2\left(1 - \frac{\delta}{d}\right)^{-1} \tag{36}$$

and Equation 17.b may now be written as

$$\frac{\partial P}{\partial t} + \frac{\partial P^2/d}{\partial x} + \frac{\partial R}{\partial x} + gh\frac{\partial \eta}{\partial x} + \frac{h^3}{6}\frac{\partial^3(P/h)}{\partial x^2 \partial t} - \frac{h^2}{2}\frac{\partial^3 P}{\partial x^2 \partial t} = 0 \tag{37}$$

It remains to determine values for the wave celerity c and the roller thickness δ, and determine a breaking criterion.

Following Schäffer *et al.*, (1993), the model assumes breaking occurs when the local water slope reaches a threshold angle α_T. Water lying above the slope is in the roller, and δ may be determined by simple geometry. The wave continues to break while the local slope α is greater the breaking slope α_B:

$$\tan\alpha_B = \tan\alpha_0 + (\tan\alpha_T - \tan\alpha_0)e^{\left(-\ln 2\left(\frac{t-t_T}{t_*}\right)\right)} \tag{38}$$

t_T indicates the time that breaking initiated in that wave-front, and t_* governs the decay of the breaking slope. In fact, Schäffer *et al* found δ should be multiplied a shape factor f_δ to give a reasonable model. The values (α_T, α_0, t_*, f_δ) =(20°, 10°, T/10, 1.5) are recommended by Schäffer *et al* and used by Ozanne (1998).

The roller is then implemented in the numerical code by the addition of the $\partial R/\partial x$ term as follows:

$$\frac{\partial R}{\partial x} \approx$$

$$\frac{1}{\Delta x}\left[\frac{\delta_i^n+\delta_i^{n+1}}{2}\left(1-\frac{\delta_i^n+\delta_i^{n+1}}{2d_i^{n+1/2}}\right)^{-1}\left(1.3\sqrt{gh_i}-\frac{P_i^n+P_{i+1}^n}{2d_i^n}\right)\left(1.3\sqrt{gh_i}-\frac{P_i^{n+1}+P_{i+1}^{n+1}}{2d_i^{n+1}}\right)\right]$$

$$-\frac{1}{\Delta x}\left[\frac{\delta_{i-1}^n+\delta_{i-1}^{n+1}}{2}\left(1-\frac{\delta_{i-1}^n+\delta_{i-1}^{n+1}}{2d_{i-1}^{n+1/2}}\right)^{-1}\left(1.3\sqrt{gh_{i-1}}-\frac{P_{i-1}^n+P_i^n}{2d_{i-1}^n}\right)\left(1.3\sqrt{gh_{i-1}}-\frac{P_{i-1}^{n+1}+P_i^{n+1}}{2d_{i-1}^{n+1}}\right)\right]$$

Since this term does not contain any higher order derivatives, it may be included in the extended numerical model for the linearly improved Boussinesq equations, without any further treatment for the truncation error.

Strictly, this formulation is only valid for progressive waves. In a standing wave situation the wave crest no longer travels at the shallow water wave speed, and the velocity assumptions are no longer valid.

3. Hydrodynamic Application

3.1. Previous work

Much work has been done by others on the validation of Boussinesq numerical models. Madsen *et al.*, (1991) demonstrated the propagation of mono-chromatic and bi-chromatic waves with a model of the present type on a flat bed. Analysing predictions of wave elevation an error in wave celerity and group velocity of the order of 3% was obtained. Madsen and Sørenson, (1992) demonstrated the shoaling properties of the equations in the present 1D formulation, and also the comparable 2D formulation. For the 1D case an error of the order of 3% was obtained comparing the numerical model to the shoaling computed by a Stokes 1st order theory on a 1:25 slope. For the 2D case good agreement was shown with the experiment of Whalin, (1971) of wave propagation over a semi-circular shoal. Madsen *et al.*, (1997a) demonstrated the use of the wave breaking mechanism. Comparisons were made with experimental observations by Luth *et al.*, (1993) and Beji and Battjes, (1993) of mono-chromatic waves breaking over submerged bars, and by Stive, (1980) and Ting and Kirby, (1994) of waves breaking on plane shallow sloped beaches. Again, good agreement was found with measured wave elevations. Tuning of the wave-breaking parameters was often found necessary for optimum results. Madsen *et al.*, (1997b) further verified the performance of a Boussinesq model against the experiment by Mase, (1994) of bi-chromatic waves on a plane sloping beach and the experiments by Cox *et al.*, (1991) and Arcilla *et al.*, (1994) of irregular waves breaking on sloping beaches. Again, good agreement with wave elevation profiles was found, and also good agreement with statistical properties of the wave elevation. In general, the dominant energy dissipation mechanism in the surf zone is found to be from the turbulence of wave breaking, with bed friction having little effect on the wave profiles. Bed friction may be important in determining wave runup, but the experiments of Madsen *et al.*, (1997a) and Madsen *et al.*, (1997b) suggest that friction may affect maximum runup by only 3%. Bed friction is accordingly omitted from the present model.

Ozanne (1998) demonstrated further comparisons between a Boussinesq model and the experimental observations by Kraus and Smith, (1994) of regular and irregular waves breaking on a non-uniform beach. This showed good agreement of modelled and observed wave elevations, and also good agreement of depth-mean velocity statistics. Bi-spectral analysis was used to show energy transfer in low-order harmonics is well represented in a low-order model of this type. Kennedy *et al.*, (2000) presented another Boussinesq model with an alternative approach to wave breaking (represented by a vertical variation in eddy viscosity). This too has shown good agreement with experimental studies.

Most earlier validations however have concentrated on the validity of elevation predictions for shoaling waves. More recently, Ozanne *et al.*, (2000) performed comparisons with the experiment by Ting and Kirby, (1994). Good agreement of velocity statistics was found, and the model also showed reasonable estimation of the vertical velocity profile from the modelled mean velocity. Lawrence and Chadwick, (2005) demonstrated further comparisons between a Boussinesq model of reflecting waves, and the large scale experiment by Bullock *et al.*, (2004) of waves in a strongly reflecting tank. Good agreement was found for calculations of the wave elevation in the resulting wave field. Further details of these last two comparisons are shown below.

3.2. Constant channel

The first numerical experiment is to confirm the behaviour of the present numerical model by reproducing a theoretical solution of a propagating Cnoidal wave. The model was run to simulate conditions in an open channel (i.e. mode I) The channel profile was a constant water depth of 5m, with a wave height of 0.5m and a period of 10s. This corresponds to a value of m of approximately 0.75 for the Cnoidal wave. The grid spacing was 0.4m, and the time step was 0.78125s (or 1/128th of the wave period). This grid spacing and time step are chosen to provide acceptable resolution for the later implementation of the morphology model. They are comparable to those used by Madsen

et al., (1991). The wave envelope is shown in Figure 11. The permanent nature of the propagating wave can be seen.

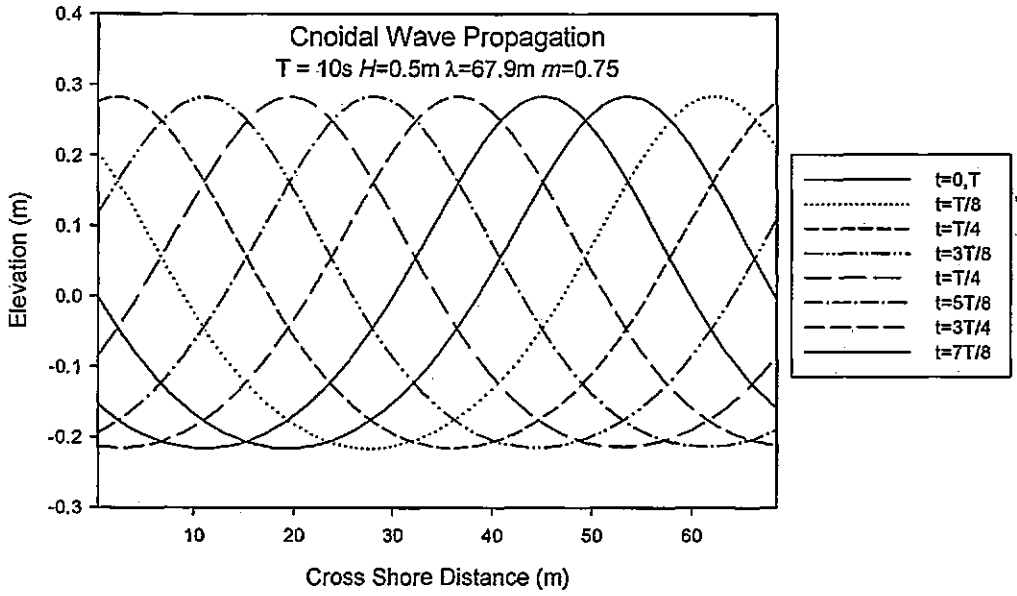

Figure 11 Cnoidal wave propagation – flat bed

A Cnoidal wave can be shown to consist of a wave at the fundamental frequency, and diminishing components of the higher harmonics. Taking a fast Fourier transform (FFT) of the model results across the channel, the fundamental frequency and the first two higher harmonics are illustrated for this case in Figure 12.

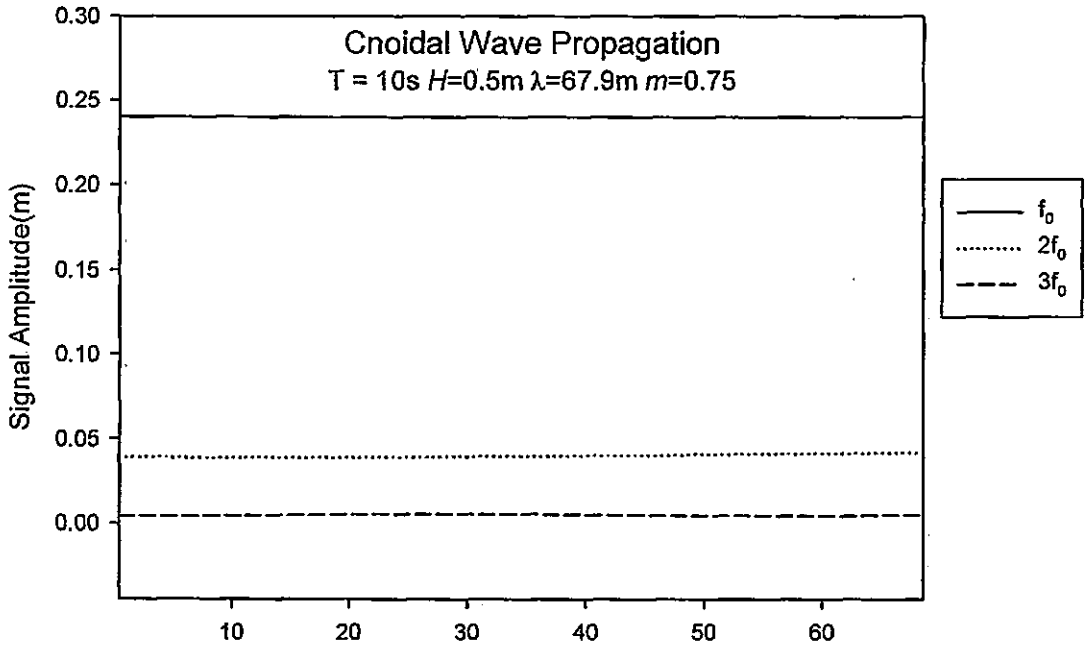

Figure 12 Frequency propagation of Cnoidal wave

The propagation of the fundamental frequency is seen to be good. There are slight variations in the propagation of the higher harmonics, but the magnitude of the variation is less than 1% of the magnitude of the fundamental frequency.

Of interest for the sediment transport properties of a simulation is the velocity skewness. As this travelling wave is of a constant form, the velocity skewness in this case is also constant. The theoretical value for this is 0.36, while the modelled value is 0.33.

3.3. Shoaling channel

Another validation of the hydrodynamic model is described in Ozanne *et al.*, (2000). The present author's contribution to this evaluation, of a comparison against the experimental data of Ting and Kirby (1994), is described here.

Ting and Kirby installed a sloping beach of gradient 1:35 in an experimental flume. Regular waves of 6s period and 10s period were then run. This was to examine the behaviour of a spilling breaker and a plunging breaker respectively.

Figure 13 shows the model performance in simulating the spilling breaker case. Here the model is being run using the slot boundary.

This figure commences at the seaward part of the slope, with wave generation occurring some 25m distant. The figure shows the cross-shore profiles of the mean water level (η_{mean}), and wave crest and trough heights ($\eta_{max}-\eta_{mean}$, $\eta_{min}-\eta_{mean}$). The agreement with wave crest and mwl measurements from Ting and Kirby (1994) is fairly good, and the discrepancy between the modelled and experimental values of maximum wave crest height is a consequence of the weak non-linearity of the Boussinesq equations. This is explained in Schäffer *et al* (1993). Figure 13 also shows the performance of the model in the swash zone by including the shore line boundary.

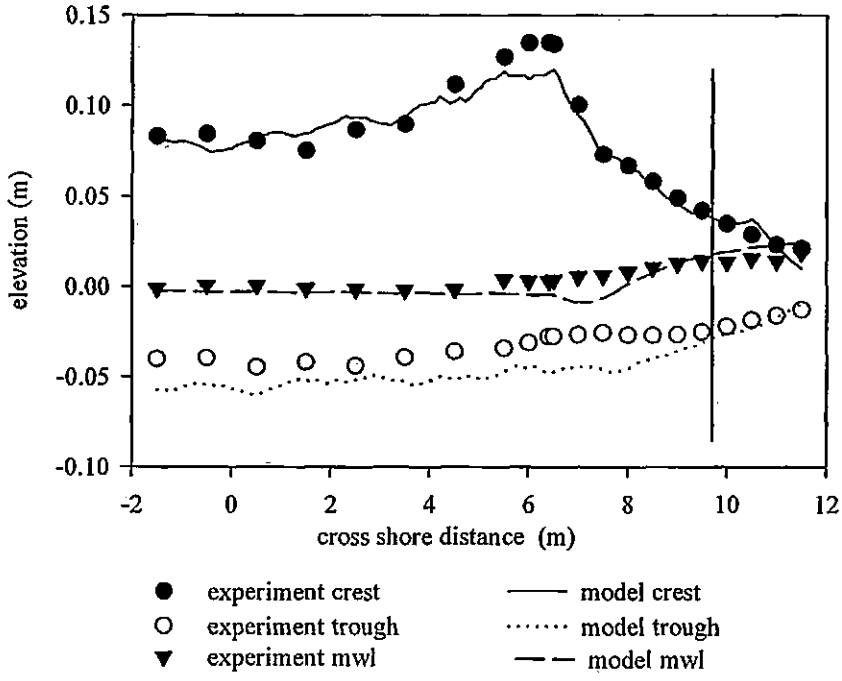

Figure 13 Model simulation of spilling breaker experiment

Figure 14 shows the surface elevation time series at the point indicated by the vertical line in Figure 13, through one wave period. At this point in the inner surf zone, the experimental skewness was calculated to be 0.61 and the modelled skewness was 0.51. The experimental and modelled kurtosis values are 1.76 and 1.65 respectively.

Figure 15 shows the velocity measurements at the same point. The experimental skewness is 0.26 and the modelled value is 0.24. The experimental and modelled kurtosis

values are 1.76 and 1.65 respectively. This demonstrates fair reproduction of the asymmetric properties of the wave, in peakedness and offshore or onshore dominant flow. If the experimental velocity is only integrated through the water column below the surface roller (estimated from the modelled roller thickness) to determine the mean, the skewness value rises to 0.31 and the kurtosis value rises to 1.82.

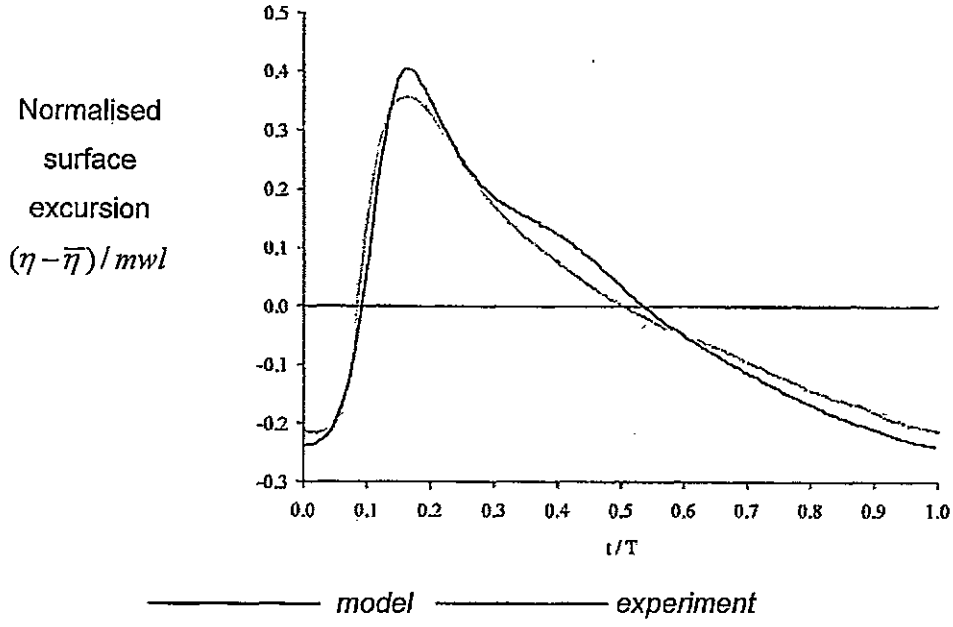

Figure 14 Elevation time series comparison – spilling breaker

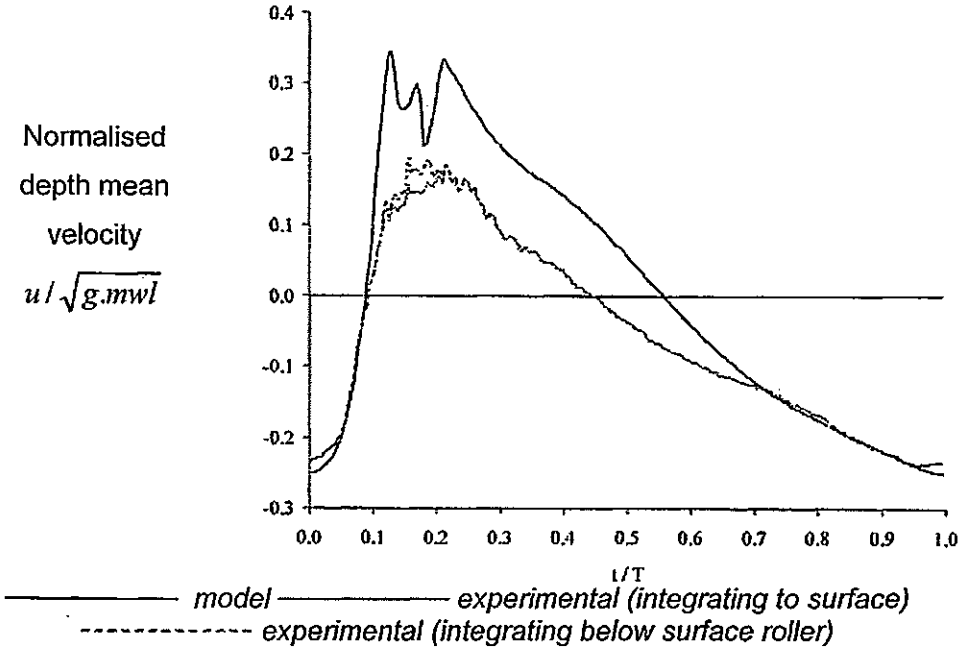

Figure 15 Velocity time series comparison- spilling breaker

In Figure 16 the cross-channel elevation results from a comparison of the model with the plunging breaker case are shown. The channel shape is identical.

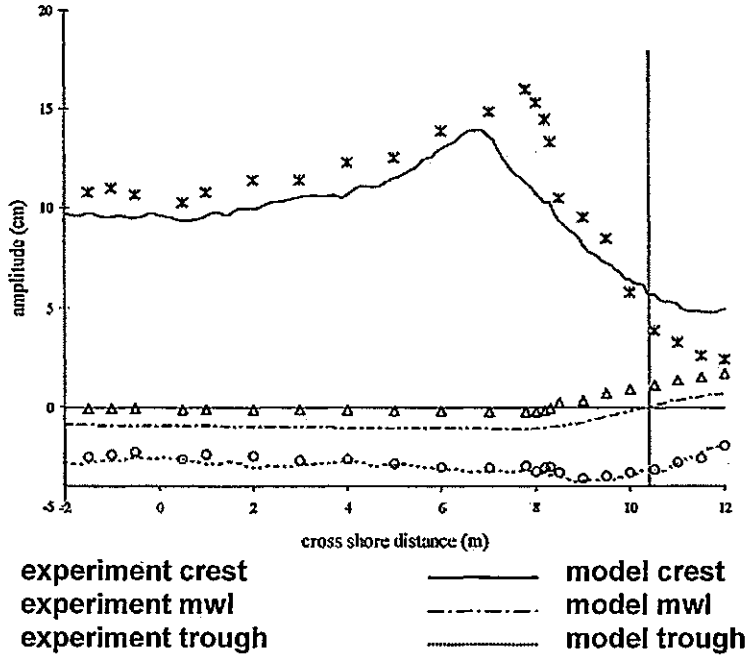

Figure 16 Model simulation of plunging breaker experiment

In this case the model was run using the sponge layer boundary. This causes a lowering in the mwl value of the model which can be seen in the figure. This is due a to

mass flux through the shoreline boundary. It was found necessary to increase the value of f_δ for this case, to reduce oscillations that were found in the surface excursion time series.

In Figure 17 the elevation series from the model and the experiment are compared, again for the point indicated with the vertical line in Figure 16. The experimental skewness for this case was found to be 0.36, while the model skewness was 0.53. The kurtosis values were found to be 2.06 and 2.5

Velocity comparisons for the same point are shown in Figure 18. The experimental skewness was 0.31 and the model skewness was 0.26. The kurtosis values were found to be 2.20 and 1.91. Again, if only the water column below the estimated surface roller is integrated, the skewness rises to 0.37 and the kurtosis rises to 2.24. Although the roller construction is more suited to a spilling breaker, the results for the plunging breaker are in closer agreement for the plunging breaker.

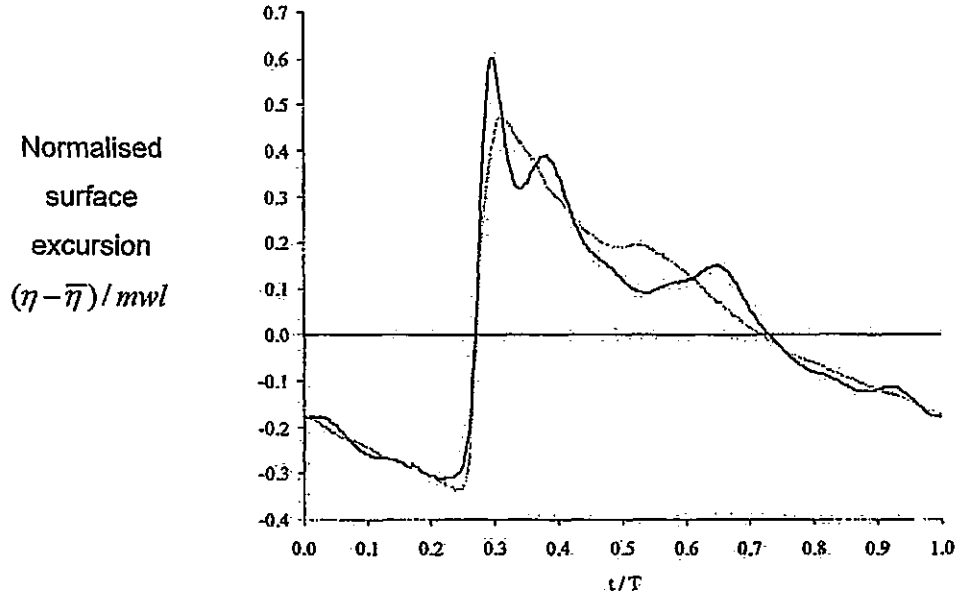

Figure 17 Elevation time series comparison- plunging breaker

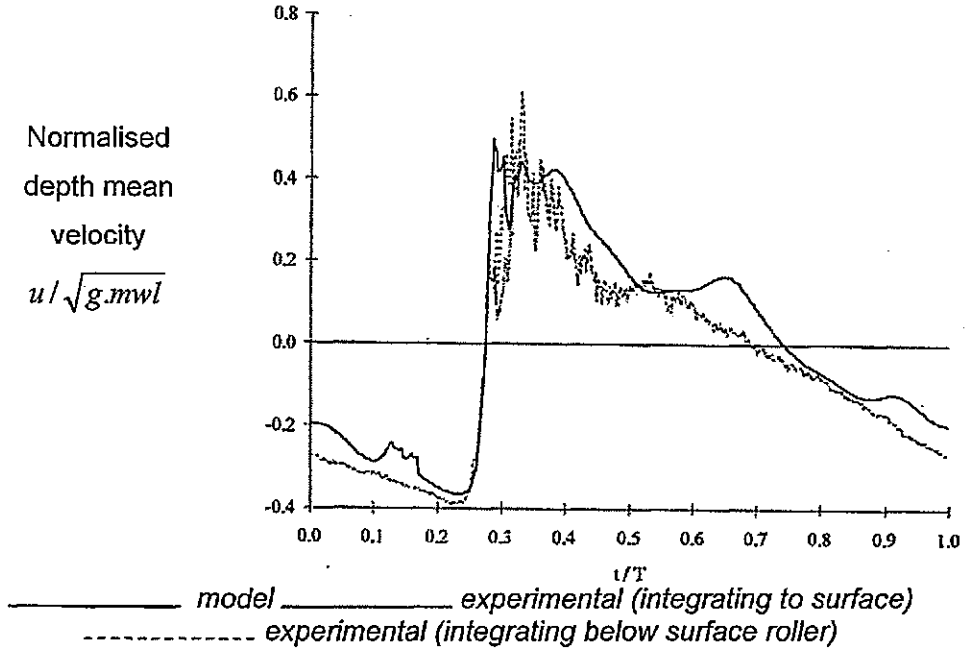

Figure 18 Velocity time series comparison - plunging breaker

3.4. Cnoidal wave reflection

The numerical model was run to simulate reflection in a flat channel with a vertical sea wall, comparable to the case in section 3.1. Again, the channel was a constant 5m depth, with a wave height of .5m and a period of 10s. The model was run to a steady state to observe the developed 'standing' wave field. The wave envelope is shown in Figure 19.

The profiles are of a similar nature to those in figures 6 to 9 The energy of the frequency components is shown in Figure 20.

It can be seen the amplitude of all the harmonics shows considerable variation. Note also that the second harmonic shows a maximum at the fundamental's minimum. In general the higher odd harmonics are aligned with common nodes, and the higher even harmonics are aligned with common-antinodes. Since this is still an idealised case, with perfect reflection, the velocities are symmetrical, and the skewness is zero.

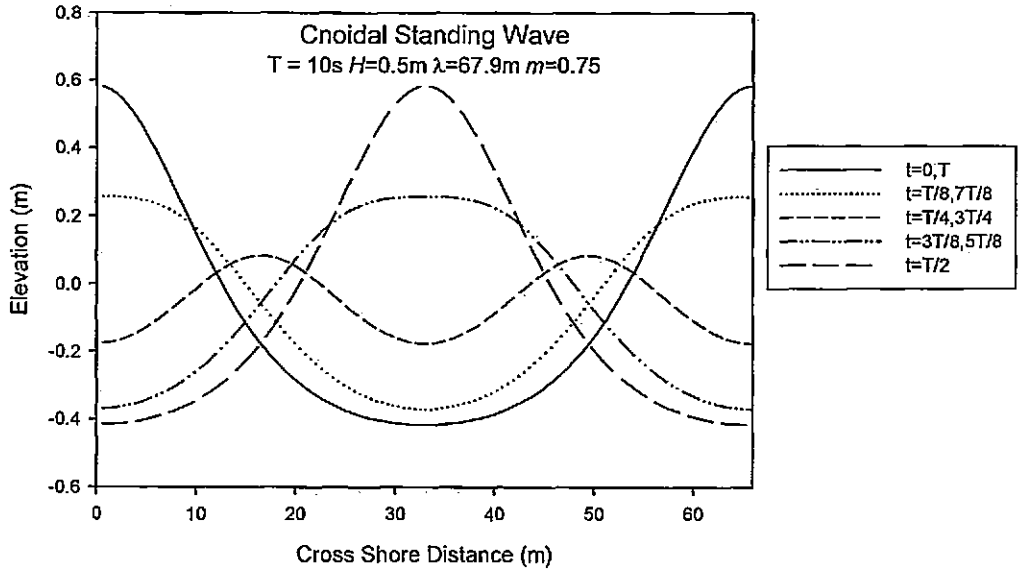

Figure 19 'Standing' Cnoidal wave profile

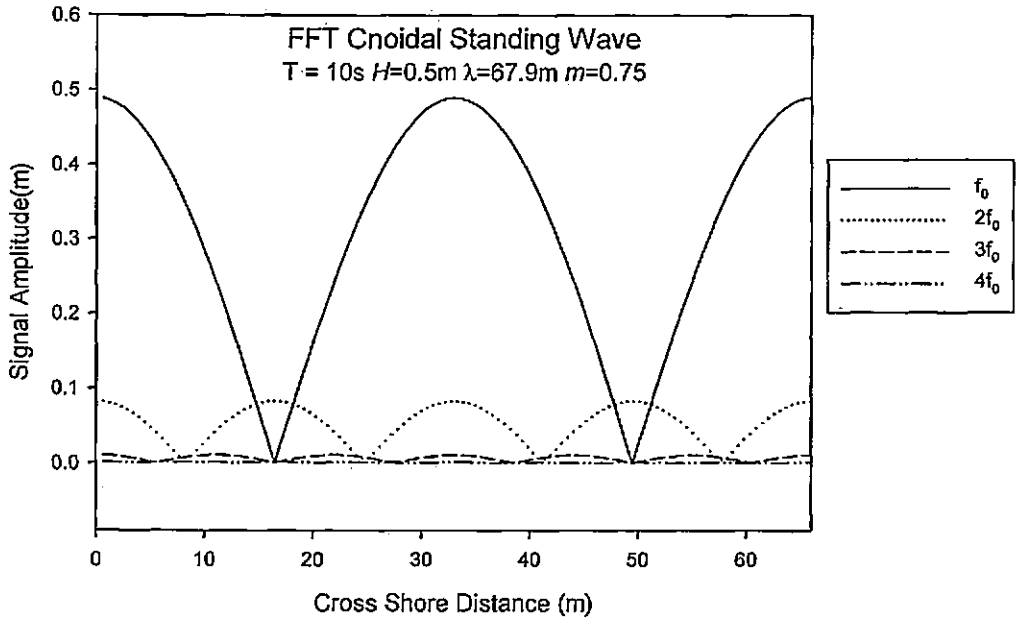

Figure 20 Frequency distribution of 'standing' Cnoidal wave

3.5. Reflecting shoreline

Another series of wave tank experiments was performed by Bullock *et al.*, (2004) in the Grosse Wellen Kanal, Hannover, Germany. A large number of wave tests were run, and some two regular wave cases have been selected as suitable for comparison with the numerical model. Figure 21 shows the physical arrangement of the wave tank.

Short packets of waves were run down the channel to investigate wave breaking on the sea wall. Since the waves are fully reflected at the wall, a quasi-standing wave field developed in the channel for a few wave periods. The incident waves were not strictly Cnoidal in form, but were composed primarily of the fundamental and the first harmonic. The nature of reflection was slightly modified by the two sloping bed sections immediately before the wall. This will be considered again later. Figure 21 shows the location of wave gauges in the flume. No velocity measurements were taken at these points however. The wave elevation data was analysed by FFT to consider the harmonic contributions to the wave field.

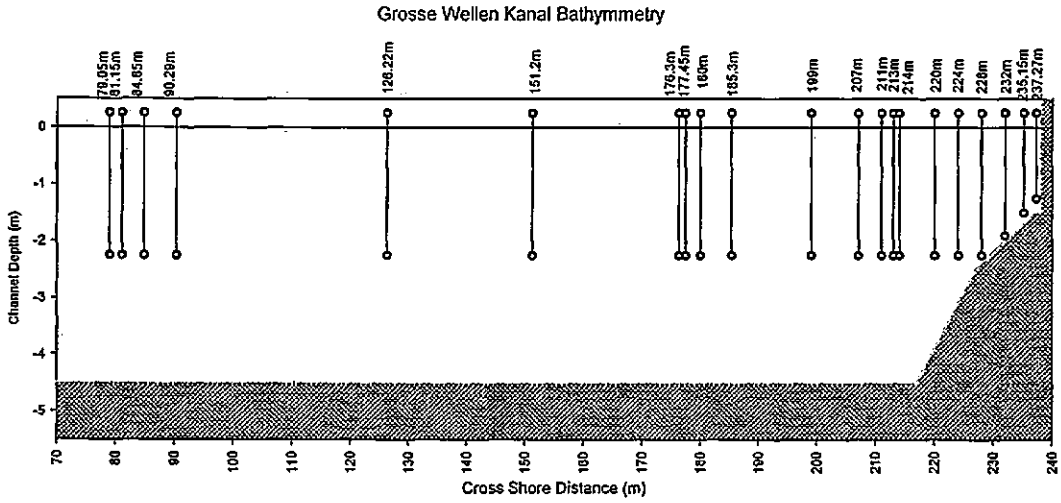

Figure 21 Schematic of GWK experiment

The numerical model was setup to match the configuration of the GWK. Wave input was at the location of the wave paddle, and corresponded to the input wave signal at the GWK. The first comparison was made with a wave sequence of 1m high 6s period waves. The elliptic parameter for a Cnoidal wave of these properties has the value 0.66. The case was designed by Bullock *et al.* to be a case with no wave-breaking. The modelled wave profile is shown in Figure 22.

While the profile is somewhat noisy, there is evidence of a standing wave in the figure. An FFT of the wave evolution is shown in Figure 23, with the comparable experimental data.

The general structure of the nodes is apparent in this figure. This is of a similar pattern to the flat channel case, but there is some modification near the sloping bed. The locations and magnitudes of these nodes and anti-nodes in the fundamental frequency are predicted fairly well by the model. The nodal structure of the second harmonic is less clear, however the general modelled magnitude of this harmonic shows good agreement with the experiment.

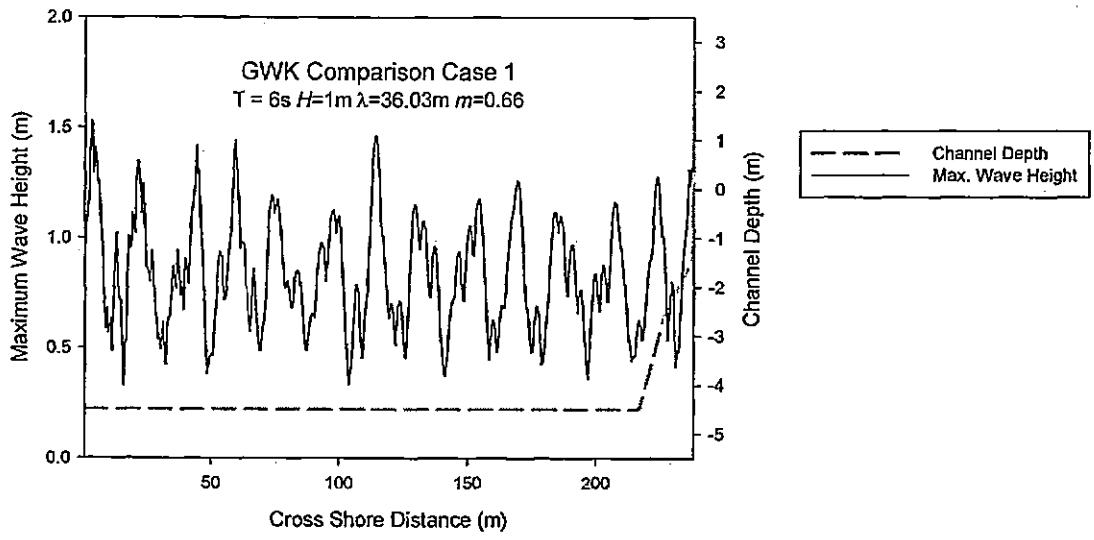

Figure 22 Elevation profile – GWK case (1)

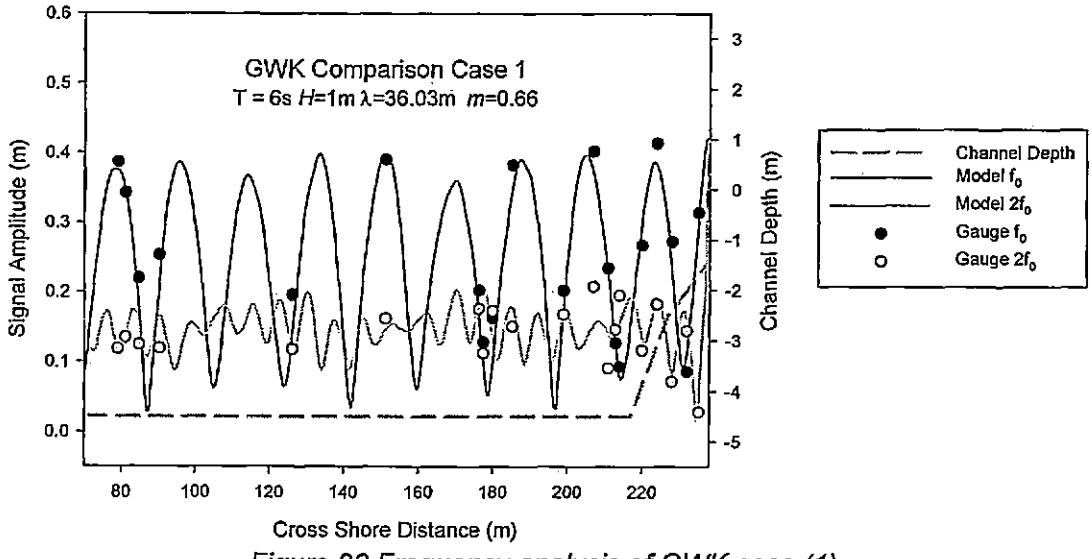

Figure 23 Frequency analysis of GWK case (1)

The second comparison was made against a similar wave but with only a 5s period. The corresponding elliptic parameter for this is 0.44. This wave then is of relatively low non-linearity. The wave profile for this is shown in Figure 24.

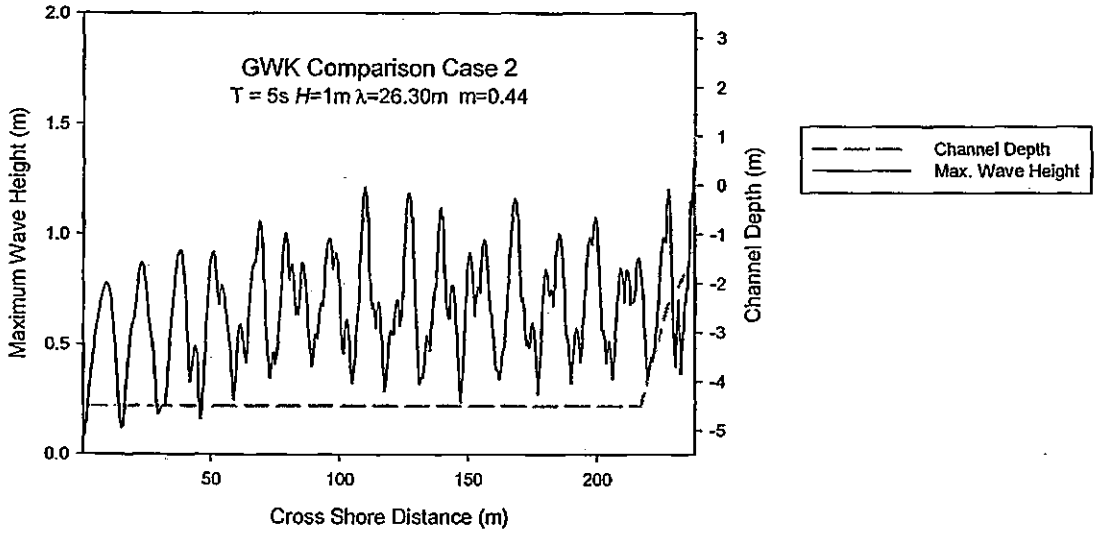

Figure 24 Elevation profile – GWK case (2)

The nodal structure can again be made out, although it is less clear than the previous case. The FFT analysis for this case is shown in Figure 25.

The model again locates the nodal structure fairly well. Agreement with the fundamental frequency amplitude is fair. The second harmonic is reproduced less clearly away from the wall, but is still fairly good overall. Since the wave has low non-linearity, the wave length of the second harmonic is now very short; a Boussinesq model is not expected to reproduce short wave dynamics very well.

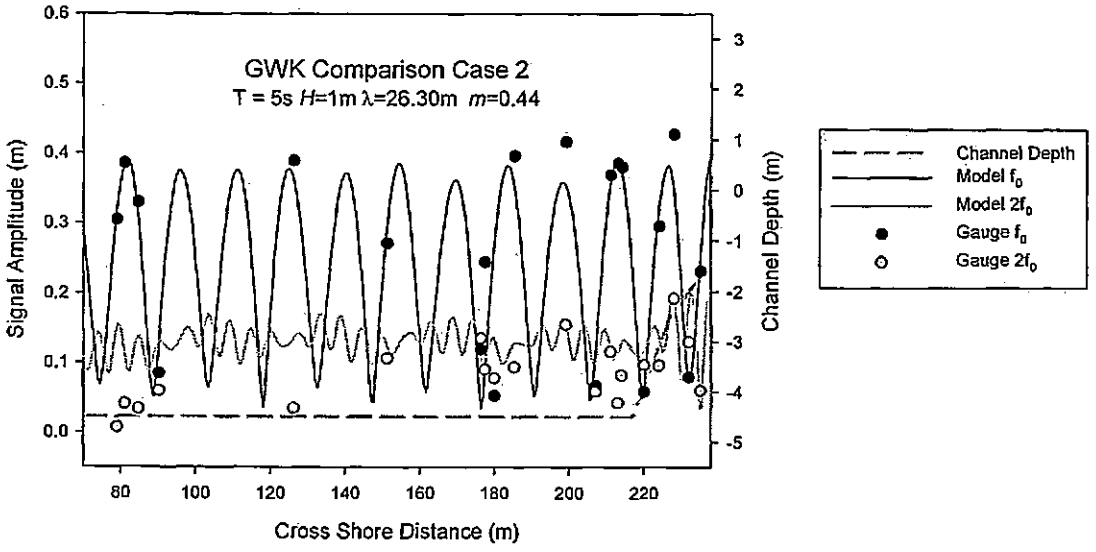

Figure 25 Frequency analysis – GWK case(2)

3.6. Wave reflection and superposition

Recalling the linear standing wave, $2A(d)\cos(k(d).x).\cos(\omega t)$. of section 2.4, the model has been applied to a study of the left and right travelling waves in the nonlinear system, and the interaction between them. Previous studies of wave shoaling have shown transformation of higher harmonics as a wave travels over a changing bed. The numerical model was used to study a shoaling wave, and then extend the situation to a reflecting wave. The initial case (case I) for this study was a channel with a flat section of 5m, rising to a depth of 3m over a constant slope. Beyond the crest the model was run into a flat channel and then a sponge layer. Slopes of gradient 1:40, 1:20 and 1;10 were studied. The wave was a Cnoidal wave of 10s period and 0.5m wave height. This corresponds to a value for the elliptic parameter of 0.75. The wave profile for the 1:40 case is shown in Figure 26.

Figure 26 shows a degree of reflection from the slope. Analysis shows the reflection co-efficient to be 2%. The Battjes empirical model for wave reflection predicts a value of 1%.

An FFT of the wave profile is shown in Figure 27. This again shows wave reflection in the fundamental frequency. The magnitude of the higher harmonics is

relatively constant until the sloping bed is reached, there is then a significant increase in this component up to the crest. Finally, the velocity skewness for this case is shown in Figure 28

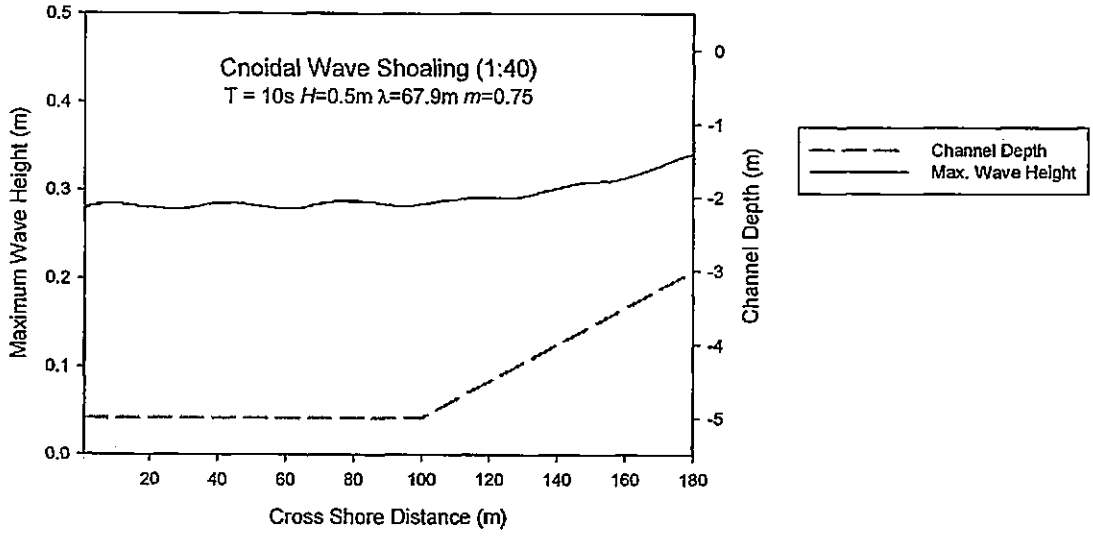

Figure 26 Cnoidal wave shoaling – 1:40 slope

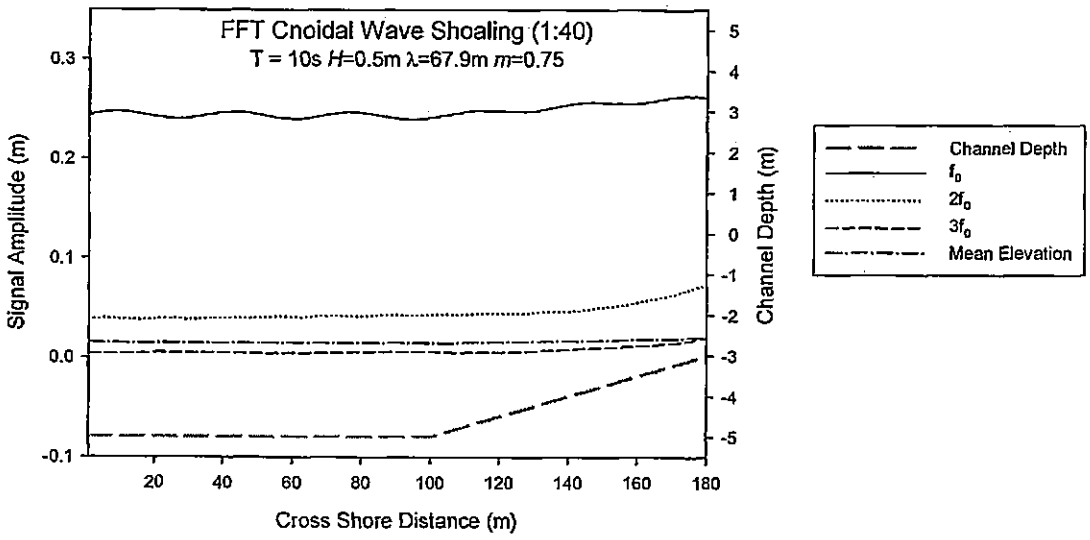

Figure 27 Frequency analysis of Cnoidal shoaling – 1:40 slope

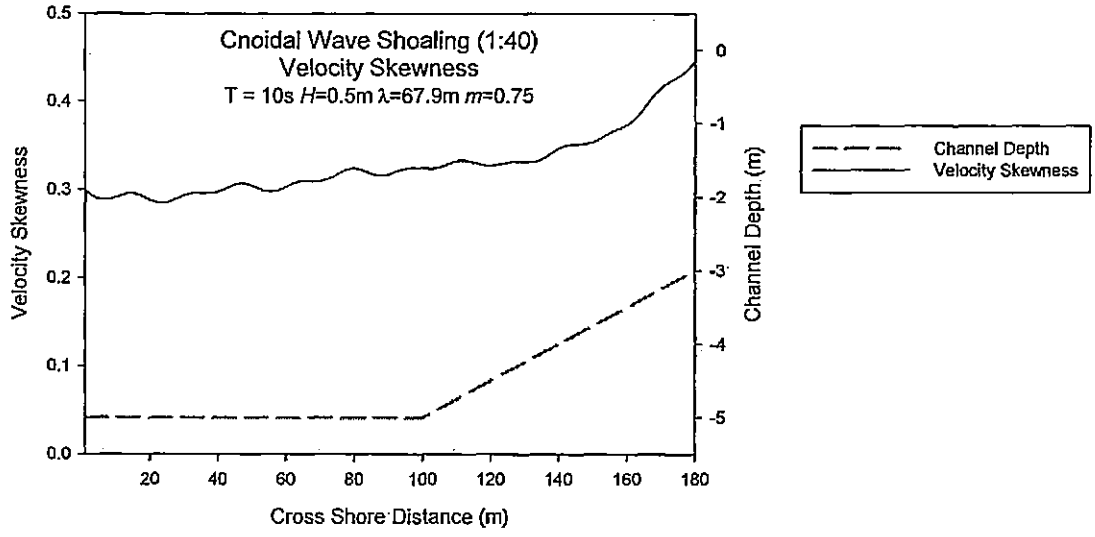

Figure 28 Velocity skewness of Cnoidal shoaling – 1:40 slope

This shows a relatively constant skewness for the flat section of the channel, with an increasing skewness as the second harmonic magnitude increases.

Figures 29 to 31 show the comparable figures for the 1:20 slope case.

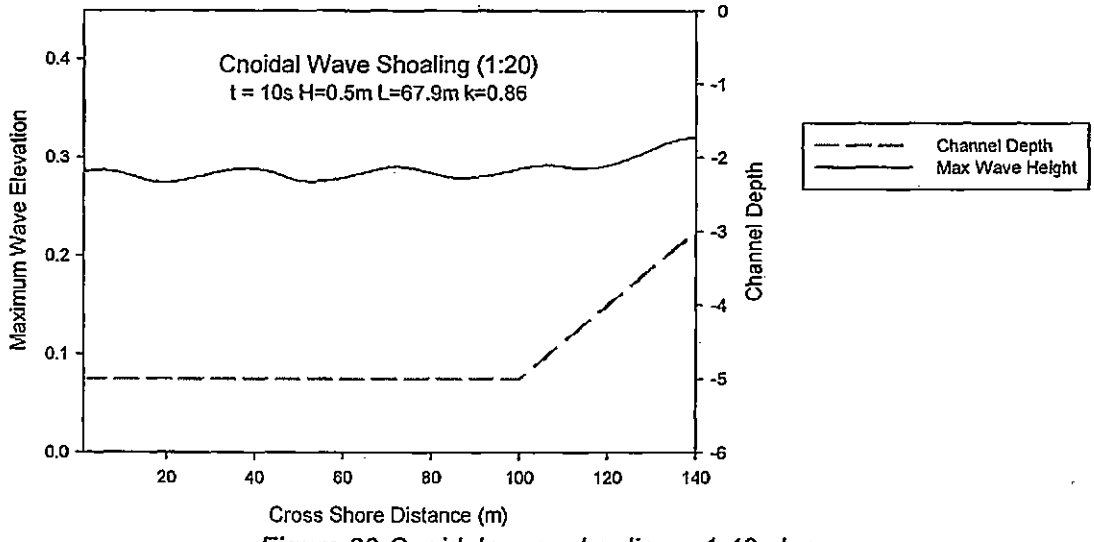

Figure 29 Cnoidal wave shoaling – 1:40 slope

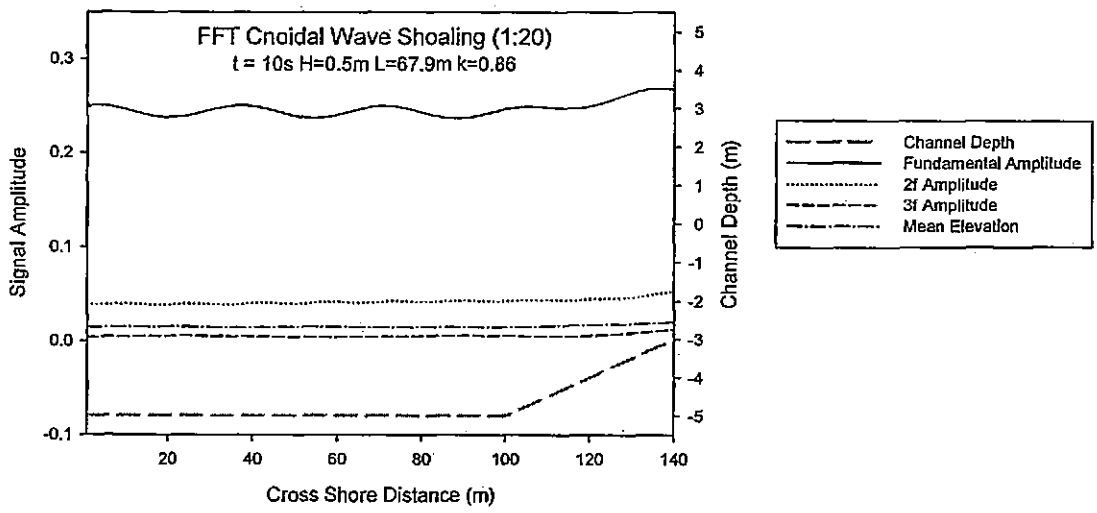

Figure 30 Frequency analysis of Cnoidal shoaling – 1:20 slope

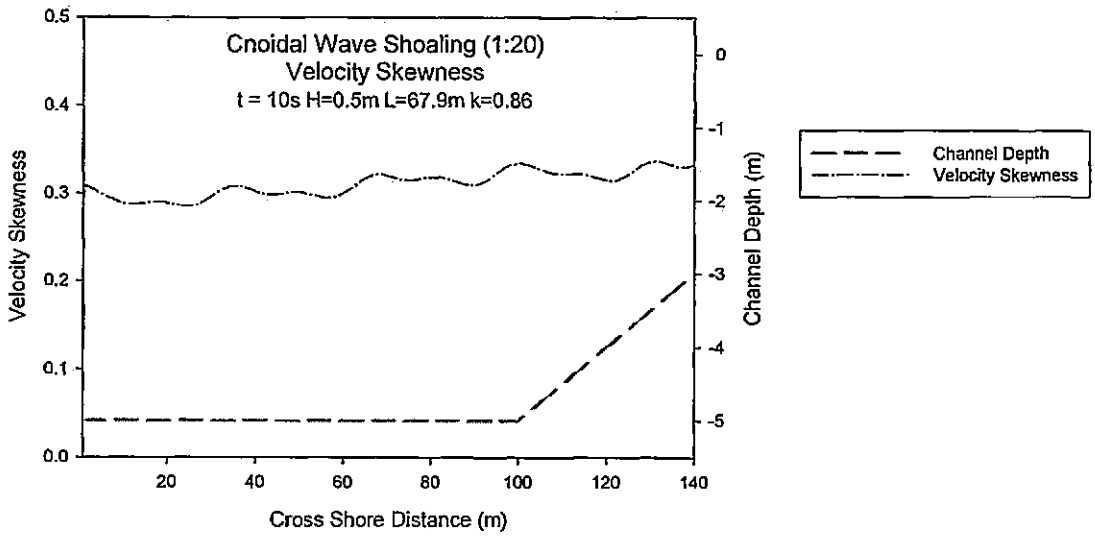

Figure 31 Velocity skewness of Cnoidal shoaling – 1:20 slope

Similar trends are seen as with the 1:40 case. The reflection coefficient from the numerical results is 3%, and the Battjes prediction is also 3%, while there is less growth in the higher harmonics.

Results for the 1:10 bed lope case are shown in Figures 32 to 34. For this case, the model reflection coefficient is found to be 8%, compared to the Battjes value of 12%. This is clearly visible in the profile figure and the FFT figure. The FFT also indicates

reflection occurring in the 2nd harmonic. The effect of reflection is also clearly seen in the velocity skewness results.

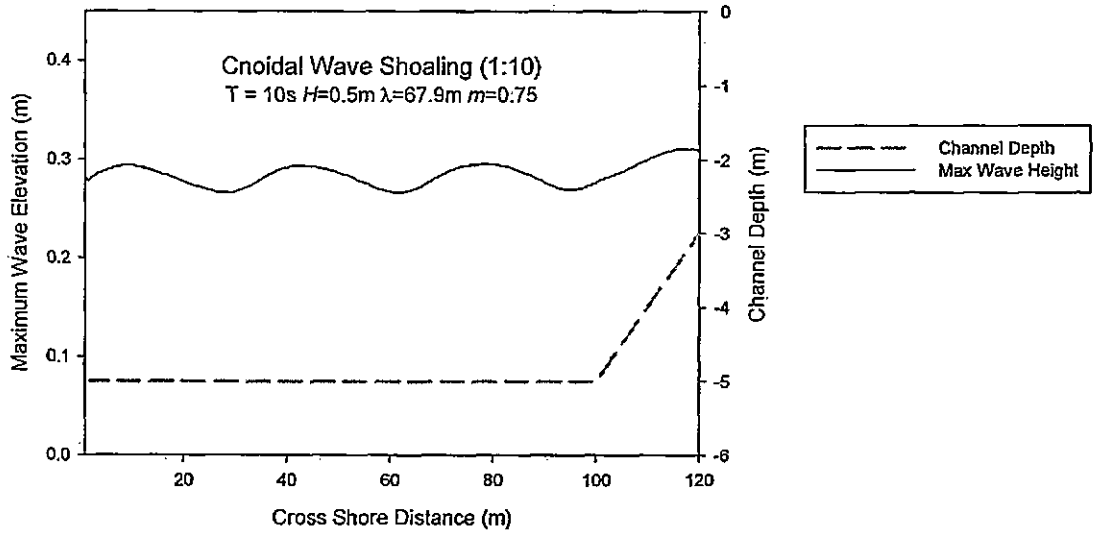

Figure 32 Cnoidal wave shoaling – 1:10 slope

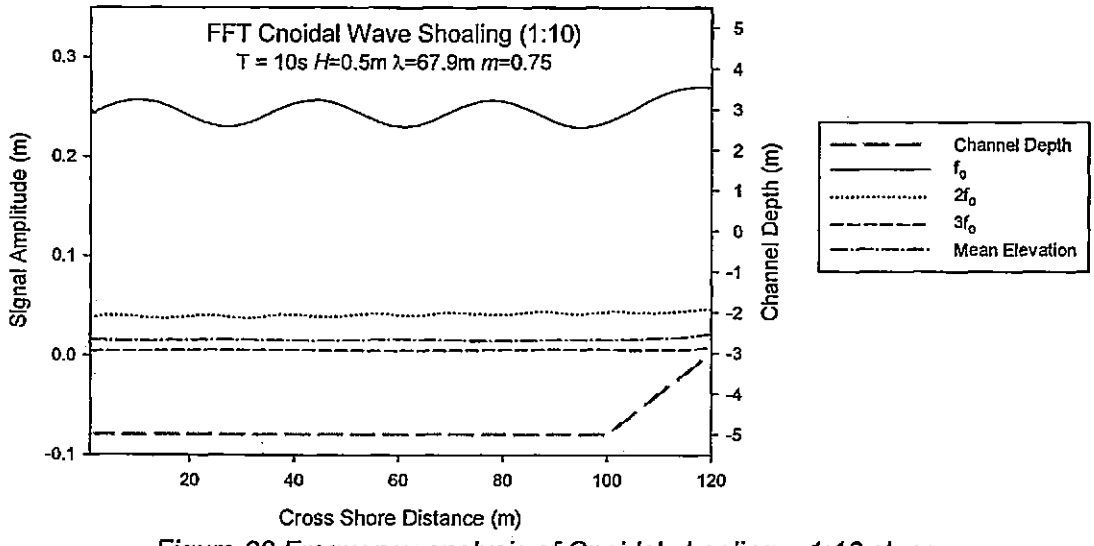

Figure 33 Frequency analysis of Cnoidal shoaling – 1:10 slope

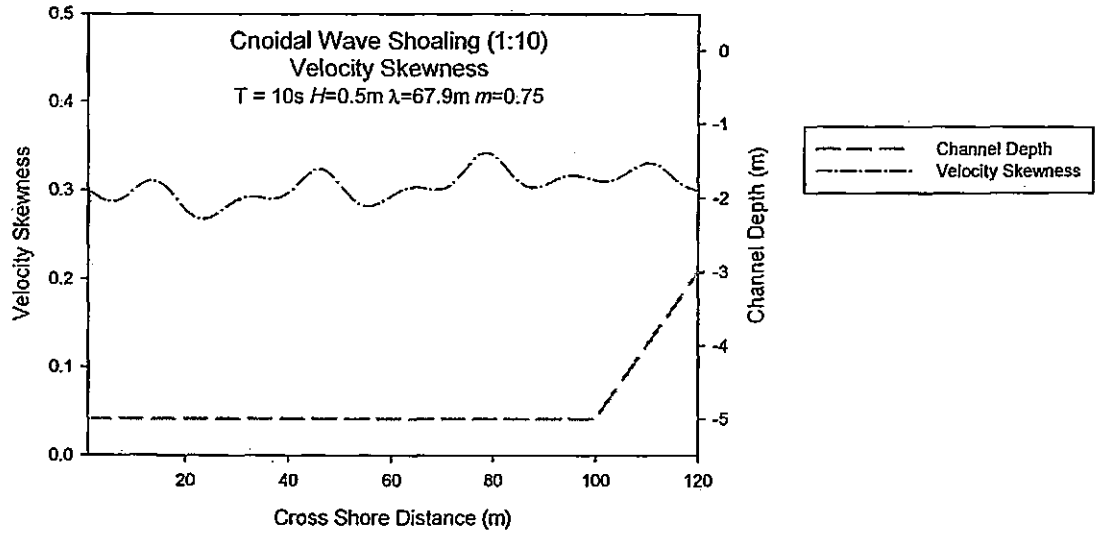

Figure 34 Velocity skewness of Cnoidal shoaling – 1:10 slope

The model was then extended by changing the shoaling bed into a symmetrical wedge with otherwise identical properties (case II). The wave propagated onward into a long flat bed region again, before finally dissipating into a sponge layer. The incident hydrodynamic conditions are the same as in the previous case, and of particular interest now are the downstream conditions beyond the wedge.

The results for the 1:40 case are shown in figures 35 to 37

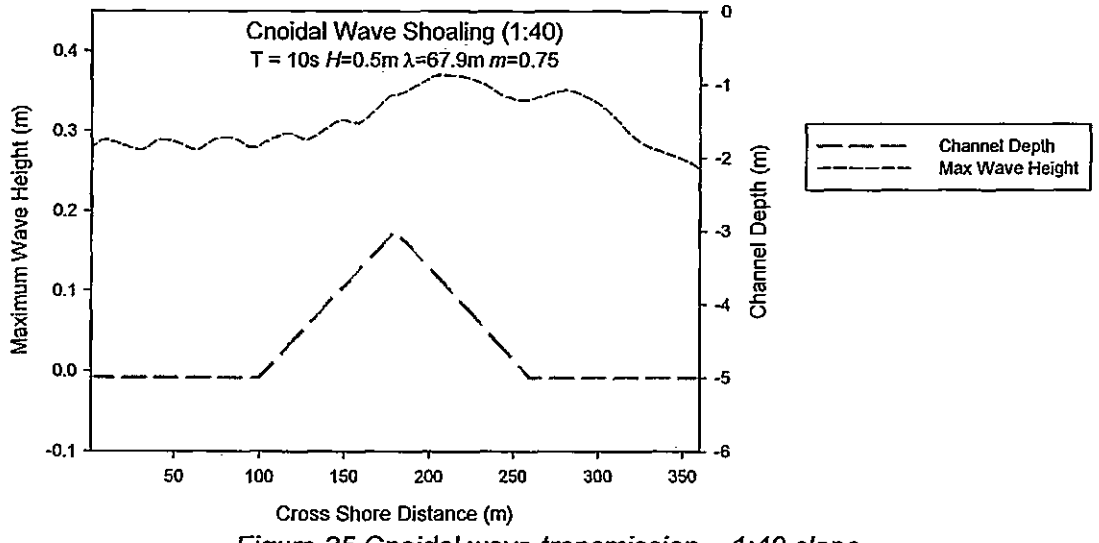

Figure 35 Cnoidal wave transmission – 1:40 slope

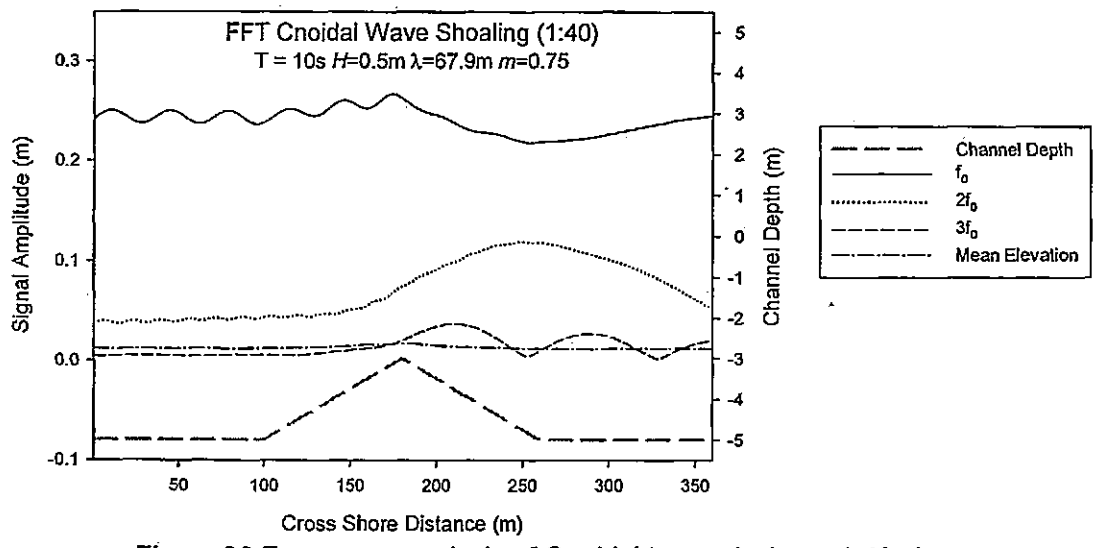

Figure 36 Frequency analysis of Cnoidal transmission – 1:40 slope

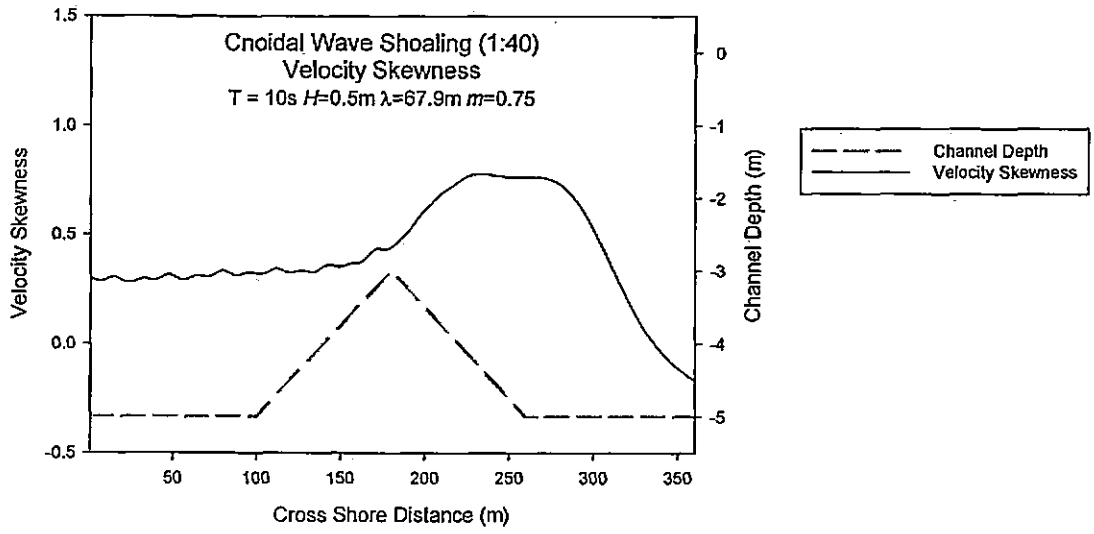

Figure 37 Velocity skewness of Cnoidal transmission – 1:40 slope

The wave reflection is again apparent between the wave-maker and the wedge. Beyond the wedge the wave shows considerable spatial variation, the FFT showing that energy transfer between the harmonics is taking place over significant spatial scales. Of particular note is the fact the incident wave is not recovered beyond the wedge. This is partly due to the energy transfer process, and partly due to the partial reflection of the incident wave. The effects of these changes are readily apparent in the velocity skewness figure. There are in fact minor differences between the previous case and this wedge case

near the crest itself. The numerical model calculates a 3rd order spatial derivative of the bed profile; since this changes across the crest position this causes a change in the numerical simulation. A further difference is that a wave propagating from shallow water to deep water is also partially reflected by the bathymetry change. Such a reflection will not be present in the previous shoaling case.

The results for the 1:20 wedge are shown in figures 38 to 40.

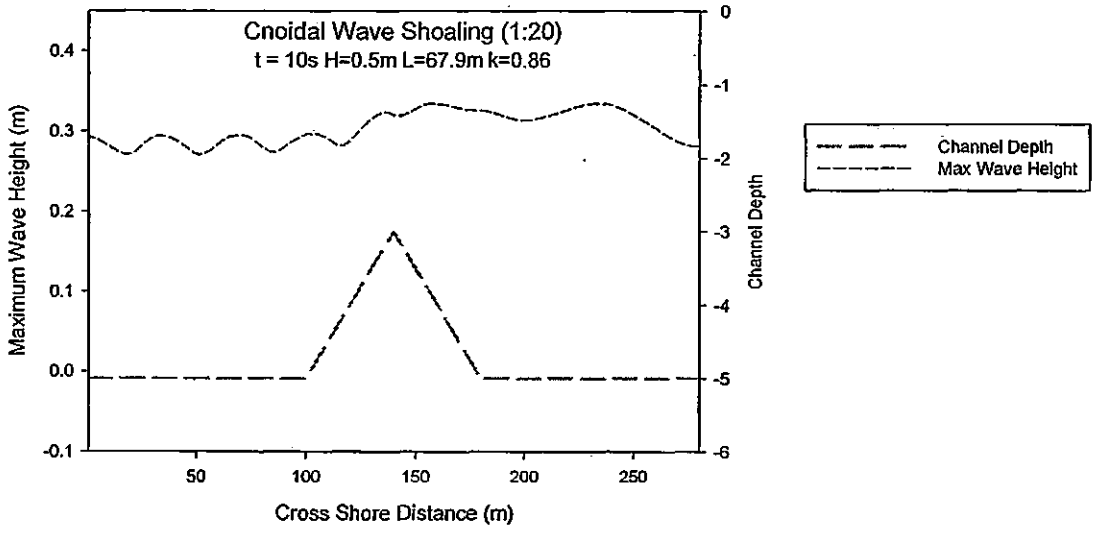

Figure 38 Cnoidal wave transmission – 1:20 slope

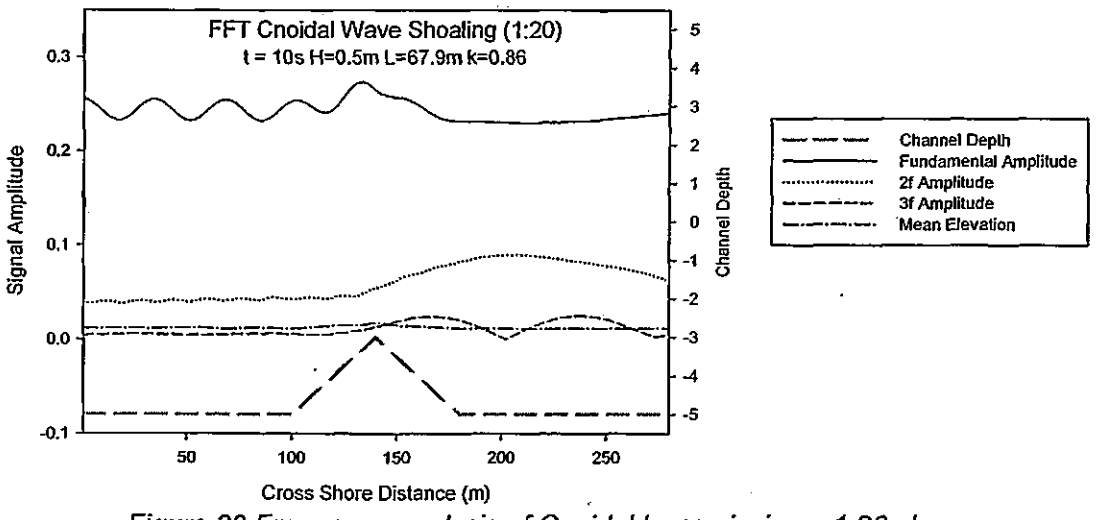

Figure 39 Frequency analysis of Cnoidal transmission – 1:20 slope

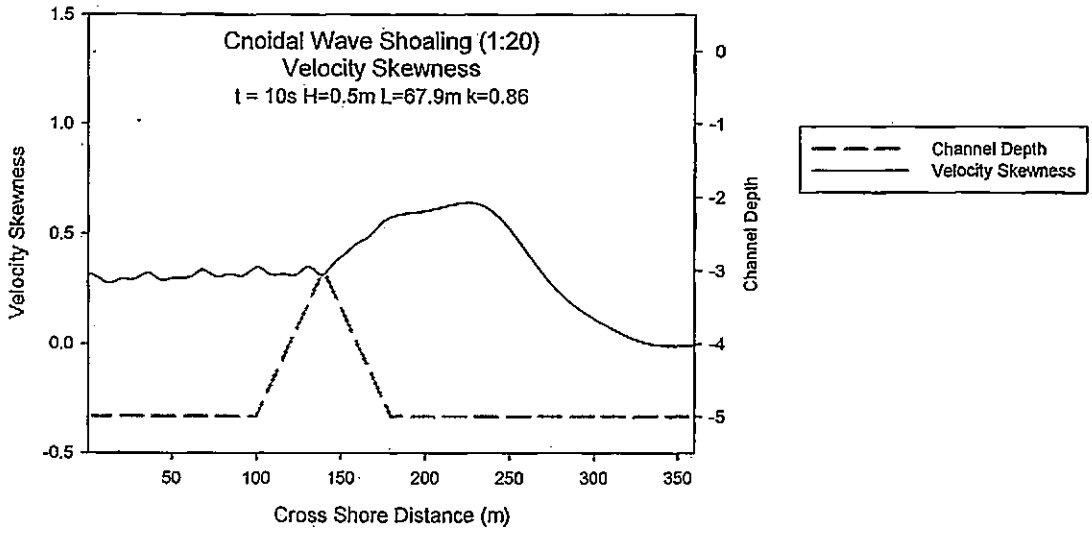

Figure 40 Velocity skewness of Cnoidal transmission – 1:20 slope

These show similar trends to the 1:40 case, with slowly varying energy exchange between the harmonics beyond the wedge, and a corresponding change of velocity skewness.

The sequence of results for the 1:10 wedge are shown in figures 41 to 43.

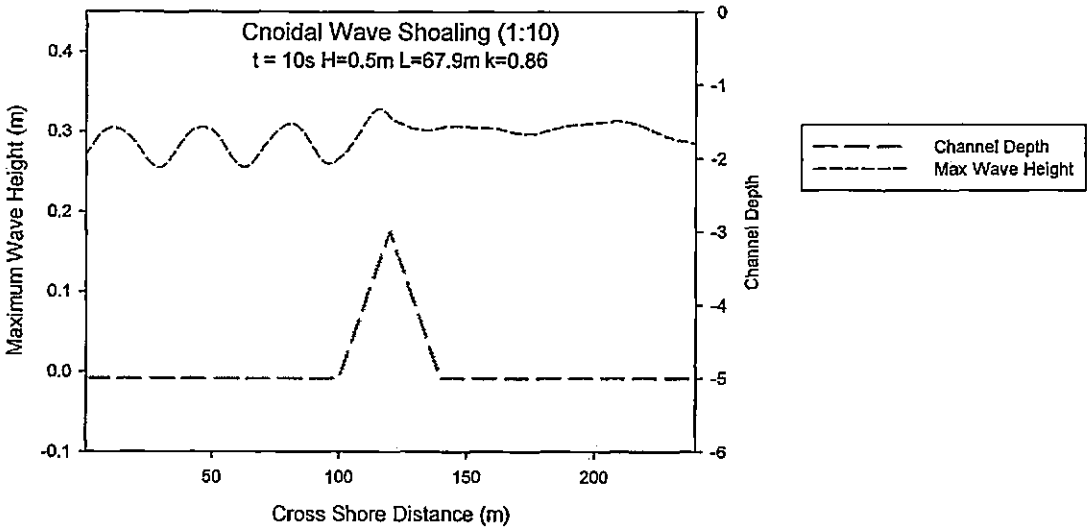

Figure 41 Cnoidal wave transmission – 1:10 slope

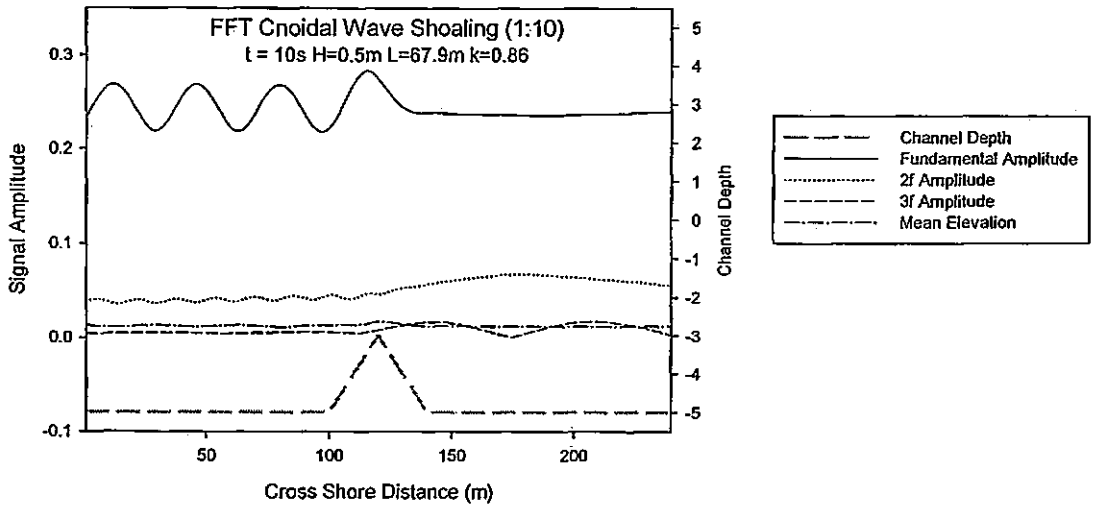

Figure 42 Frequency analysis of Cnoidal transmission – 1:10 slope

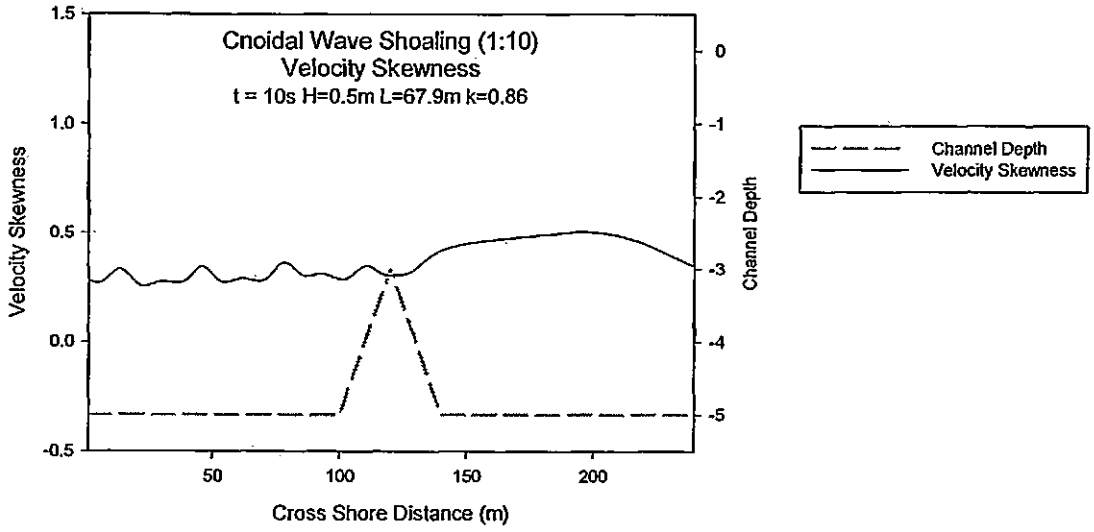

Figure 43 Velocity skewness of Cnoidal transmission – 1:10 slope

Again the same general pattern is observed. Similar patterns of transformed flow have been found in other experiments, both physical and numerical, but these have studied a different profile for the submerged bar. The present profile is studied to gain insight into the processes involved in wave reflection.

Returning to the flume characteristics of case I in this section, if instead of extending the model, the land boundary is replaced by a reflecting wall, the principle of superposition expects the resulting flow to the combination of the seaward side flow in case II with the (reversed) flow of the landward side. The model was then set up to study

this situation (case III). In Figure 44 the elevation profile for the numerical model of the reflecting tank shown for the 1:40 slope.

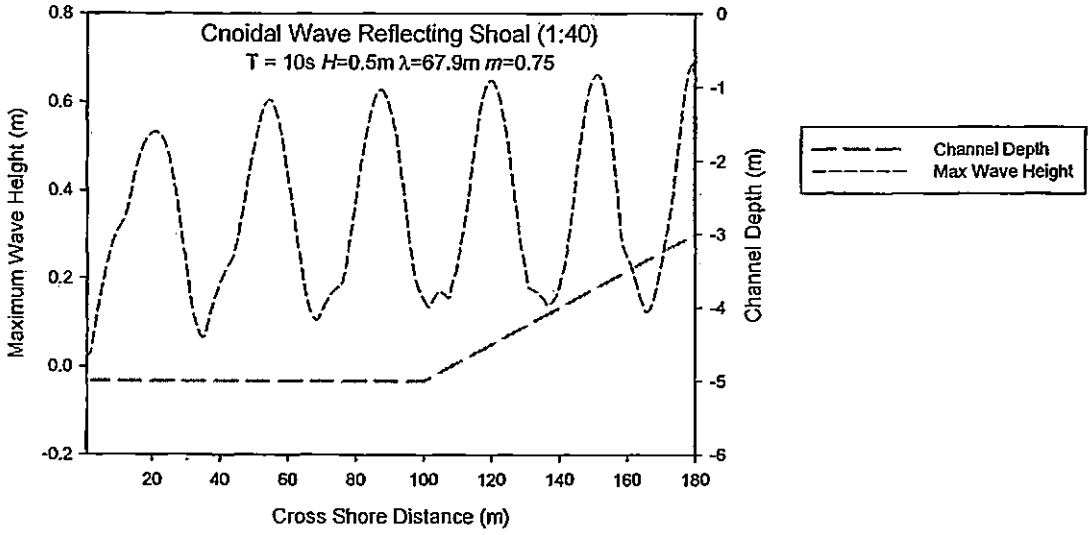

Figure 44 Cnoidal wave reflection – 1:40 slope

This shows a standing wave-like pattern of similar form to the flat bed case. However the nodal points show development of profile features. In Figure 45 this result is repeated, and compared with the result predicted by superposition described above. This is referred to as the linear re-combination.

A further comparison of non-linearity may be made by running the wedge model with two generated waves, one at the left and one at the right hand boundary. With a symmetrical profile and symmetrical wave generation, the leftward travelling wave after traversing the crest may be considered as the reflected wave of the right travelling counterpart in the reflecting model. This result is referred to as the non-linear recombination.

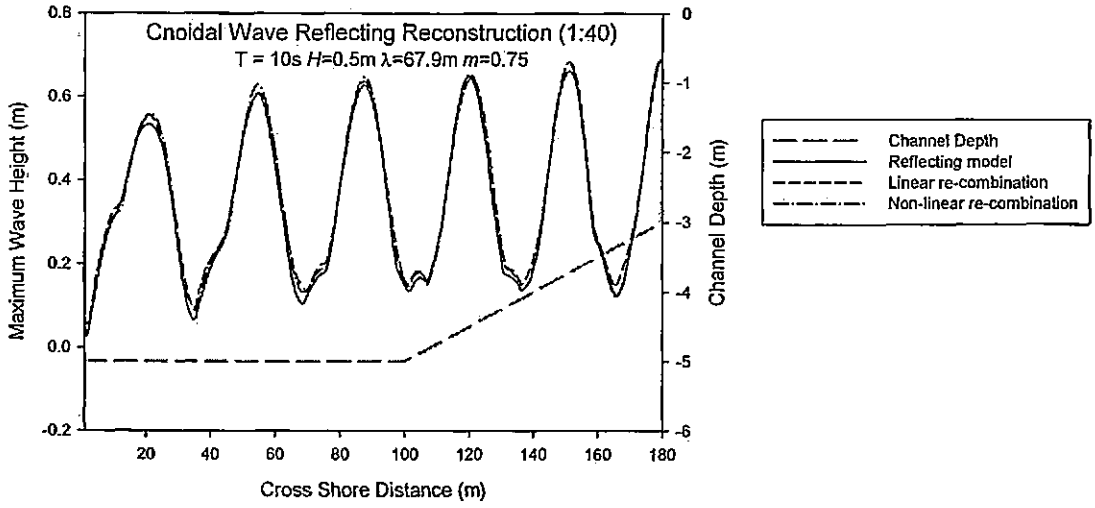

Figure 45 Cnoidal wave superposition – 1:40 slope

There is close agreement between the models, but the difference at the extrema is quite visible. This indicates the effect of the non-linear interactions between the waves.

The FFT for this case is shown in Figure 46.

This shows clearly the standing wave of the fundamental frequency similar to Figure 20. The pattern of the second harmonic is rather different however. Similar oscillations are seen, but have super-imposed on them the rise and fall of the transmitted second harmonic in the wedge model. The are also no true nodes in this pattern.

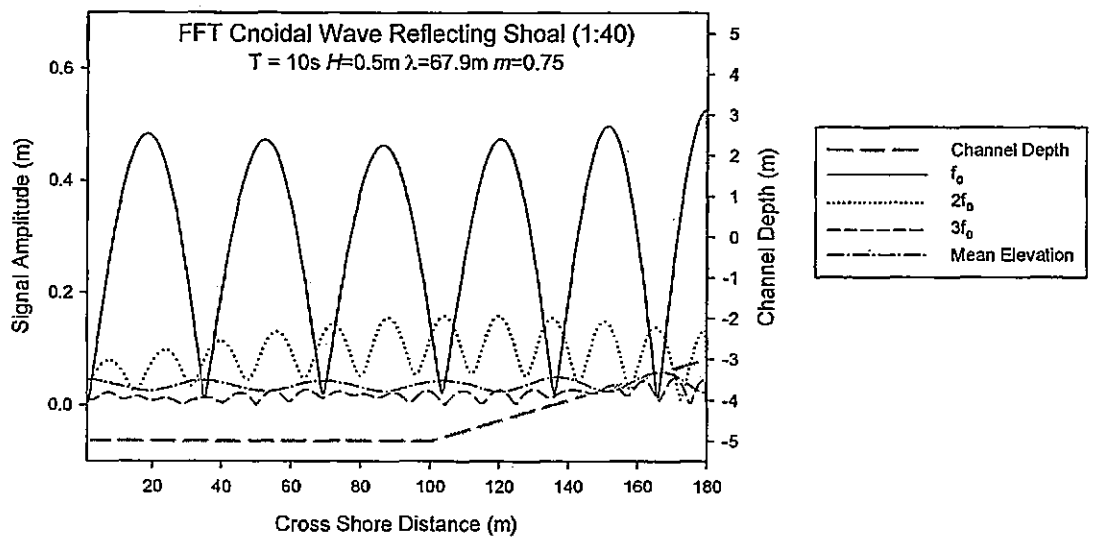

Figure 46 Frequency analysis of Cnoidal reflection – 1:40 slope

The velocity skewness pattern arising from this model is shown in Figure 47. The apparent spikes in the velocity are an artefact of the statistical computation, occurring at locations where the velocities from the model are always very small. The skewness calculation requires division by the time mean velocity, which is therefore approaching zero at these points. Since the actual velocities are low, in a sediment transport calculation there would be no sediment transport at these points. The general pattern shows a velocity skewness varying with the same space scale of the elevation standing wave.

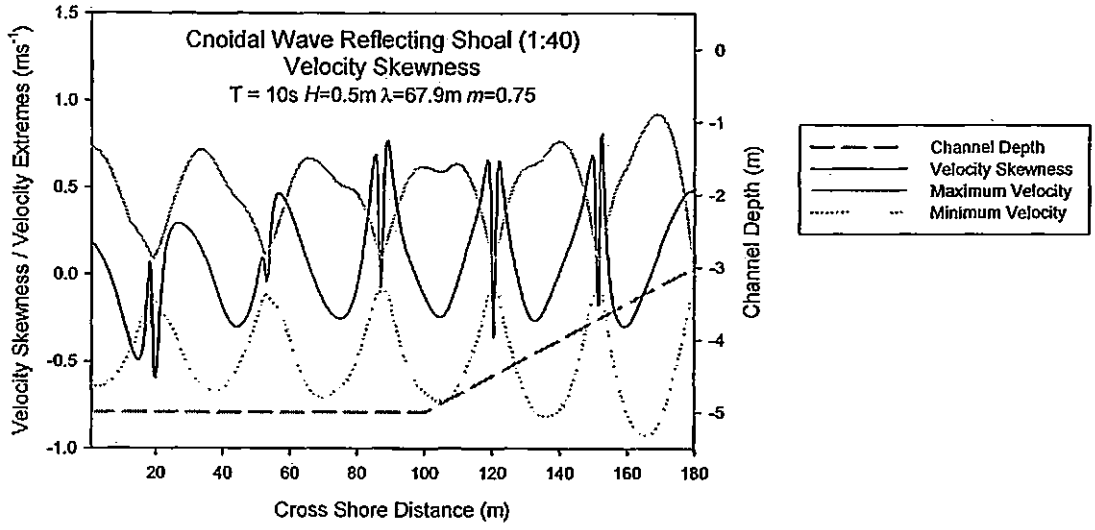

Figure 47 Velocity skewness of Cnoidal reflection – 1:40 slope

Figures 48 to 51 show the predictions of the reconstruction methods for the 1:20 slope case, with Figure 49 comparing them to the actual reflection profile obtained from the numerical model.

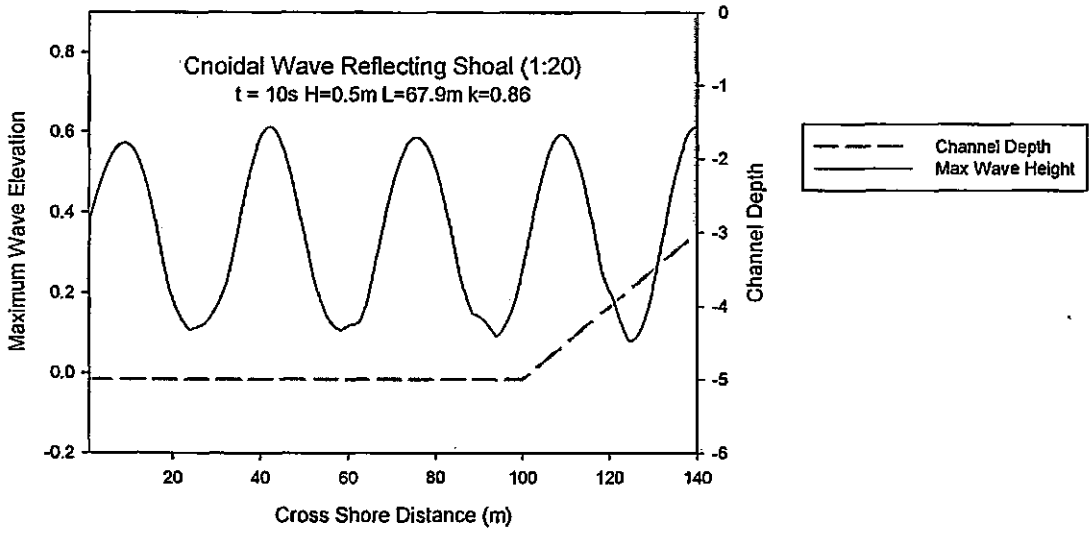

Figure 48 Cnoidal wave reflection – 1:20 slope

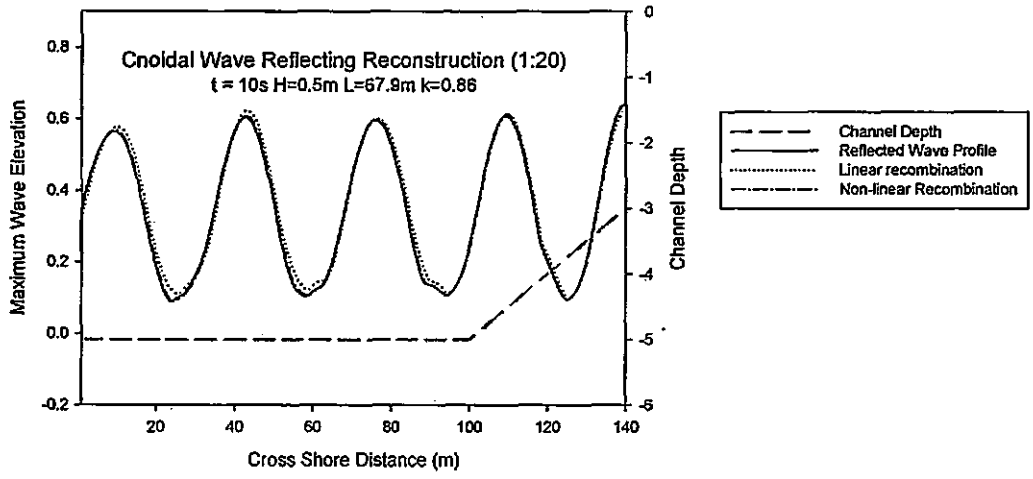

Figure 49 Cnoidal wave superposition – 1:20 slope

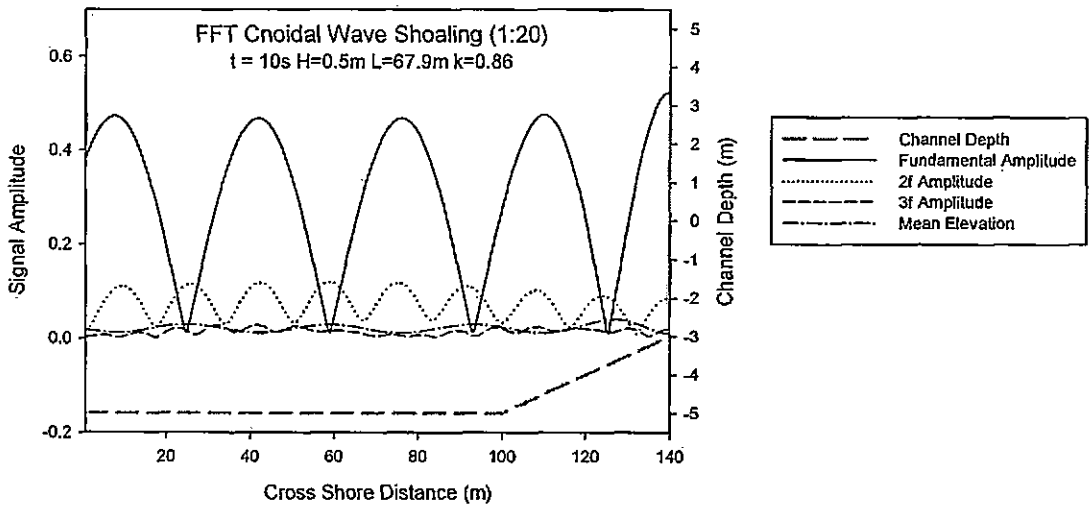

Figure 50 Frequency analysis of Cnoidal reflection – 1:20 slope

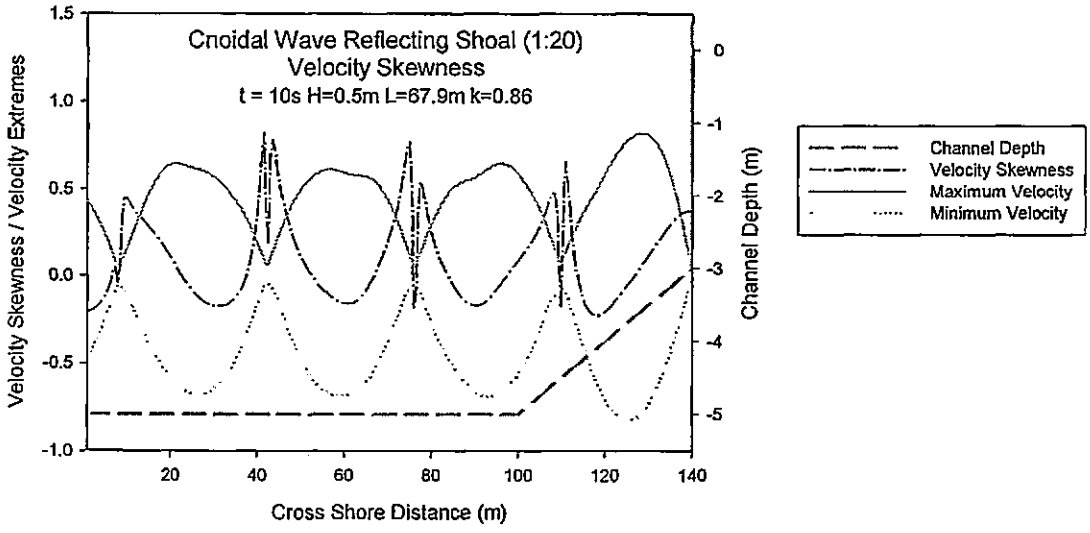

Figure 51 Velocity skewness of Cnoidal reflection – 1:20 slope

This also shows a similar set of trends. The differences between the linear and the non-linear interactions are seen in Figure 49. The frequency analysis again shows the modulation of the higher harmonics, and the length scale of the skewness variation is clearly seen.

Figures 52 to 54 show the predictions of the reconstruction methods for the 1:10 slope case, and compares them to the actual reflection profile obtained from the numerical model.

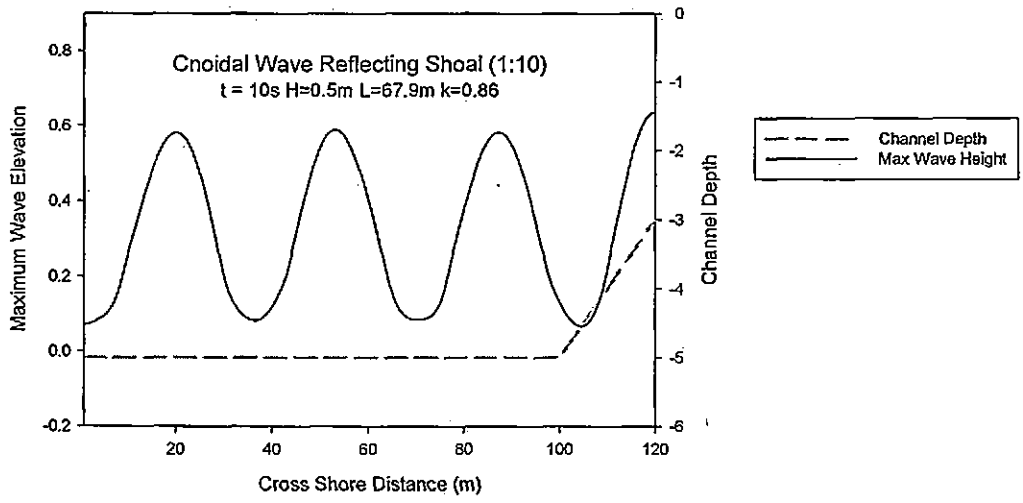

Figure 52 Cnoidal wave reflection – 1:10 slope

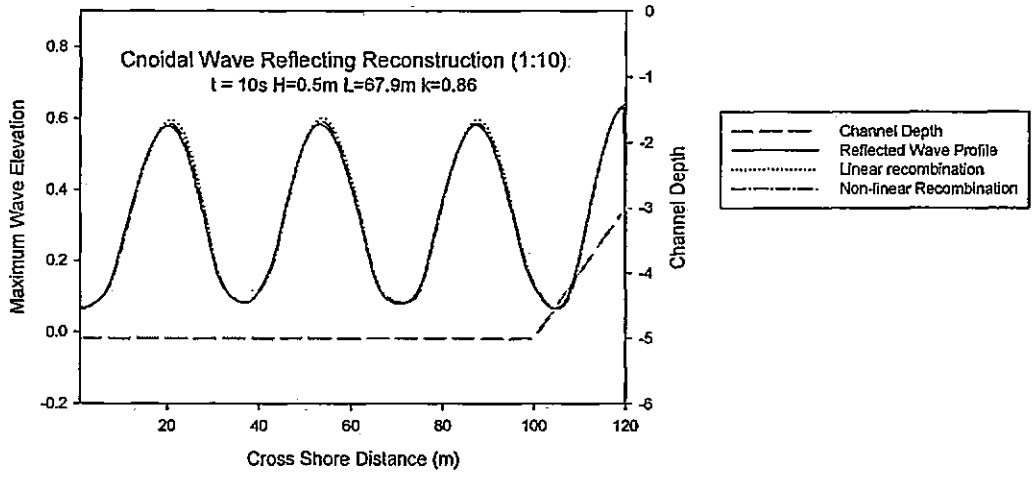

Figure 53 Cnoidal wave superposition – 1:10 slope

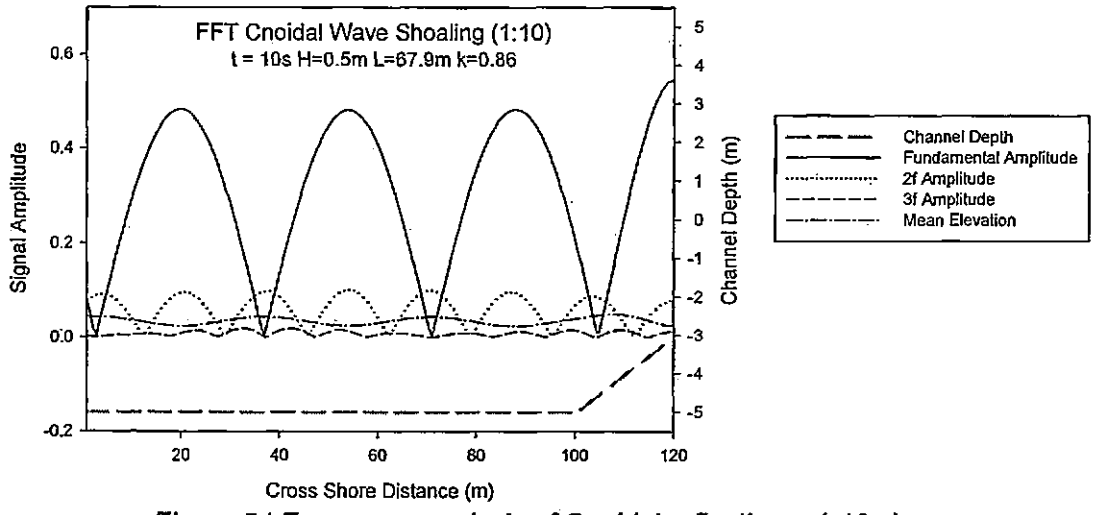

Figure 54 Frequency analysis of Cnoidal reflection – 1:10 slope

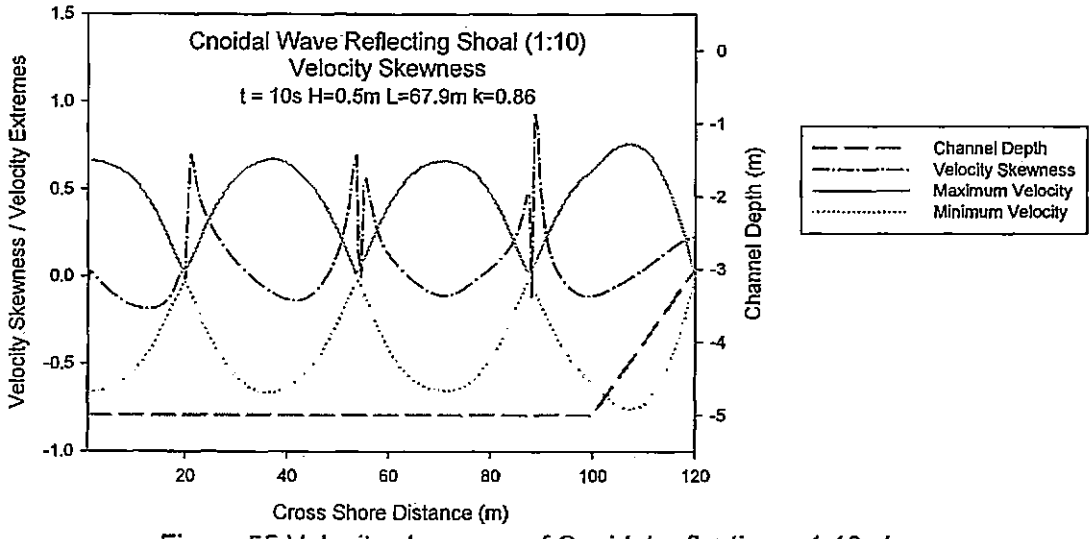

Figure 55 Velocity skewness of Cnoidal reflection – 1:10 slope

In all cases the contribution to the wave profiles due to slope reflection and non-linear interactions may be discerned. The changes in velocity skewness are also of considerable magnitude.

As the incident wave traverses the rising slope of the reflecting boundary, it undergoes the same reflection/process as in the rising wedge of case I. Therefore not all the incident energy can be reflected at the sea wall. Accordingly, the reflected wave interference is modulated. The final pattern of the velocity skewness field is seen to have

a contribution from the wave component reflected off the slope, and separately the reflection off the sea wall.

4. Sediment Transport Modelling

4.1. Bed shear stress calculations

Sediment transport at the sea bed is driven by the transfer of energy and momentum from the fluid to the sediment. A principle mechanism for this transfer is the interaction of fluid shear stress and the sediment (Soulsby , 1997). Therefore it is first necessary to estimate the magnitude of this shear stress before estimating the transport rate. Two approaches have been evaluated. The first is to use Manning's friction law to determine the bed shear stress. This assumes the flow is generally comparable to a uniform flow, such as over a river bed. The second approach is to consider the wave motion at the sea bed, and uses a flow dependent wave friction factor. A variety of empirical laws have been suggested for this approach.

The first approach, Manning's law, states that the bed shear stress is given by

$$\tau_b = \frac{\rho g \hat{u}^2 n^2}{h^{1/3}} \tag{39}$$

where n is a changing parameter for different types of flow (e.g. open, river, pipe, channel), and is also a measure of the bed roughness. The principle physical rule of this law is that shear stress will increase as the water depth under a wave gets smaller.

The second approach, a friction factor, has been considered by examining three available formulations for a wave friction factor. These calculate the bed shear stress from

$$\tau_b = \frac{1}{2}\rho f_{wr} u_w^2 \tag{40}$$

where f_{wr} is the friction factor and u_w is the bed velocity. In the model ,linear wave theory is used to derive u_w from $\hat{u}$.

Swart, (1974) suggests

$$\left.\begin{aligned} f_{wr} &= 0.3 \\ f_{wr} &= 0.00251 e^{(5.21 r^{-0.19})} \end{aligned}\right\} \text{for} \begin{cases} r \le 1.57 \\ r > 1.57 \end{cases} \tag{41}$$

Nielsen (1992) suggests

$f_{wr} = e^{(5.5r^{-2}-6.3)}$ for all r, (42)

and Soulsby (1997) suggests

$f_{wr} = 0.237r^{(-0.52)}$ for all r (43)

where

$r = A_e / k_s$

A_e = wave semi orbital excursion

N=0.04$k_s^{1/6}$ = Manning's n

k_s= 3d_{90} = Nikuradse equivalent sand grain roughness

d_{90} = 90% grainsize

These formulations , and others, are available in Soulsby (1997). Packwood, (1980), and Chadwick (1991) have found that when considering flows in the surf zone, Manning's n should be multiplied by a coefficient of the value 2~3.

A comparison of the bed shear stresses given by these four methods is shown in figures 56 and 57. Shear stress is shown as a function of grain size for combinations of fluid velocity and depth. Shear stress according to Manning's law is shown for coefficients of 1 (i.e. unaltered) and 2. To determine the wave friction factors, a wave orbital excursion is required. To establish equivalence between the Manning's formulation and the friction factor formulation, linear shallow water theory is used. The wave amplitude for the given wavelength in the given total water depth is determined for which the maximum depth mean velocity is equal to the depth mean velocity of the Manning's calculation.

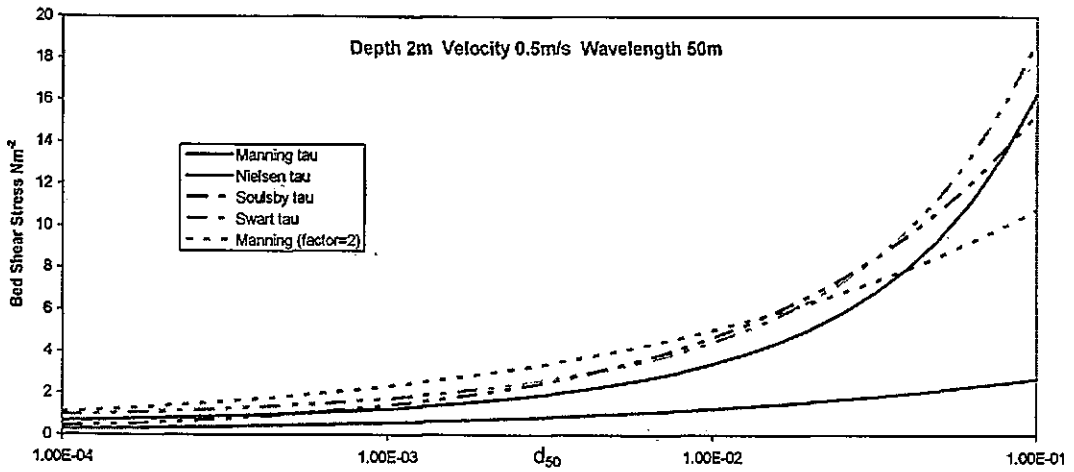

Figure 56 Comparison of friction factor results (a)

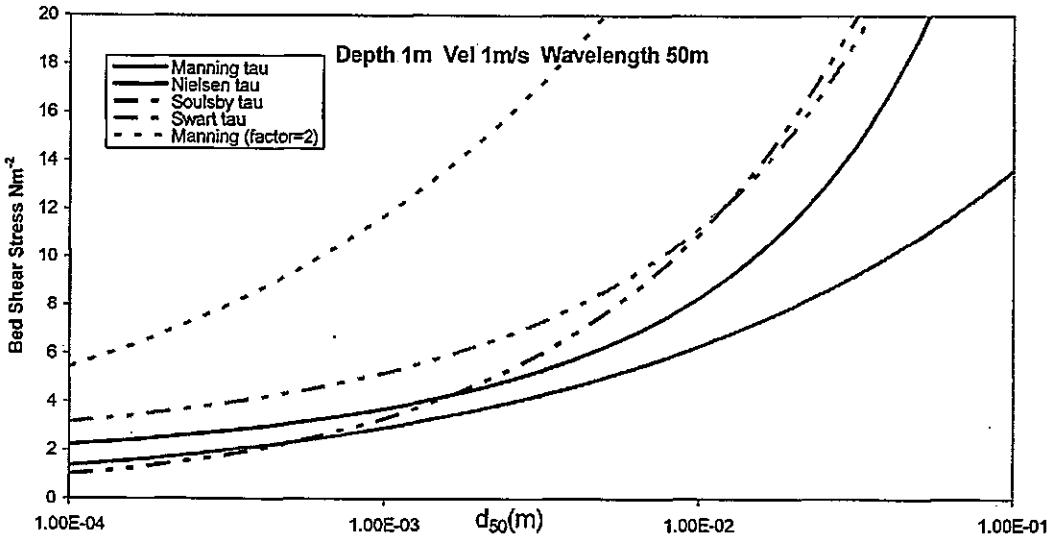

Figure 57 Comparison of friction factor results (b)

It can be seen that agreement between the Manning's formulation and the friction factor formulations is dependent on the depth of the flow and can obviously be 'tuned' by Packwood's factor. Manning's law directly includes a height dependency that calculates a higher shear stress in shallower water. Shoaling waves generally increase in wave amplitude near the shore, and therefore have higher bed excursions and higher bed velocities. The wave friction factor reduces as the bed excursion increases, but as the full

friction formula is (friction factor)*(velocity squared), the final bed friction prediction also grows as the wave moves into shallower water.

4.2. Sediment transport calculations

For shingle beaches, bed load sediment flow is found to predominate. The estimated sediment transport rate is determined as a function of the bed shear stress (estimated from the depth mean velocity) and the grain size. Initially, this is considered for a single grain size. The modification used in the presence of multiple grain sizes is discussed in section 4.4. A variety of formulations are presented in Soulsby (1997). Some comparisons of their predictions were presented in Lawrence *et al.*, (2001). Particular choices are detailed below.

Shields (1936) investigated the threshold of motion of sediments. The Shields parameter

$$\theta = \frac{\tau_b}{g(\rho_s - \rho)d_{50}}$$

is used to determine the onset of motion. This measures the ratio of frictional and gravitational forces acting on a grain. The critical value required for sediment motion has been established empirically, and the best expression for this is given by Soulsby and Whitehouse, (1997) as

$$\theta_{cr} = \frac{0.3}{1+1.2d_*} + 0.055(1-e^{-.020d_*}) \qquad (44)$$

where d* is the dimensionless grain size given by

$$d_* = \left[\frac{(\rho_s/\rho - 1)g}{\nu^2}\right]^{1/3} \qquad (45)$$

Sediment flow occurs for $\theta > \theta_{cr}$.

The critical shear stress is modified for the bed slope by correction factor of

$$\alpha_\psi = \left[\frac{\sin(\beta \pm \psi)}{\sin(\beta)}\right] \qquad 46$$

where β is the angle of repose of the material, and ψ is the local angle of slope for the beach. The sign of y is dependent on the direction of the slope and the instantaneous velocity, so that upslope transport is retarded and downslope transport is enhanced.

Two approaches for the sediment transport have also been evaluated.

McDowell (1989) uses a virtual stream power method as follows

$$
\begin{aligned}
u_* &= (\tau_b / \rho)^{1/2} \\
P &= \rho u_*^3 \\
u_0 &= (\tau_{cr} / \rho)^{1/2} \\
P_0 &= \rho u_0^3 \\
s_m &= 17.4(\rho g)^2 N^4 \tau_b^{-6} d_{50}^{-1/2} (P - P_0)^{5.03} \\
q_s &= \frac{s_m}{\rho_s - \rho_w}(1+e)
\end{aligned}
\tag{47}
$$

Nielsen and Van Rijn have developed an alternative approach, based in part on a force balance. Defining Φ as the dimensionless transport rate, and

$$q_s = q_s(\tau_b, \tau_{cr}) = \Phi[g(s-1)d^3]^{1/2} \tag{48}$$

where van Rijn, (1984) uses

$$
\begin{aligned}
\Phi &= F_R \theta^{1/2} (\theta^{1/2} - \theta_{cr}^{1/2})^{2.4} \\
F_R &= \frac{0.005}{C_D^{1.7}} \left(\frac{d_{50}}{h} \right)^{0.2}
\end{aligned}
\tag{49}
$$

and Nielsen (1992) uses the simpler

$$\Phi = 12\theta^{1/2}(\theta - \theta_{cr}) \tag{50}$$

Figures 58 to 60 compare the results of these formulations.

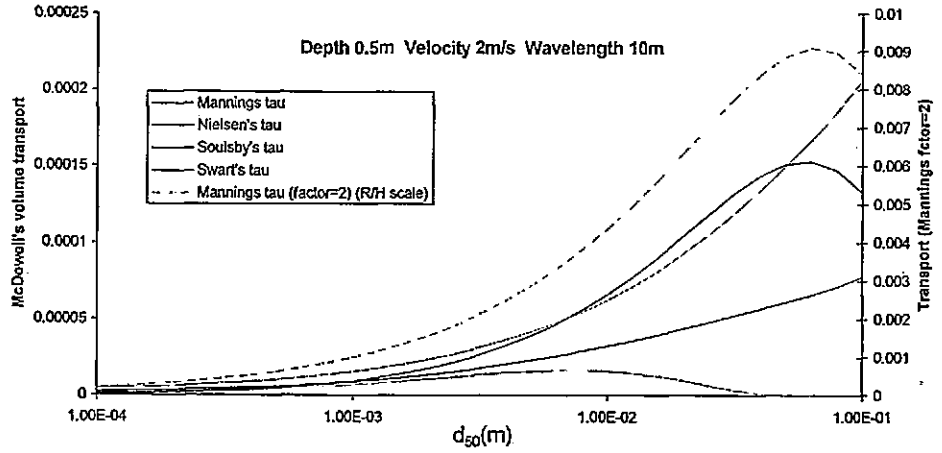

Figure 58 Sediment transport estimated by McDowell's formula

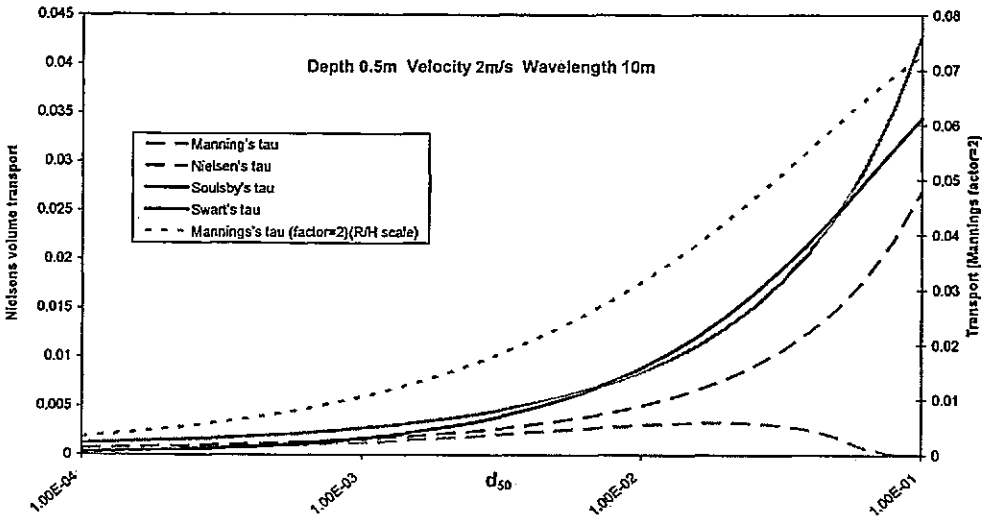

Figure 59 Sediment transport estimated by Nielsen's formula

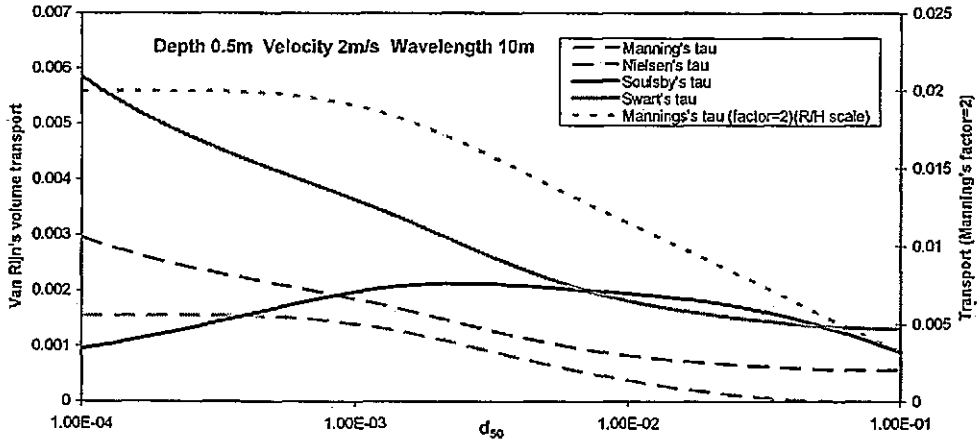

Figure 60 Sediment transport estimated by van Rijn's formula

There is clearly considerable variation between these formulations, in particular in the response of the transport prediction with regard to grain size.

No account is taken by either the shear stress model or the transport model of enhanced stress and therefore transport due to increased turbulence from the breaking wave.

4.3. Undertow

In the hydrodynamic model mode without a shoreline boundary there is a 'run off' region of shallow water after the slope, ending in a numerical sponge layer. As a consequence there is a net flow of water through the model, partly due to a Stokes drift-like mechanism, and partly due to onshore transport in the wave surface roller. In the physical situation, the net onshore hydrodynamic flux is zero, as onshore fluxes are matched by the wave undertow. Accordingly, the net flow through the model may be used as an estimate for the undertow. Comparisons are now made between ignoring and correcting for the undertow in the bed stress calculations. The undertow is estimated by determining the time averaged mass flux in the model at the edge of the sponge layer, and subtracting this from the instantaneous mass fluxes. These corrected mass fluxes are then used to calculate corrected depth mean velocities.

The model has been run for a test case of a 1:20 bed slope from 5m depth to 0.3m depth, with input waves of 0.75m wave height, and wavelengths of 75m (Cnoidal wave),

35m (Cnoidal wave) and 22m(sinusoidal wave), with corresponding wave steepnesses of 0.01, 0.02, 0.04. These values have been restricted to those the hydrodynamic model has been able to run without showing signs of instability. This appears to be a restriction caused by the performance of the model in the shallow water 'run off' region, which must remain deep enough to allow the incoming wave to propagate without the wave trough touching the sea bed.

To evaluate the bed shear stress according to Manning's law, the instantaneous values of the depth averaged current are evaluated at each node. To evaluate the wave friction factors, the model time series output has to be analysed to calculate the wave amplitude at each node. From the wave amplitude the wave orbital excursions may be calculated by using linear wave theory.

The figures 61 to 63 show the maximum wave height in the model for the three cases, and the associated roller thickness.

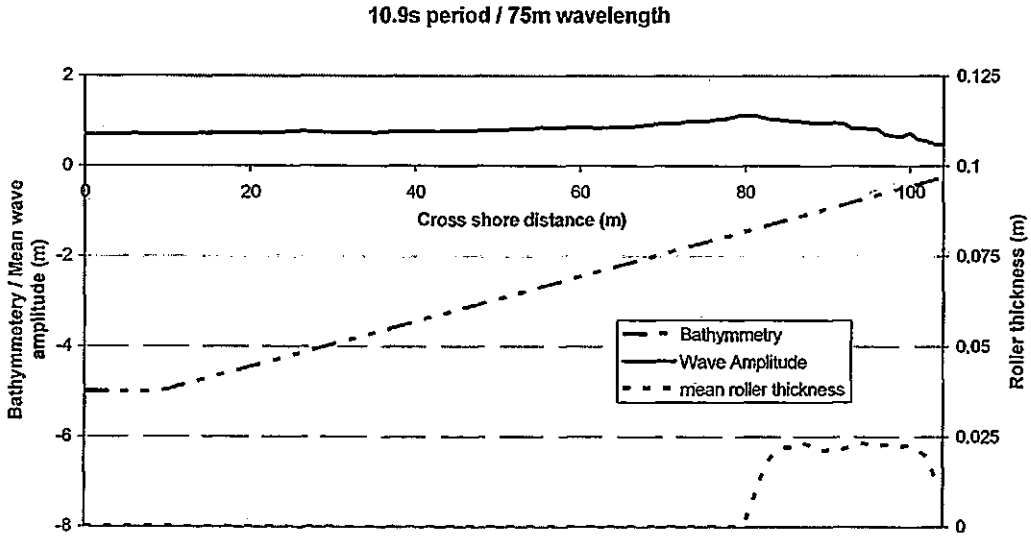

Figure 61 Cross shore wave amplitude – 75m wave length

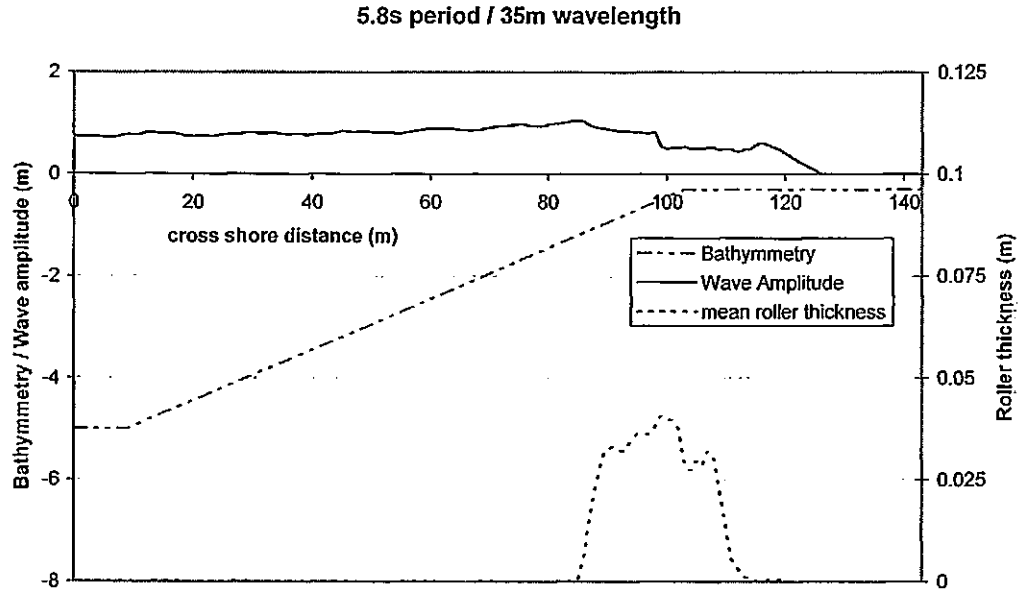

Figure 62 Cross shore wave amplitude - 35m wave length

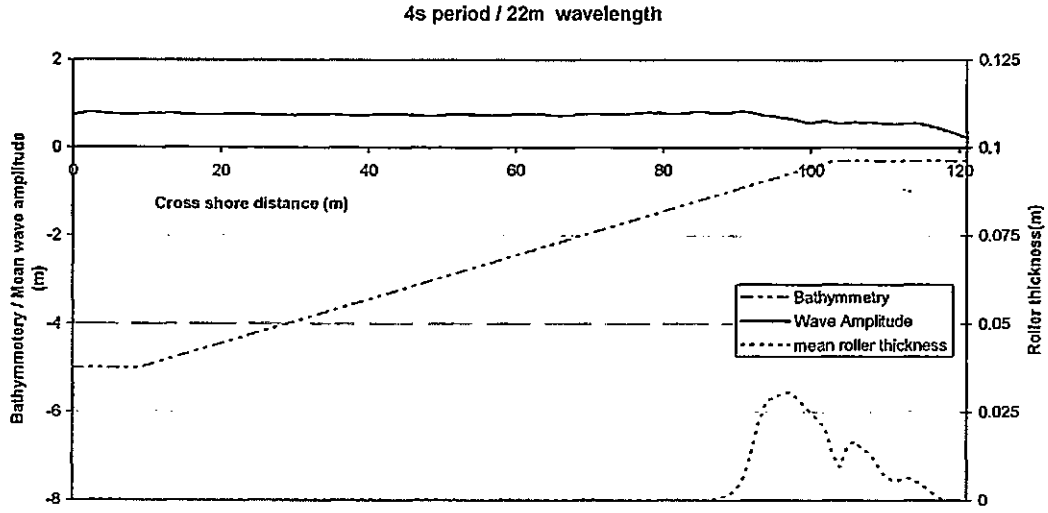

Figure 63 Cross shore wave amplitude – 22m wave length

Figures 64 to 66 show the maximum and mean onshore and offshore velocities output by the model. These are shown as the values calculated directly from the model, and also the values with the undertow correction described above. By correcting for the undertow it can be seen the calculated onshore velocities are reduced, and the corresponding offshore velocities are increased. Onshore values are positive.

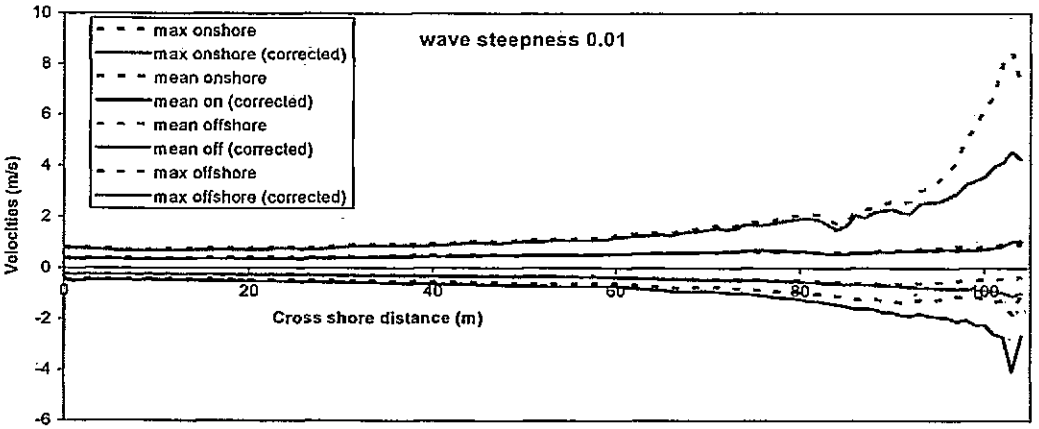

Figure 64 Cross shore wave velocities – 75m wave length

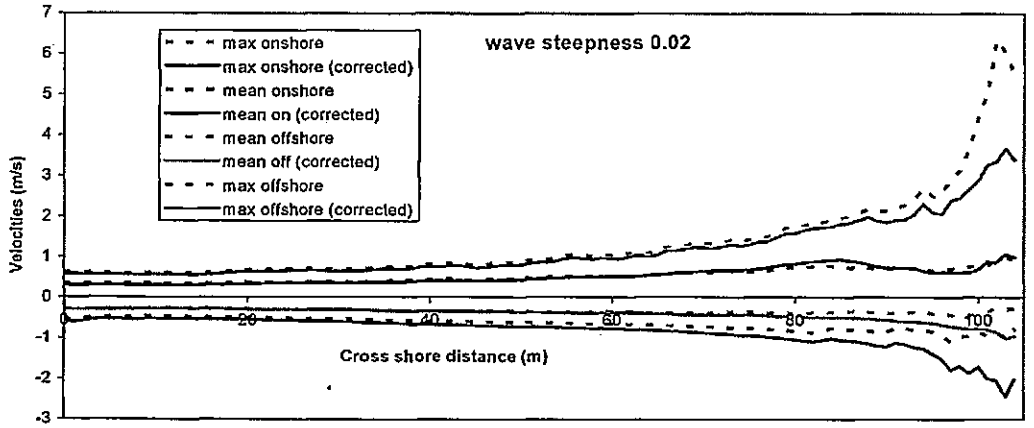

Figure 65 Cross shore wave velocities – 35m wave length

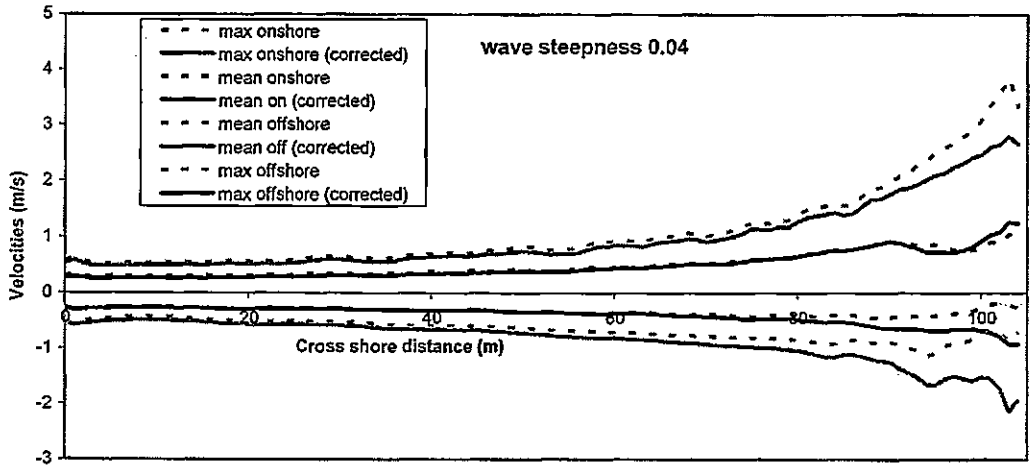

Figure 66 Cross shore wave velocities – 22m wave length

The figures 67 - 72 show the maximum onshore and offshore bed shear stresses for the long wave case with two values of d_{50}, (= .02 and .001m), neglecting and including the undertow corrections. The figures now show the cross shore variation from a point 50m from the left hand boundary, to show detail at the top of the slope better. Comparisons of the instantaneous values of bed shear stress at a particular timestep are also shown.

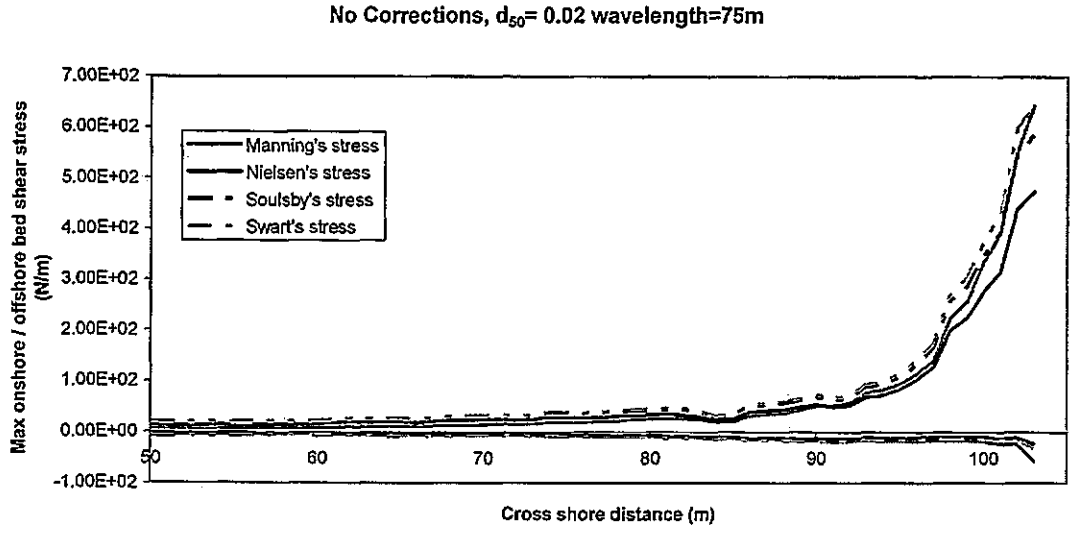

Figure 67 Cross shore uncorrected bed shear stress – d_{50}=0.02m

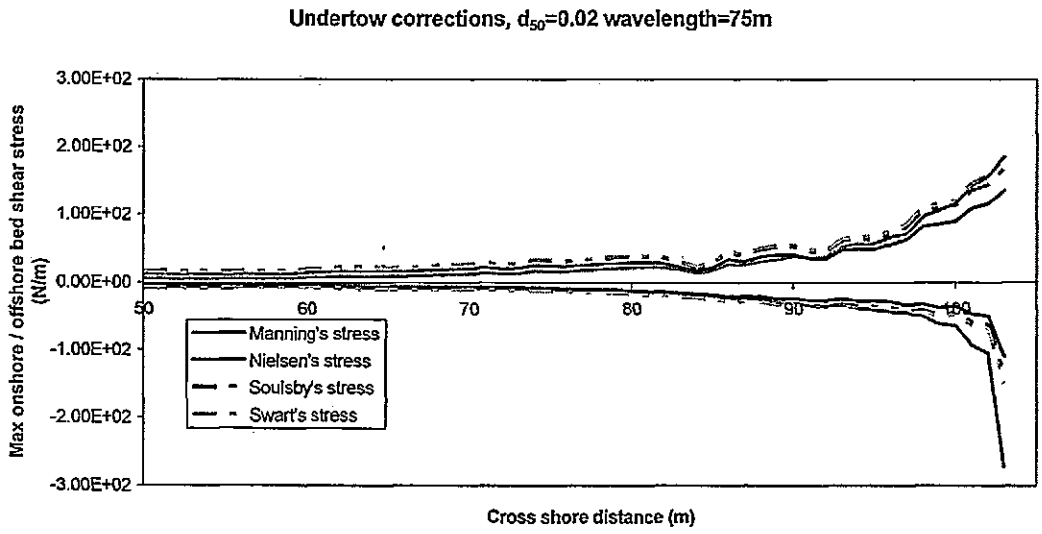

Figure 68 Cross shore corrected bed shear stress – d_{50}=0.02m

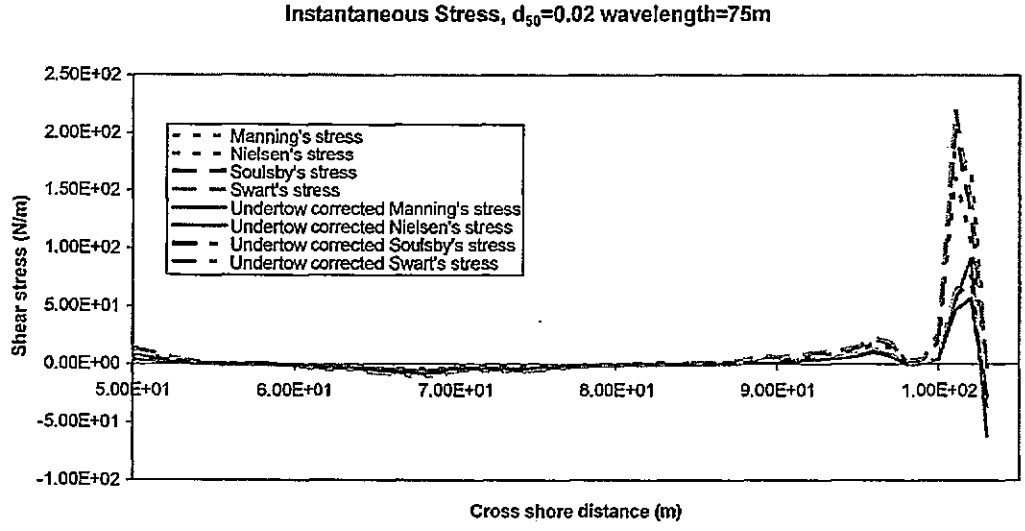

Figure 69 Cross shore instantaneous bed shear stress – d_{50}=0.02m

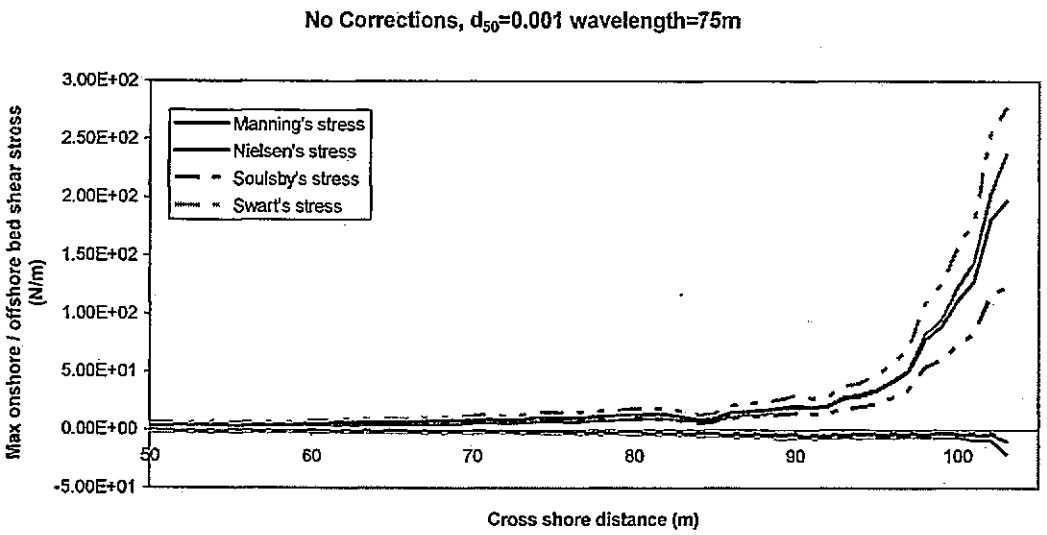

Figure 70 Cross shore uncorrected bed shear stress – d_{50}=0.001m

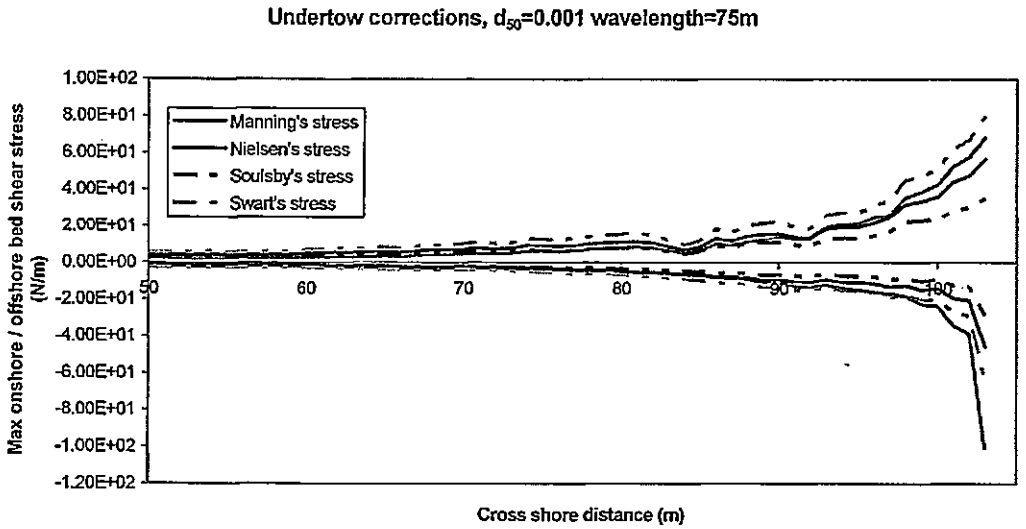

Figure 71 Cross shore corrected bed shear stress – d_{50}=0.001m

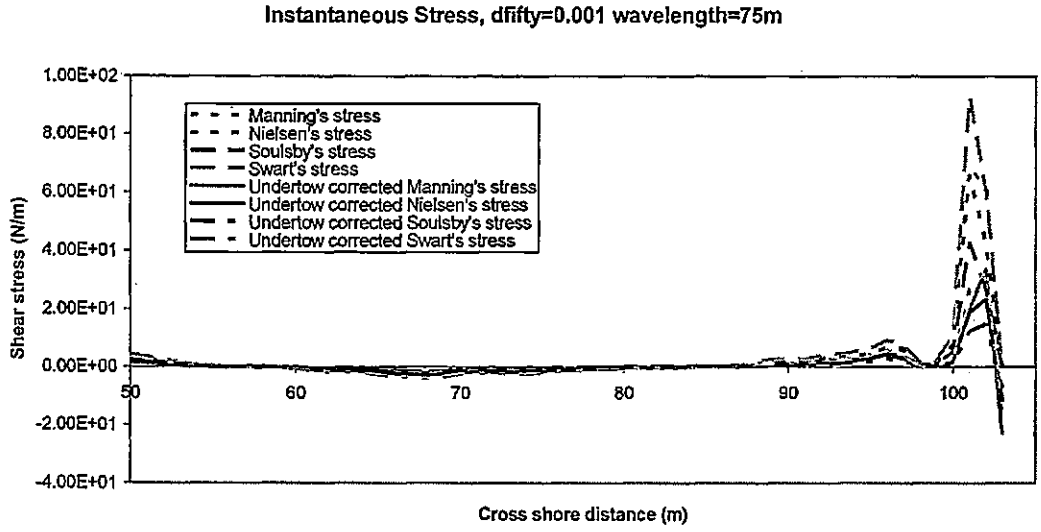

Figure 72 Cross shore instantaneous bed shear stress – d_{50}=0.001m

It can be seen from the figures that before correcting for undertow the calculated onshore shear stresses can be an order of magnitude greater than the calculated offshore. The undertow correction makes the onshore and offshore stresses comparable. It can also be seen that the various stress formulations lead to similar calculated values, despite the different physical assumptions made.

Figures 73 – 78 show the some of calculated transport rates for the long wave case with a d_{50} of 0.02m. The instantaneous transport rates correspond to the timestep for the instantaneous stresses. The net transport rates are the time integrated transport through each grid point in the model over a single wave period. Again, the figures are calculated neglecting and including the undertow correction, and are from a point 50m from the left hand boundary.

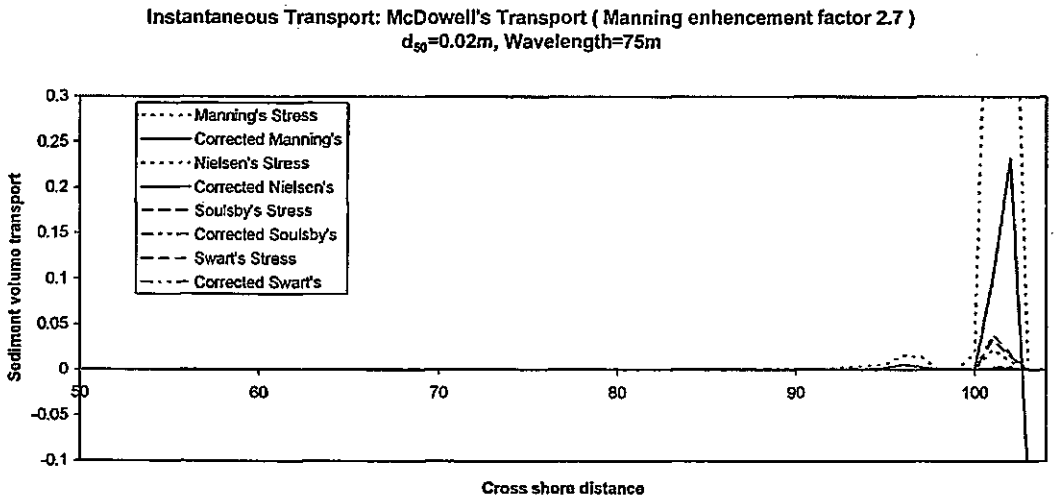

Figure 73 Instantaneous transport rates, McDowell's formula

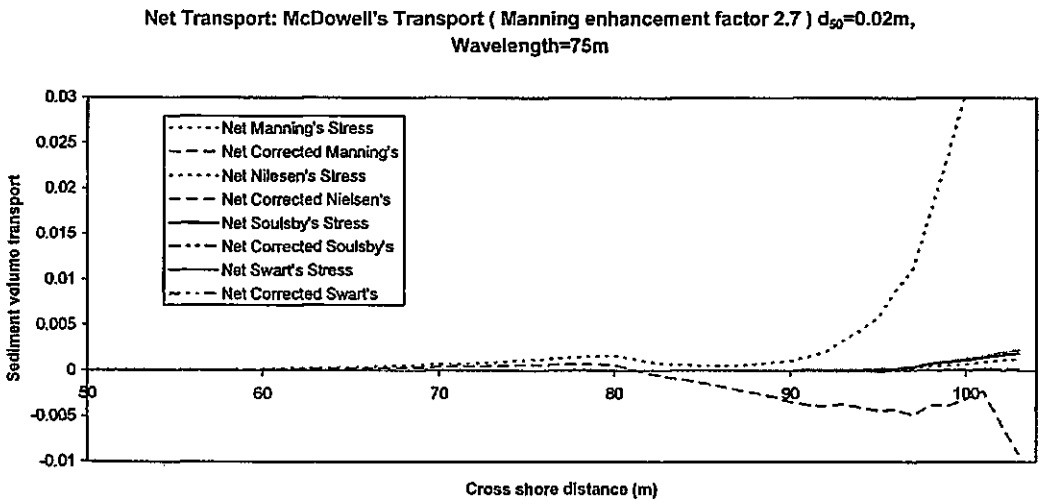

Figure 74 Wave period net transport rates, McDowell's formula

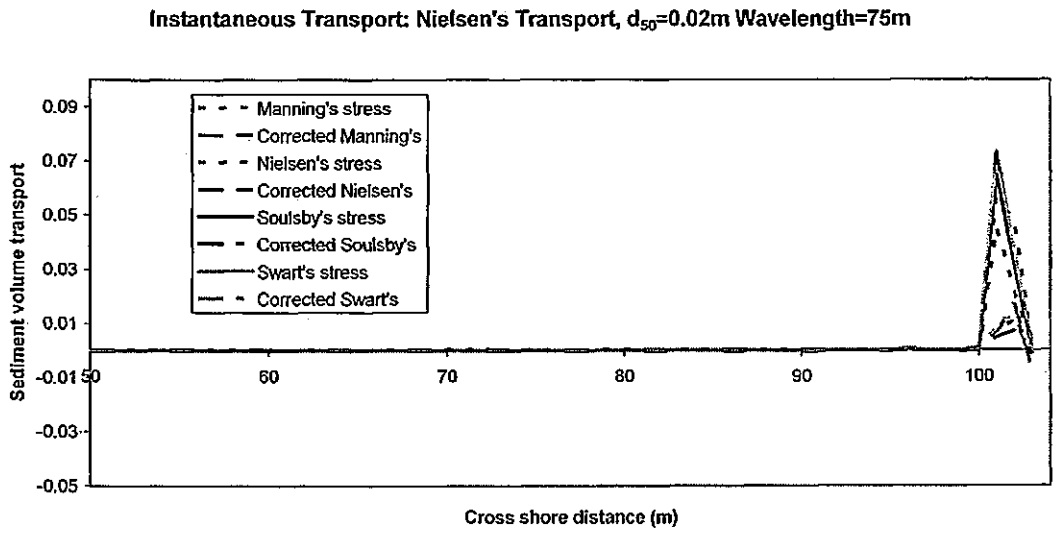

Figure 75 Instantaneous transport rates, Nielsen's formula

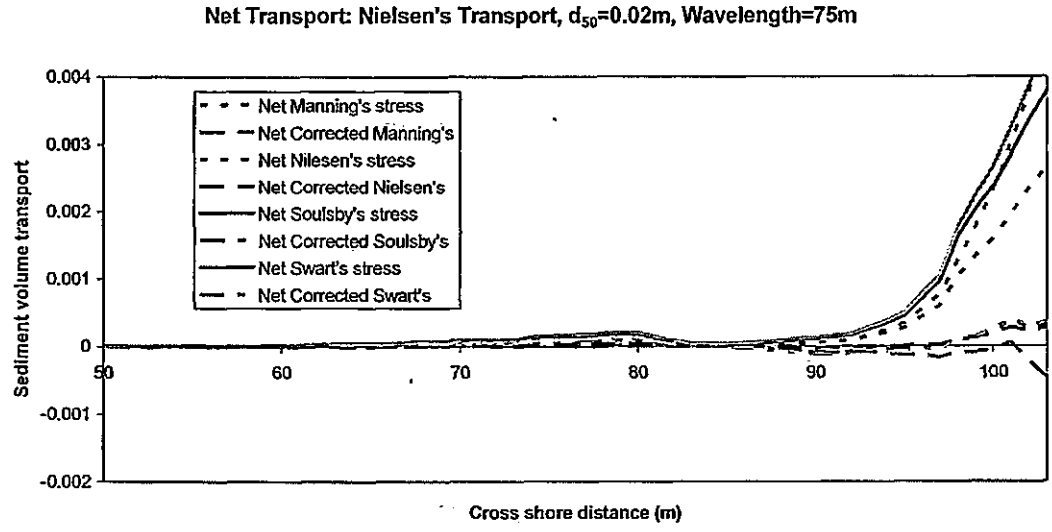

Figure 76 Wave period net transport rates, Nielsen's formula

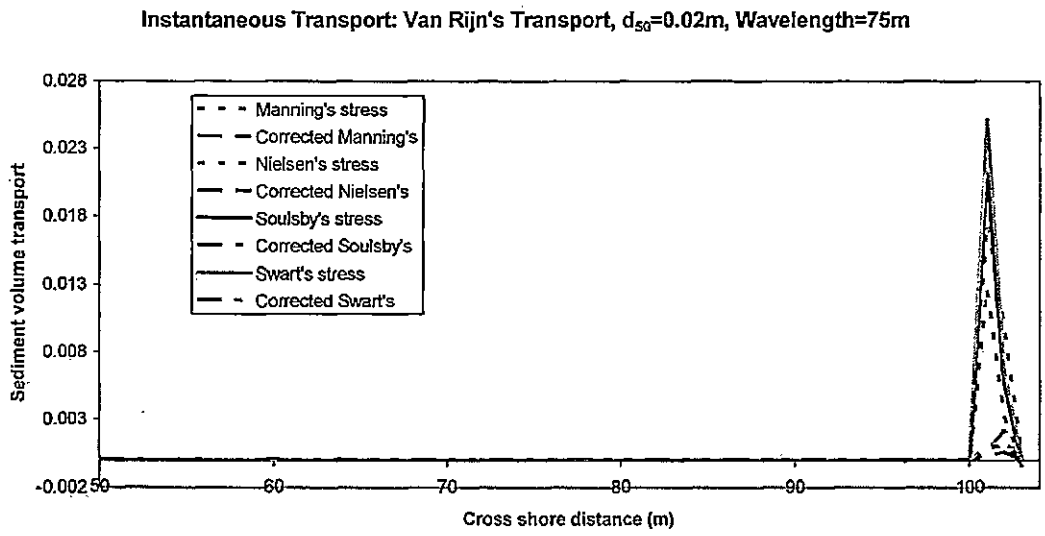

Figure 77 Instantaneous transport rates, van Rijn's formula

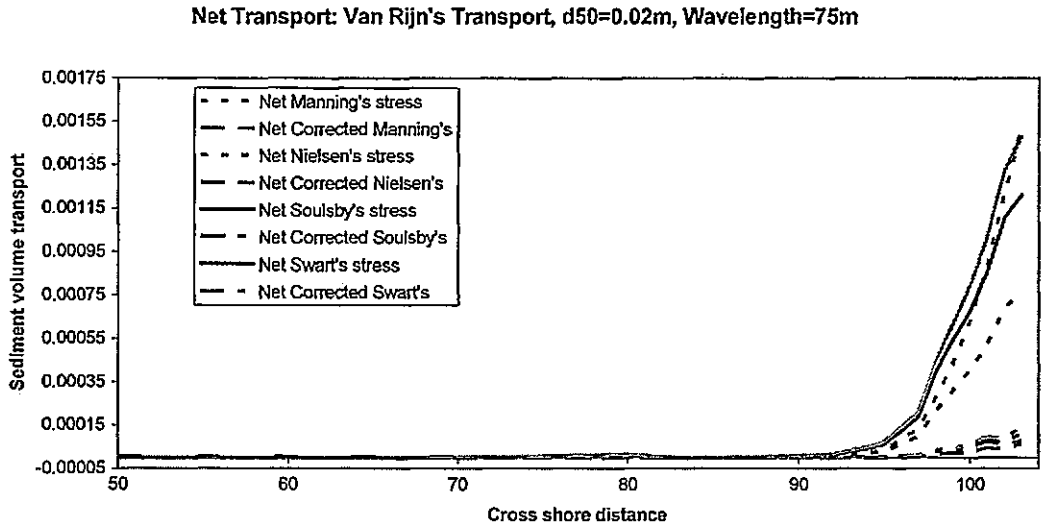

Figure 78 Wave period net transport rates, van Rijn's formula

Here the importance of the undertow correction can be seen. Without the correction essentially all the transport is calculated as onshore, regardless of the hydrodynamic conditions.

In fact, the McDowell transport formula only calculates net transports comparable to Nielsen's and Van Rijn's transport rated when used with Manning's stress formula and with the Manning enhancement factor of Packwood and Chadwick.

Using Nielsen's or Van Rijn's transports, Manning's stress generally predicts the least magnitude of net transport, and Swart's stress predicts the greatest.

There is no obvious optimum combination of these formulae from the physical point of view, as the overall predictions agree to an order of magnitude. In view of this, in the final evolving bed numerical model, the simplest computational choices have been made for the shear stress and transport rate formulae, that is: Soulsby's stress formulation and Nielsen's transport formulation.

4.4. Multiple grain size transport

To extend the sediment transport model to a set of grain sizes, a hiding function approach has been taken. This modifies the shear stress according to the relative presence of different grain sizes. A good introduction to this is given in Kleinhans and van Rijn, (2002). The procedure is outlined below.

Since the sediment mixture is in fact time varying, the critical shear stress is actually a function of time. That is to say,

$$\tau_{cr} = \tau_{cr}(d_{50}(t)) \tag{51}$$

The critical shear stress for each sediment fraction may then be calculated according to

$$\frac{\tau_{cr,f}}{\tau_{cr}} = \left(\frac{d_{50,f}}{d_{50}(t)} \right)^{c} \tag{52}$$

where $\tau_{cr,f}$ is the critical shear stress for the fraction f and $d_{50,f}$ indicates the d_{50} of the fraction f. c is an empirical parameter which takes a value between 0 and -1. Using the value c = 0 corresponds to not correcting the Shields values at all, and using the value c = -1 corresponds to using an identical critical bed shear stress for all size fractions. Kleinhans and van Rijn, (2002) discuss previous works estimating values of c and report an average observed value of approximately -0.65.

Finally, the volume transport rate for each fraction f may be calculated from

$$q_{s,f} = q\left(\tau_b, \tau_{cr,f}\right)$$
$$q_s = \sum_f q_{s,f} \tag{53}$$

which replaces Equation 48.

5. Sloping Beach Morphology Application

5.1. Previous work

Roelvink and Brøker, (1993) review a set of process based models. However, all these models are based on phase-averaged wave models. These are restricted by a number of inherent assumptions in the models chosen. Typically the models have no direct treatment of long-waves or wave asymmetry. Such a models reliability is also restricted to regions of quasi-uniform flow, whereas in the vicinity of the breakpoint the flow is highly non-uniform. This requires further (empirical) approximations to treat the transition zone inshore.

Rakha *et al.*, (1997) described a model based on the Boussinesq equations. An oscillatory boundary layer model, based on an momentum integral method, formed the interface between the hydrodynamics and the sediment transport. The boundary layer was assumed to grow from a zero thickness at each velocity zero-crossing. Suspended sediment transport was included, coupled with an eddy-viscosity model. Long *et al.*, (2005) describe another Boussinesq based model. Again a boundary layer model is included, this time derived from a Reynolds averaging of the Navier-Stokes equation at the boundary. Both of these models have been used to study sand beaches.

This chapter describes a coupling of a Boussinesq based model to a sediment model for coarse grains. Since the grain size is relatively large, the grains are larger than the boundary layer thickness, so boundary layer effects will be neglected. This will also improve computational speed for the model.

5.2. Single grain sized morphology model

The fully developed, interacting numerical model is implemented by adding an evolving bed morphology routine. The bed evolution is calculated by applying the law of conservation of mass to the sediment transport rates described in the previous chapter. For the single grain model this may be written

$$\frac{\partial Z}{\partial t} + \frac{1}{(1-n)} \frac{\partial q}{\partial x} = 0 \qquad (54)$$

where

Z = depth of sea bed, and

n = sediment porosity.

The depth Z need not be on the same origin as the fluid; providing the sea bed with its own frame of reference allows a convenient representation for calculating bed level changes independently of tidal sea level changes. This equation is a type of advection equation, but the sediment velocities are never evaluated, just the overall mass transport rates. The bed evolution is solved by an upwinded implicit finite difference scheme. The morphology model has a single independent variable, the bed level, which is solved alongside the Boussinesq variables, making a coupled equation set. In the sloping beach version of the model (using the slot boundary condition), it has been found necessary to apply a numerical filter to the bed evolution to remove high frequency numerical noise from the calculations. This was applied in the form of a low pass numerical filter applied to the sea bed depth changes. This is similar to the filter used by Kennedy *et al.*, (2000) in their hydrodynamic model.

Rakha *et al.*, (1997) implemented a similar morphology routine, but used a modified Lax's method for the bed update procedure. This also needed a filter for stability, with the filter was applied to the modified Lax's morphology routine.

The first trial for the combined model studied the 1:20 beach slope, commencing in a channel of 2m depth, with a 5mm grain size and a 3s period, 0.5m wave height. The initial wave crest, wave trough and mwl positions are shown in Figure 79. The model was run to simulate 2 hours duration of wave action.

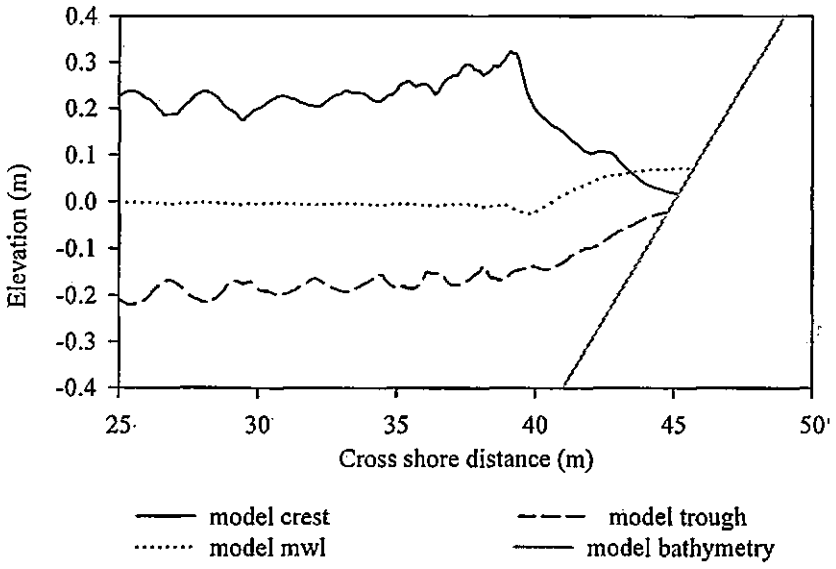

Figure 79 Initial hydrodynamic conditions, 3s, 0.5m wave, 1:20 slope

A sequence of bed profiles through the 2 hour simulation is given in Figures 80 and 81. In Figure 80 the evolution in the first hour is show at 15 minute intervals, with the graphs vertically staggered for clarity. The initial profile is also shown against each evolved profile to show the changes.

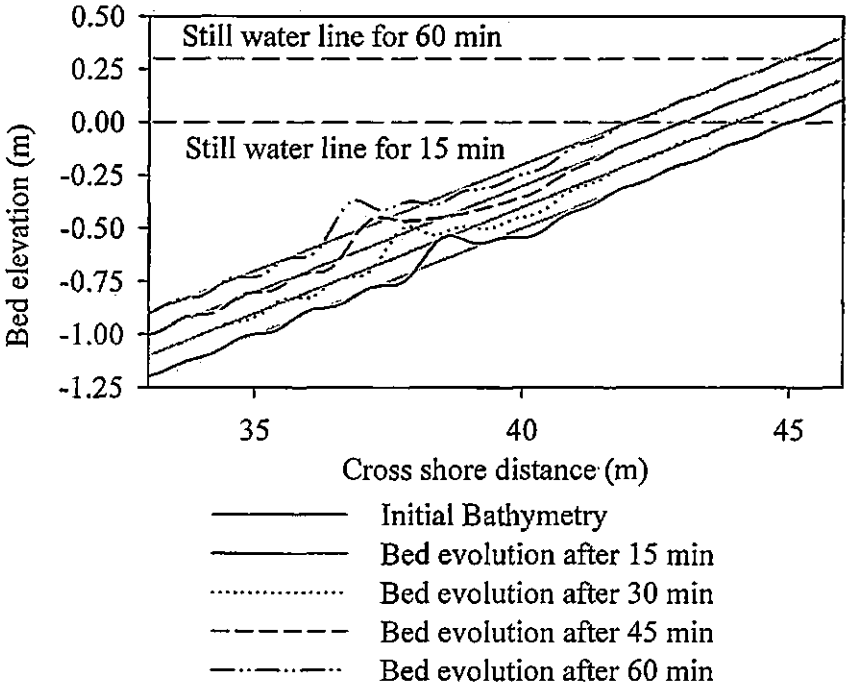

Figure 80 Evolution of 1:20 slope bed, first hour

In the first hour a bar is seen developing before moving offshore. The bar is generally located under the surf zone.

In Figure 81 the bed evolution over the second hour is shown in a similar manner. The bed continues to evolve and in this run does not seem to be approaching a steady state.

This is qualitatively similar to a result of Rakha *et al.*, (1997), which also generates a bar migrating offshore, however the substantive cases studied are very different.

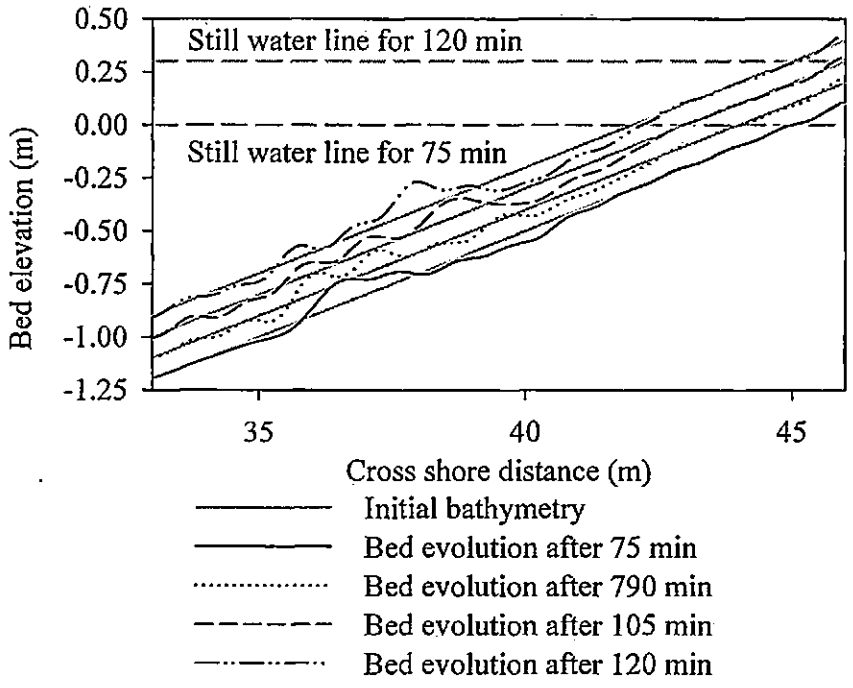

Figure 81 Evolution of 1:20 slope bed, second hour

To illustrate the changing nature of the sediment transport rates as the sea bed evolves, net transport rates over a single wave period are shown in figures 82 and 83. Figure 82 shows the net rate over the time interval of 29s – 32s, and Figure 83 shows the net rate over the interval 70s - 73s.

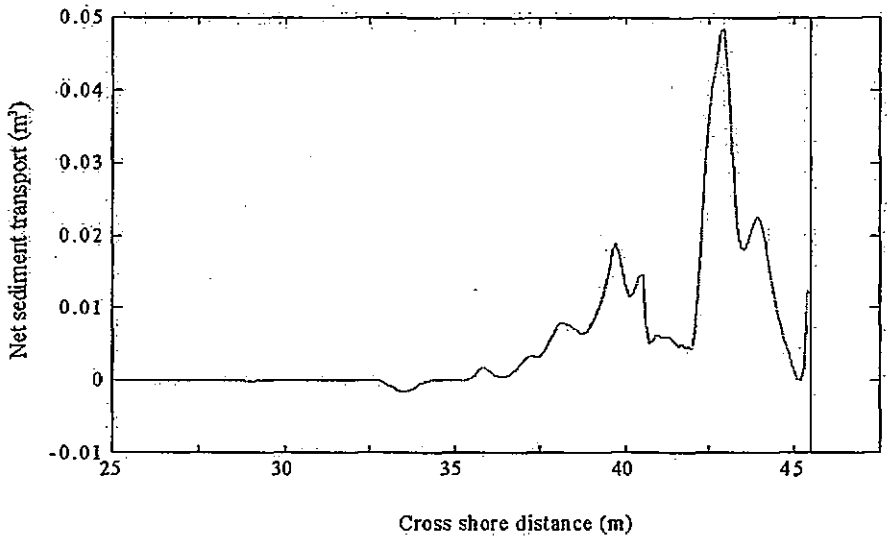

Figure 82 Net sediment transport rate, 29s – 32s

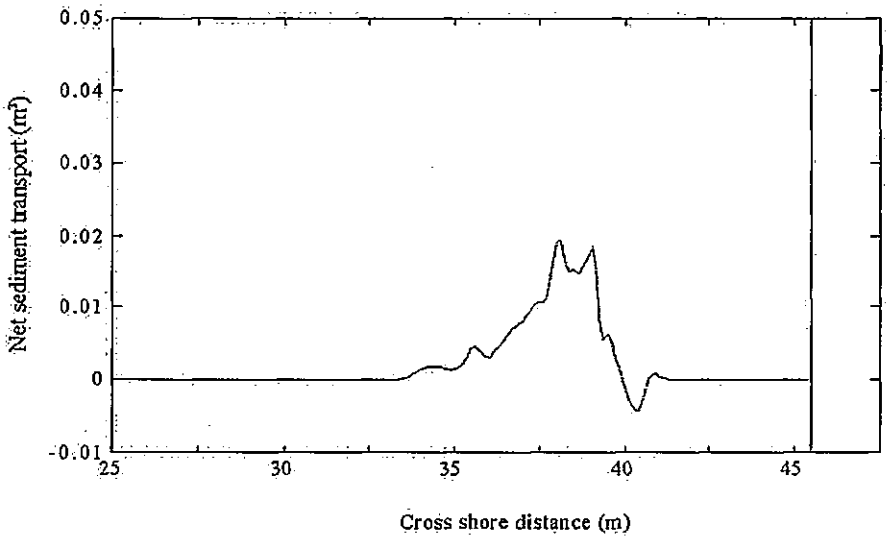

Figure 83 Net sediment transport rate, 70s – 73s

In Figure 82 the onshore accretion is significantly larger than in Figure 83 and exists closer to the still water line. This illustrates the significance of changes that may occur in the sediment transport regime over short time scales.

A second run was performed with a 1:10 sloped beach and a 6mm grain size. The bed evolution from this run is shown in Figure 84.

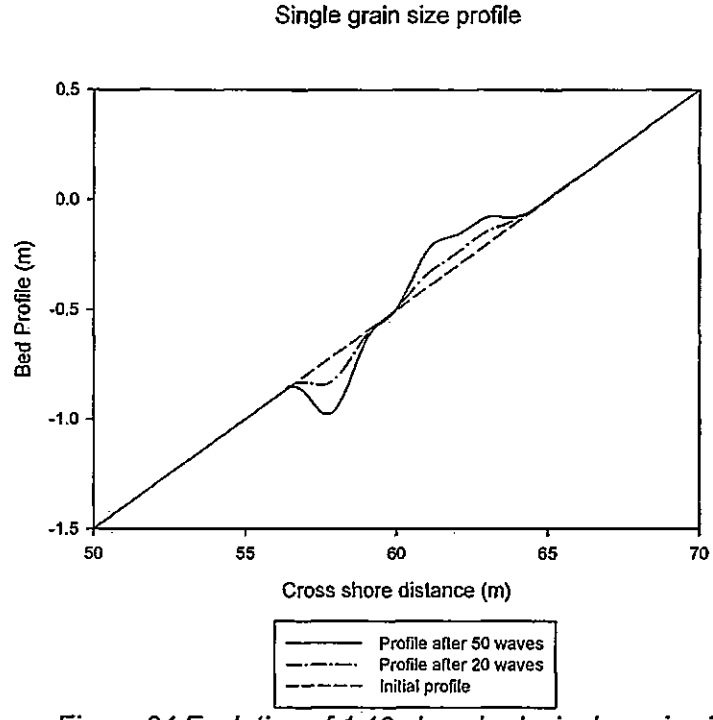

Figure 84 Evolution of 1:10 slope bed, single grain size

This shows accretion nearer the shore, leading to steepening of the beach face. It is also approaching a steady state much faster than the previous case.

5.3. Multiple grain sized morphology model

The multiple grain sized morphology model integrates the sediment transport rates in a similar manner to the single grain sized model, but now summing over all the transported fractions. Changes in seabed level are therefore calculated by

$$\frac{\partial Z}{\partial t} + \frac{1}{(1-n)} \sum_f \frac{\partial q_{s,f}}{\partial x} = 0 \qquad 55$$

where f = fraction index, and other quantities are with the same notation as before. For the mix of grain sizes considered here the sediment porosity n is taken as a constant, but for a mix of sand and shingle this should be time varying.

The sediment fractions are also individually sorted by also considering the conservation of mass of the separate fractions. The morphodynamic now model consists of a layer of sediment available for transport, called the active layer, of thickness δ which rests on the sediment substrate. δ is an adjustable parameter. Sediment becomes mobile

by erosion from this active layer, and is deposited onto this layer. The full expression for the calculation is given in Equation 56.

$$\frac{\partial}{\partial t}\left(p_f \delta\right) + p_f \left(\frac{\partial Z}{\partial t} - \frac{\partial \delta}{\partial t}\right) u\left(\frac{\partial Z}{\partial t} - \frac{\partial \delta}{\partial t}\right) + p_{0,f} \left(\frac{\partial Z}{\partial t} - \frac{\partial \delta}{\partial t}\right) u\left(-\frac{\partial Z}{\partial t} + \frac{\partial \delta}{\partial t}\right) + \frac{\partial q_{s,f}}{\partial x} = 0 \tag{56}$$

p_f and $p_{0,f}$ denote the percentage of fraction f present in the active layer and the substrate respectively. A model of this type has been used by Pender and Li (1996) to study river sediments. (It is not strictly conservative, as the substrate sediment ratios never change. This can be improved by a multi-layer approach, but with a consequent increase in computational time.)

The exchange rate of sediment between the active layer and the mobile sediment is the second term of Equation 56. This is determined by the rate of change of the sea bed level, and the erosion rate of the sediment. As the depth of the seabed changes, the interface between the substrate and the active layer moves accordingly. Sediment therefore numerically migrates between the substrate and the active layer, and this exchange rate is the third term of Equation 56. A schematic of the sediment layers is shown in Figure 85.

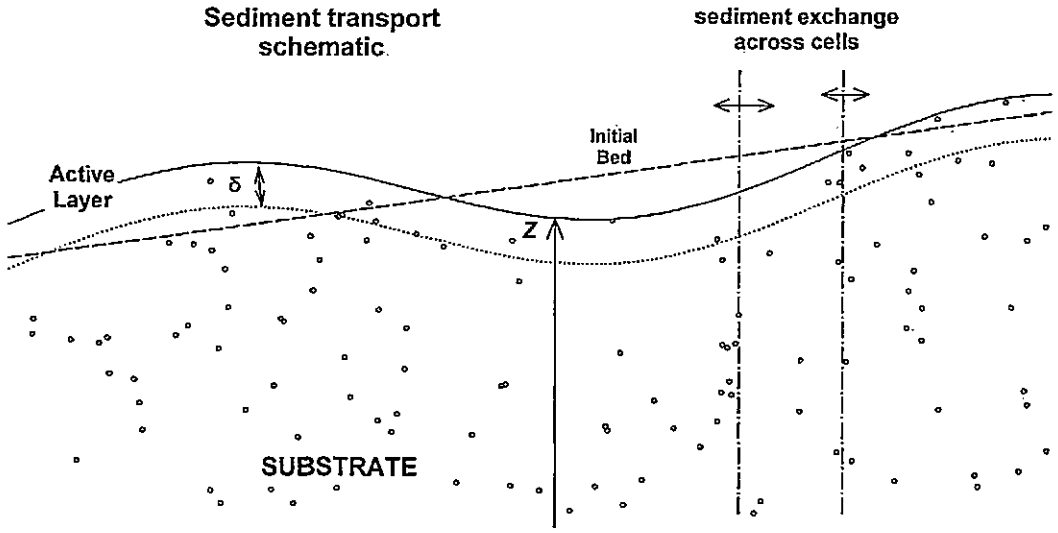

Figure 85 Multiple grain size sorting schematic

The model was run with an initial sediment composition with a mean d_{50} of 6mm, and with the initial grain size distribution shown in Figure 86 applied throughout the model. The bed slope was 1:10 and the wave was a 3s period, 0.5m wave height as in the single grain size case above.

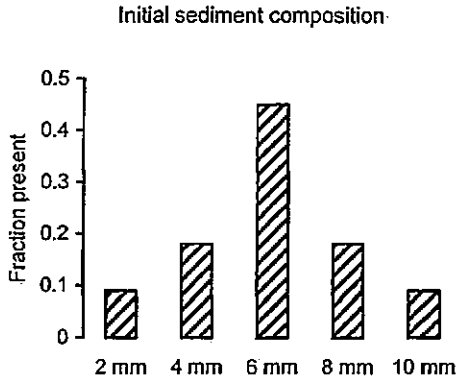

Figure 86 Multiple grain size initial distribution

The evolved profile for this case is shown in Figure 87.

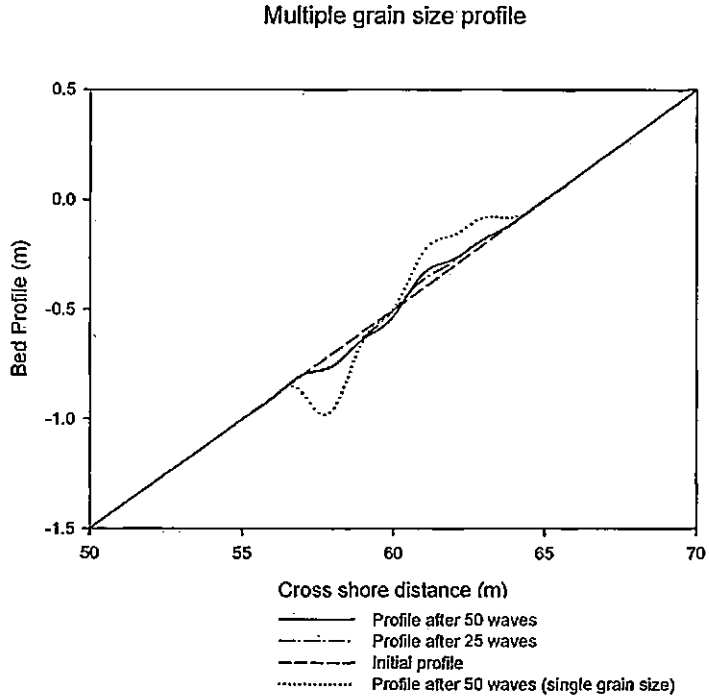

Figure 87 Evolution of 1:10 slope bed, multiple grain sizes

While showing similar characteristics to the single grain size run, it is clear that the overall movement of sediment is much reduced for this case. This agrees with the finding of Román-Blanco and Holmes, (2003) in a large scale experiment.

For the multiple grain size runs the changes of sediment composition through the run may also be examined. The cross shore profiles of relative sediment presence (e.g. a presence of 0.1 indicates 10% of the material is within that fraction) are shown in Figure 88, after 25 and 50 waves, corresponding to the bed profiles in Figure 87. The initial condition from Figure 86 is shown as the horizontal dotted lines.

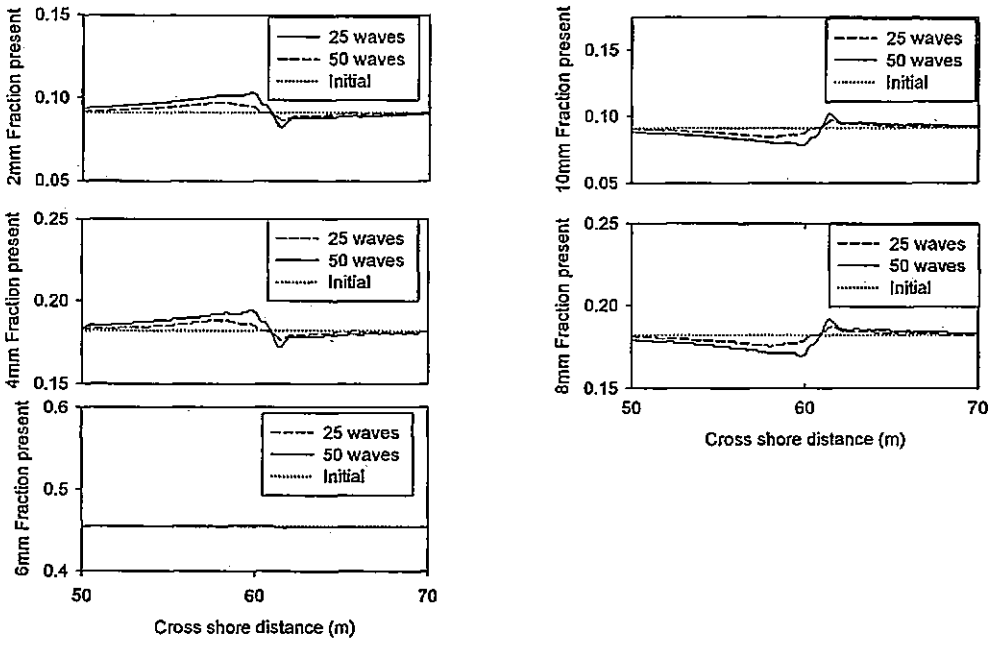

Figure 88 Sediment composition, final distribution

This figure shows the change in sediment composition increasing with time. There is an increase in the quantity of the coarse grains present in the onshore direction, and a corresponding derease in the quantity of fine grains present. There is also a decrease in the quantity of the coarse grains present in the offshore direction, and a corresponding increase in the quantity of fine grains present.

These runs show the types of prediction possible with the sloped beach model. However, the shoreline boundary is rather problematic. In practice, the slot parameters and filtering necessary to study a particular beach case must be found by trial and error, which is very time consuming. The use of filtering also causes inaccuracies in the evolved profile calculations, smoothing out short scale bed forms that may evolve. In particular, much detail is lost at the swash zone.

The model may also be applied to the study of beaches terminated by a submerged seawall, by changing the appropriate boundary conditions. In fact, a major limitation of the present model is the behaviour in very shallow water. The numerical

scheme is stable in deep water, and so may applied to the sea wall case without the need for any smoothing. The use of such a model is described in the next chapter.

6. Beach Morphology with a Sea Wall

6.1. Previous work

A sea wall may be placed on a beach to prevent landward retreat of the shoreline, or to prevent flooding due to high sea levels. The wave regime on the beach is then considerably modified. If the beach material adjacent to the wall is removed by wave action is removed, then the wall may fail. A number of physical experiments have been carried out over the years to understand this case. Russell and Inglis, (1953) provide one of the earliest, and this appears to be the only study that considered the effects of tides. They suggested scour would stop at about one wave-height below low water. Irie and Nadaoka, (1984) and Xie, (1985) found two patterns of sediment evolution under standing wave fields, that are now called *P-type* and *N-type*. For fine sediments, the P-type transport from the wave nodes to the antinodes has been observed and for coarser sediments the N-type pattern of transport from the antinodes to the nodes has been observed. There is also the SUPERTANK experiment reported by Kraus and Smith, (1994), and many others. A good review of the subject is found in DEFRA, (2003).

As with plane beaches, more work has been performed on sandy beaches than shingle beaches. Powell and Lowe, (1994) investigated toe scour in a physical model for nominally coarse sediment (actually graded anthracite) that was scaled to a d_{50} of 5mm < d < 30mm, and measured the response of a beach to a number wave fields. The wave flume was physically scaled at 1:17. They found a zone of erosion associated with wave reflection generally within the space of

$$1 < D_w/H_s < 3 \qquad (57)$$

where D_w is the depth of water at the structure toe, and H_s is the significant wave height. Their results are reproduced in Figure 89

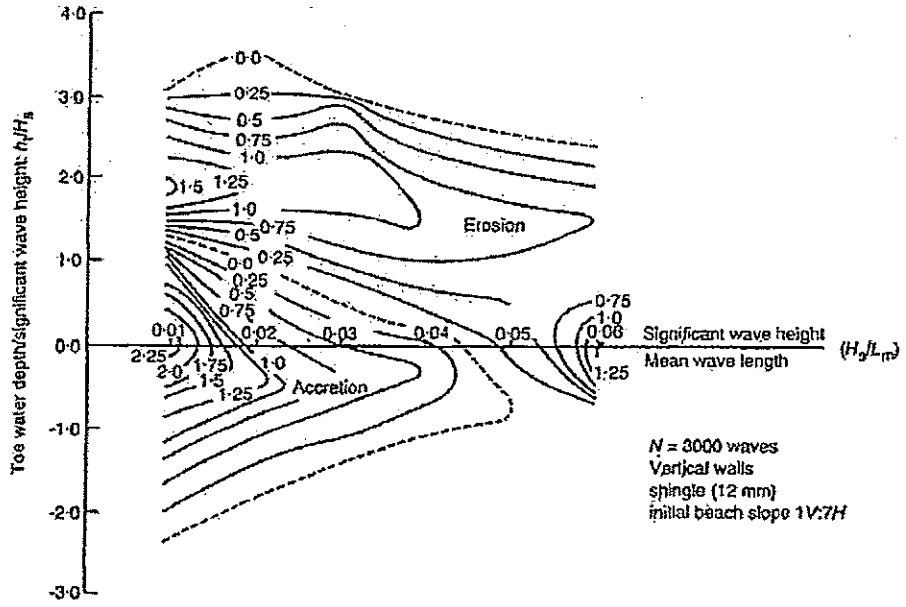

Figure 89 Experimental contours of toe scour, Powell and Lowe, (1994)

A theoretical study of wave reflection was made by Longuet-Higgins, (1953) where rotating cells develop in a boundary layer. The main body of fluid then rotates in the opposite sense above this boundary. A schematic is shown in Figure 90

Bed load transport within the boundary has been suggested as a mechanism for the development of the N-type flow, and suspended load sediment in the main flow has been suggested as a mechanism for the P-type flow.

A numerical model with no boundary layer cannot reproduce these rotating cells. However, such cells are derived for a fully developed flow, whereas in most cases of interest, an constantly varying incident wave field does not allow a steady state to develop. Wave asymmetry-induced transport however does not require the flow to be fully developed, and may be present for any non-linear or partial reflection case. Accordingly it may be a complementary mechanism for sediment transport.

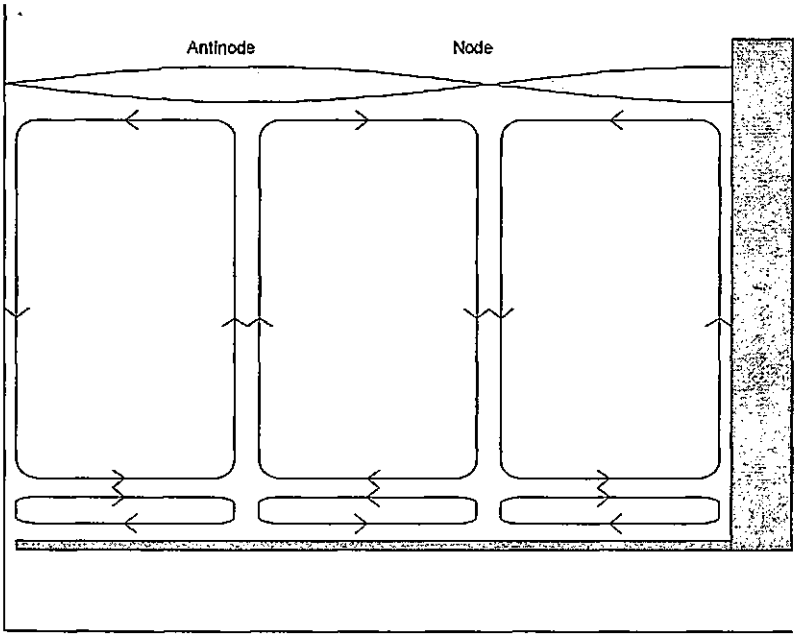

Figure 90 Boundary layer currents under standing wave

Numerical models for the sea-wall case are again sparse. Recently, McDougal *et al.*, (1996) have presented a wave-averaged model for a sandy sediment, and Rakha and Kamphuis, (1997) have presented a model driven by a Navier-Stokes solver also for a sandy sediment. Lawrence *et al.*, (2003) have presented a coarse grained sediment transport model coupled with a Boussinesq hydrodynamic model, and further results from this model are given in this chapter.

6.2. Sea wall model

Combining the numerical sediment techniques of the previous chapter to a reflecting wall hydrodynamic model such as in section 3.4 allows a simulation of the wave flow and beach evolution for a sloping beach with a sea wall located seaward of the natural still water line. In this case there is very little need for numerical filtering. Some high frequency noise has been observed in the Boussinesq model, but a filter at every hour of simulated time is sufficient to remove it.

The combined numerical model was set up with a deep channel section of a still water depth of 10m. At the shoreward end of the tank, a plane slope of 1:10, rising to a depth of 3m was placed, ending with the vertical wall. A regular Cnoidal wave series of period 8s was run, with a grain size of 15mm. This was allowed to run to a steady state sea-bed profile, taking approximately 2500s. A series of the resulting profiles is shown in Figure 91

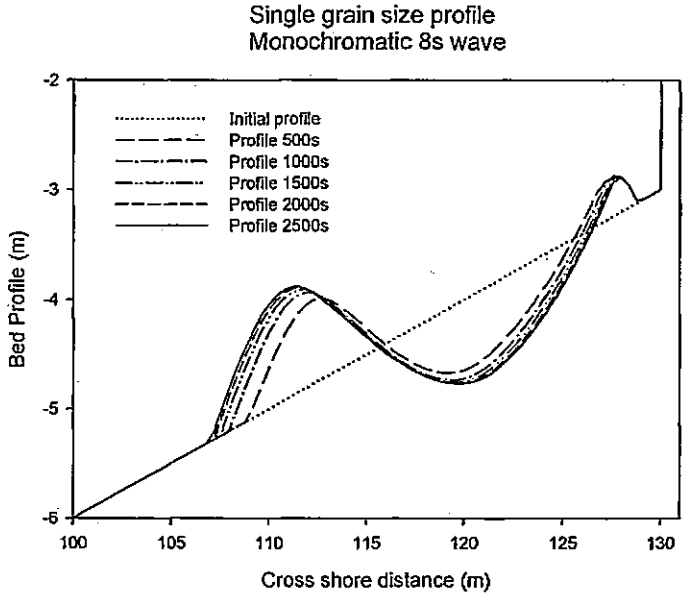

Figure 91 Evolution of 1:10 slope bed, 8s monochromatic wave

This shows a region of accretion close to, but not adjacent to the sea wall. There is then a wider zone of erosion further offshore, and also a corresponding zone of accretion offshore. The pattern is generally of N-type motion. Since the hydrodynamic model assumes a zero flow condition at the sea wall, the modelled velocities adjacent to the sea wall are low, in accordance with the standing wave profile. Therefore, the bed shear stress predicted is always less than the critical shear stress, and no sediment motion due to wave action is modelled in this zone. However, sediment is still able to move due to slumping, to preserve slope stability.

A similar case but for a wave period of 5s was also run. The resulting profile is shown in Figure 92

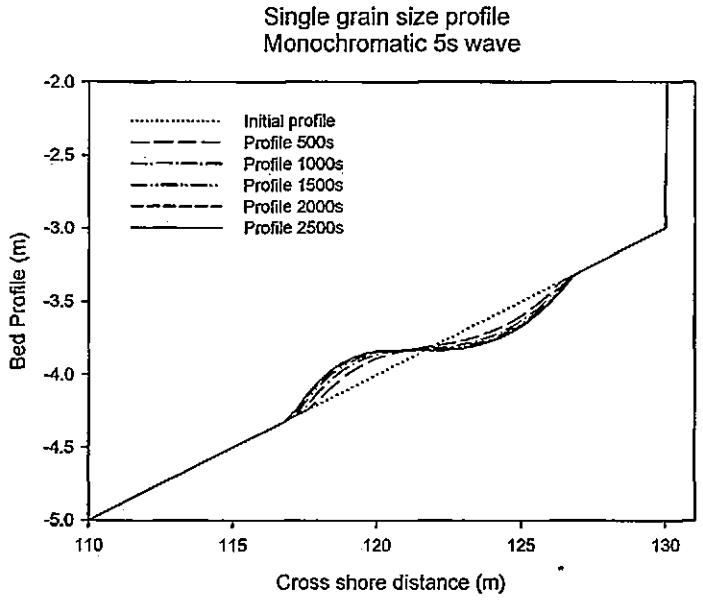

Figure 92 Evolution of 1:10 slope bed, 5s monochromatic wave

Here there is no accretion near the sea wall. Since the 5s wave has a shorter wavelength, the morphological 'cell' in which the bed moves has a narrower width. Overall this run shows lower amounts of sediment movement, but is otherwise showing the same general features as seen in Figure 91.

A random wave series was also chosen for a comparison. An irregular wave series of mean period 8s was run in a similar manner in the same numerical wave tank. The friction factor formula (Equation 43) used above could no longer apply; this formula requires constant orbital motion, and therefore constant wave period. Instead, the friction factor was held fixed at the value of f_w =0.04. This corresponds to the regular wave motion at a depth of approximately 4m. The bed profile from this run is shown in Figure 93.

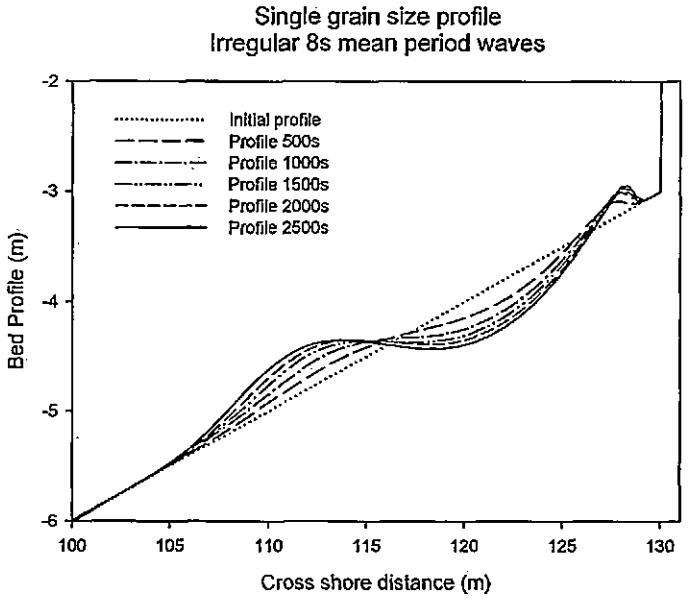

Figure 93 Evolution of 1:10 slope bed, 8s mean period irregular waves

The same general characteristics as the regular wave can be seen, although the overall change in bed profile is less significant. This is in agreement with the finding of Hughes and Fowler, (1991) that irregular waves caused less erosion than regular waves.

The physical dimensions of the coastal situation suggest two families of parameters for more detailed study. The first family describes the wave field, and consists of the wave height, wave period, bed slope and the toe-depth of the sea wall. A second family of parameters may be grouped by the flow characteristics of the sediment, in particular the friction factor and the grain size. Series of experiments have therefore been performed to study the behaviour of these parameter families. Further tests have also been made to show the capability of the sea wall model in the multiple grain size case, and in its use for simulating tidal situations.

6.3. Variation of wave characteristics

The irregular wave run referred to previously was taken as the base line run. The first comparison was made by varying the depth of the wall toe and the wave period. A set of model runs was generated for wave periods between 5s and 14s at 0.5s intervals, and

for toe depths varying from 1m to 6m in 0.25m intervals. A second comparison was then made by fixing the toe depth, but changing the bed slope to a value of 1:7. Figure 94 shows more illustrative patterns of the behaviour found, with an example of changed toe depth, and an example of changed bed slope. The depth axis for this figure has been normalised to indicate a toe depth equal to zero for all cases.

This shows clear differences in the sea-bed response to the variations in the bed slope. The magnitude of accretion adjacent to the toe (when it exists) is particularly sensitive to such changes. In this figure, the 2.5m toe depth run has the overall shallowest water depths, and shows the largest morphological changes. For the 3.5m toe depth runs, the 1:10 slope case and 1:7 slope case result in similar erosion/deposition patterns, and have distinct final steady states.

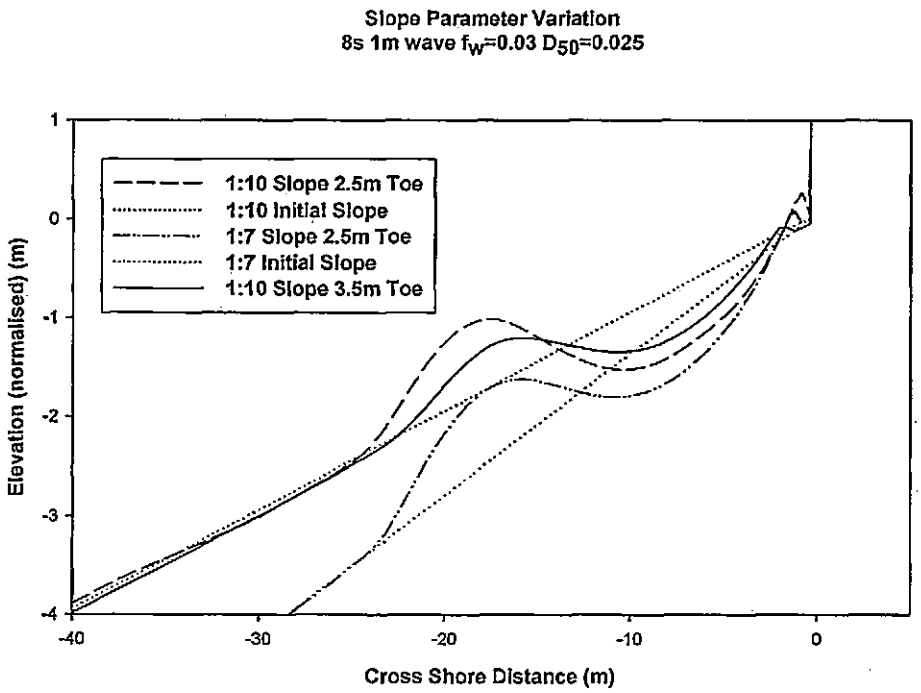

Figure 94 Wave characteristic comparison: 8s mean period irregular waves

The contour graph of the maximum relative erosion (erosion depth divided by significant wave height) across the numerical model profile while varying the wave period and toe depth for a 1:10 slope is presented in Figure 95.This figure is scaled to the same dimensionless parameters as in Powell and Lowe, (1994) (Figure 89).

A decrease in relative erosion is seen across this chart for increasing H_s/L_m. Another contour graph of the maximum relative erosion for varied toe depth and wave period with a bed slope of 1:7 is presented in Figure 96. Again, a decrease in relative erosion is found with increasing H_s/L_m. The general slope of the contours is similar to the corresponding region of Figure 89.

In both cases, the model is unable to make predictions for the full range of wave period and toe depth cases stated above. As the bed evolves, wave troughs touch the sea bed away from the sea wall, and further numerical code is required to handle these cases. For such regions of shallow water, the assumption of small ε (wave height divided by water depth) for the Boussinesq equations is in fact broken.

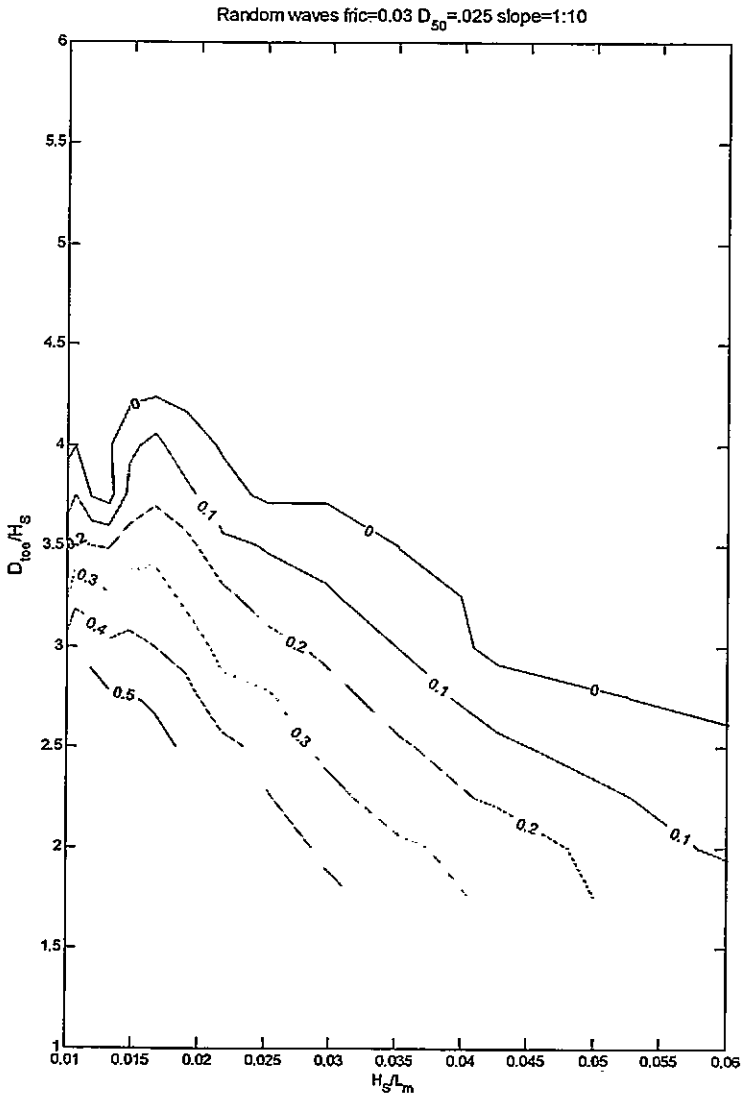

Figure 95 Contour graph of maximum toe erosion, 1:10 slope

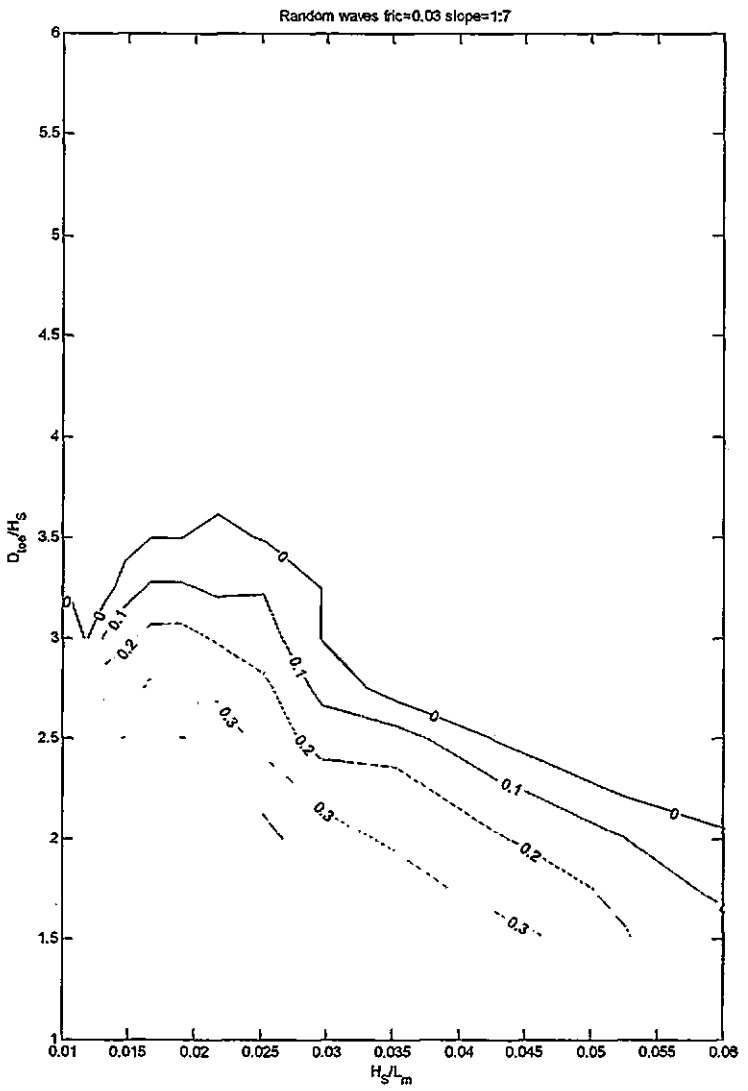

Figure 96 Contour graph of maximum toe erosion, 1:7 slope.

6.4. Variation of sediment characteristics

Similar runs were then performed to compare the effect of changing the friction factor and the sediment size. Changing the friction factor directly changes the shear stress acting on a grain, and therefore changes transport initiation and transport rates, according to Equations 40 and 50. Changing sediment grain size alters transport initiation

by altering the Shields parameter for the flow case. An illustrative figure for these changes is given in Figure 97.

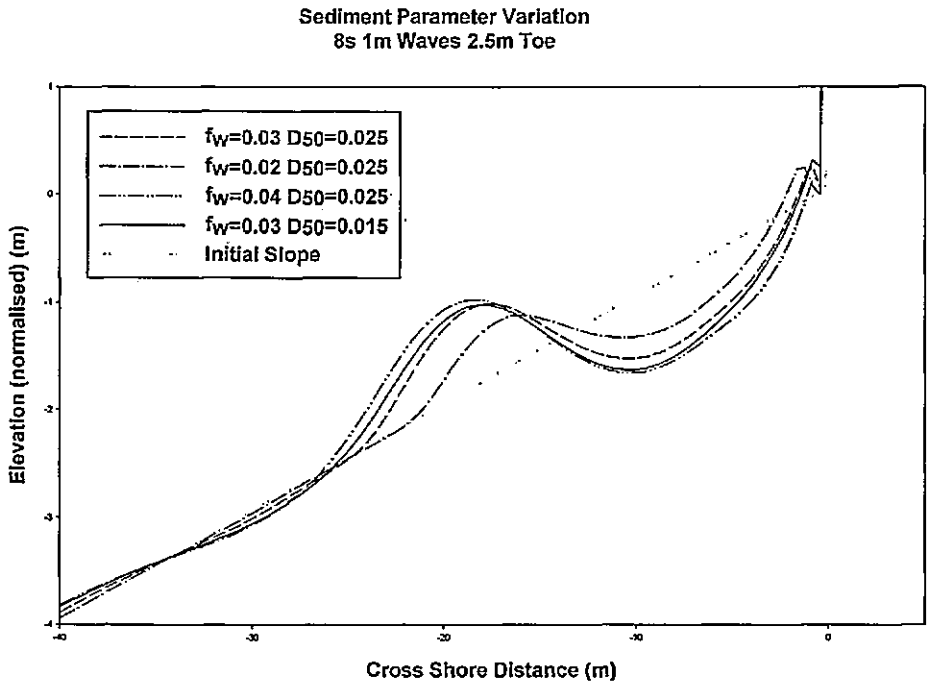

Figure 97 Variation of sediment flow characteristics

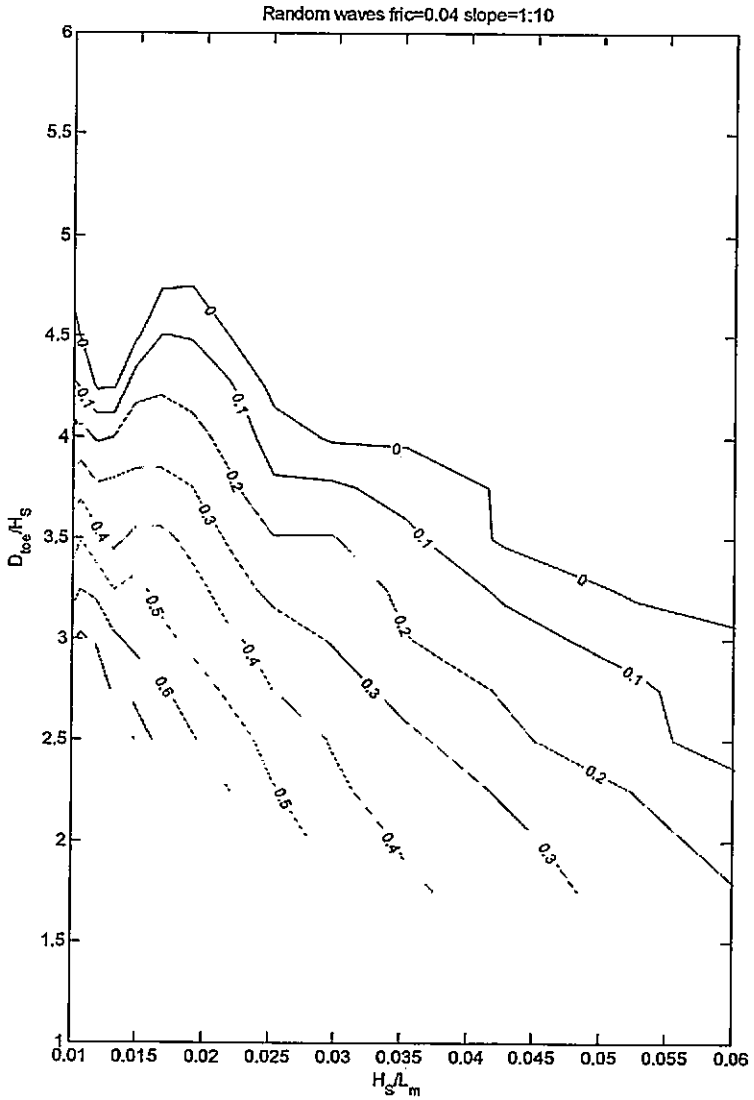

Figure 98 Contour graph of maximum toe scour, f_w = 0.04

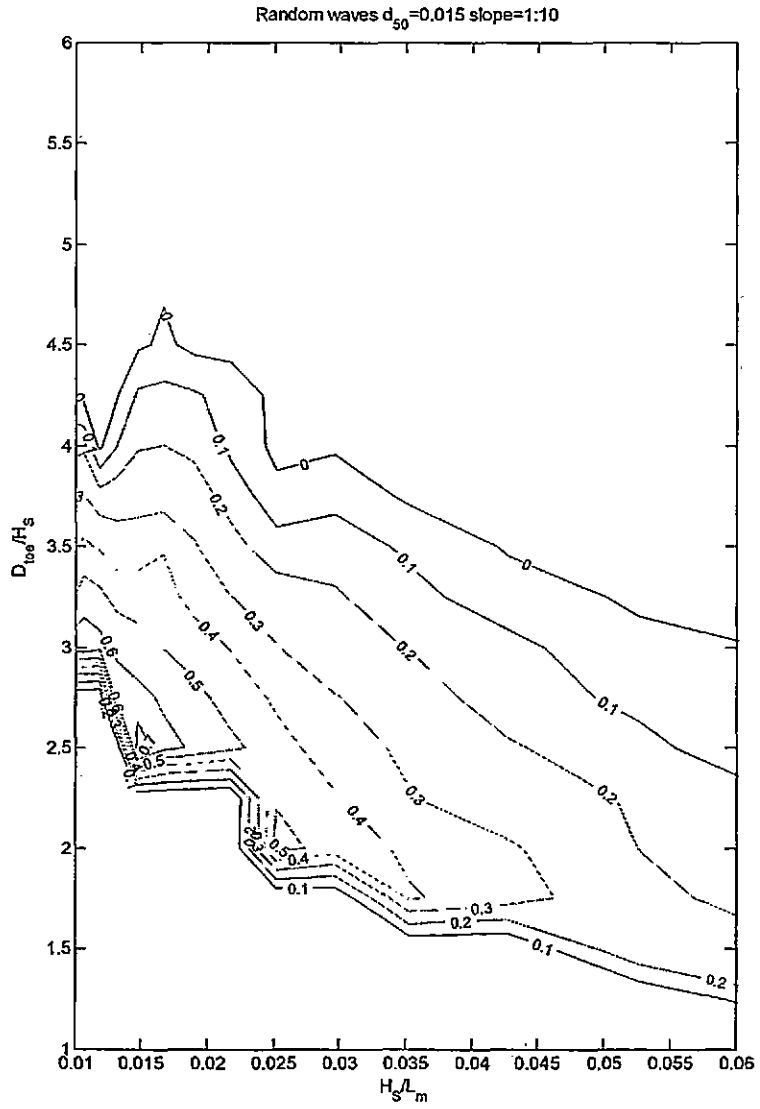

Figure 99 Contour graph of maximum toe scour, d_{50} *= 0.015.*

Figure 98 shows the erosion contour diagram for the increased friction factor case of f_w=0.04. Figure 99 shows the erosion diagram for the smaller d_{50} case of d_{50} =0.015. Again there is clearly variation across these parameters, but the overall pattern looks similar to that in Figure 89.

6.5. Multiple grain sizes

A single comparison run for the multiple grain size case was run, comparing to the baseline run in section 6.1 with the multiple size fractions as shown in Figure 100.

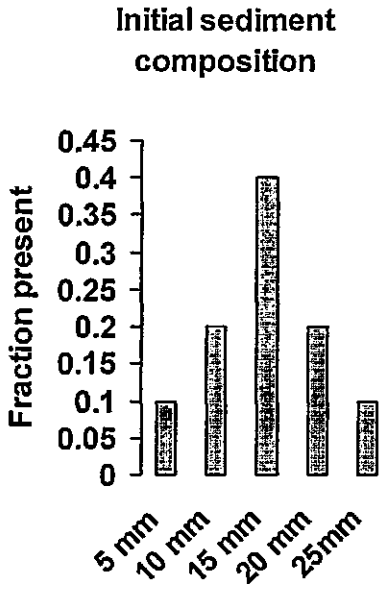

Figure 100 Initial sediment distribution.

The evolution of the bed profile with this sediment composition is shown in Figure 101, and is compared to the single grain size case. Figure 102 shows the final cross shore profile of the sediment fraction distribution.

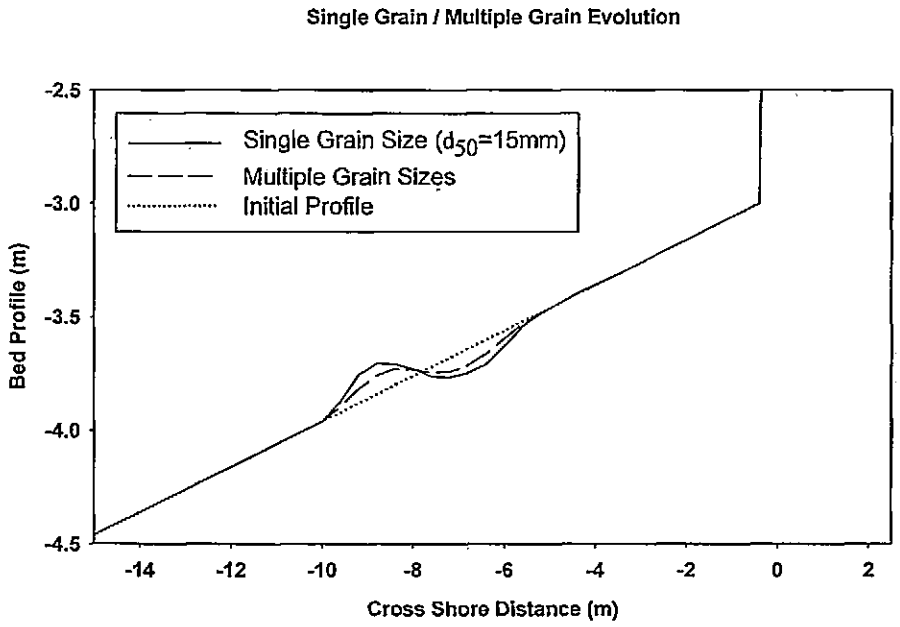

Figure 101 Comparison of single grain size and mixed grain sizes evolution

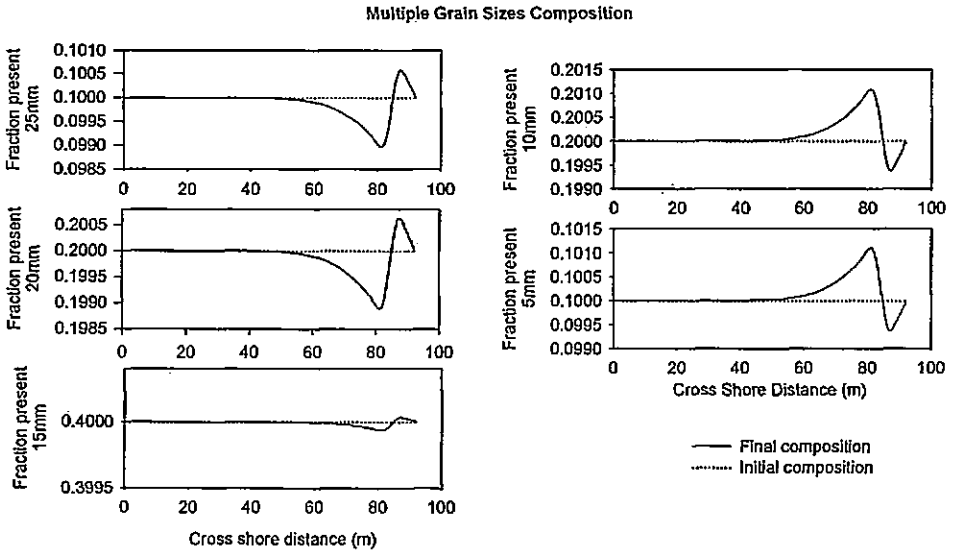

Figure 102 Cross shore distribution of sediment composition.

The magnitude of the bed change is reduced with the mixed sediment. After the run has reached a steady profile, the relative change in composition shows a predominance of the larger grains in the onshore erosional region, and a predominance of the smaller grains in the offshore depositional region.

6.6. Tidal effects

A final series of runs has been made to study the effect of tidal cycles on the erosion patterns. This is achieved by changing the still water level component of the model at successive timesteps, according to the tidal signal. A tidal range of 1m with a period of approximately 12.5 hours has been added to the conditions for the base line run. The model was run for 3 tidal cycles, and approached 'convergence' after about 1 cycle. A sequence of bed profiles is shown in figures 103 and 104, starting at high water for the third cycle.

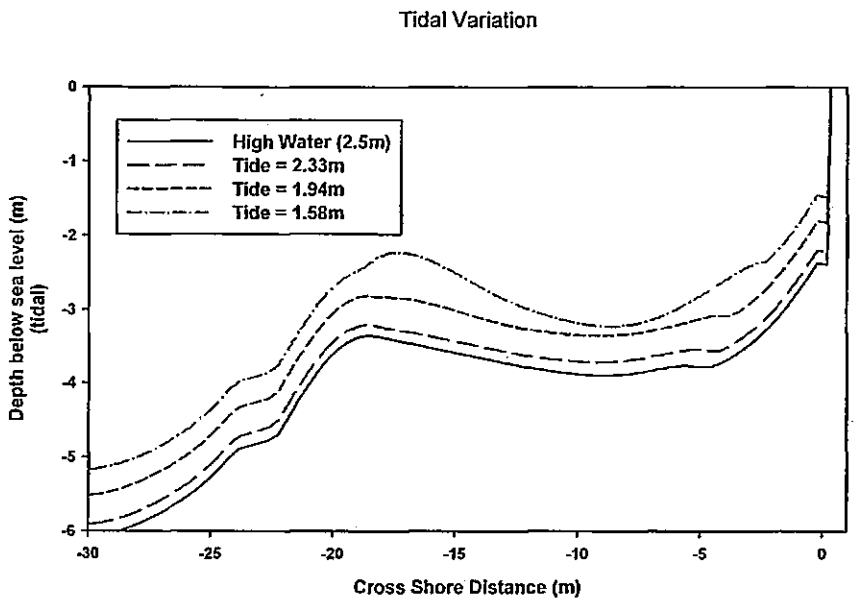

Figure 103 Bed evolution profiles – falling tide.

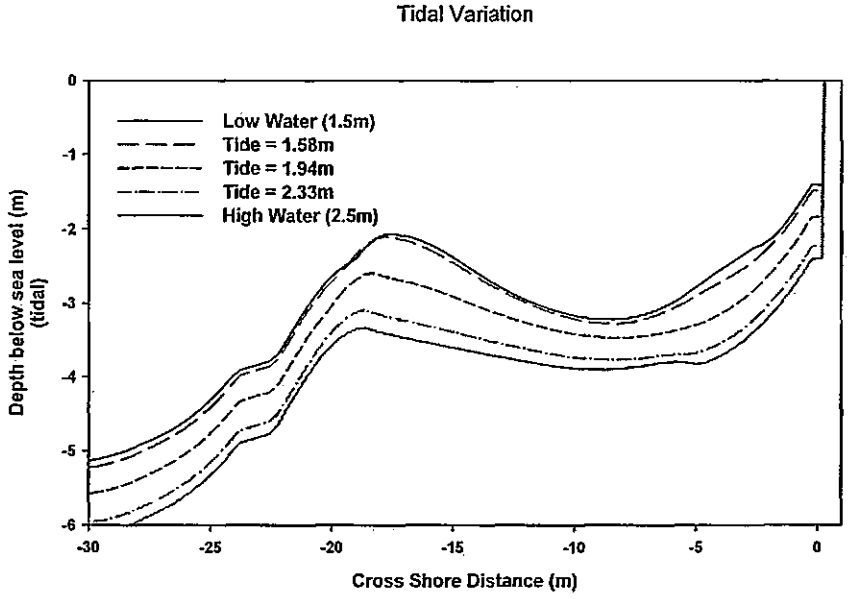

Figure 104 Bed evolution profiles – rising tide.

The maximum erosion is seen at low water, when the shoreline wavelength is shortest, and the profile responds relatively swiftly to the tidal changes. As the tide falls, material is moved both on and offshore from the maximum erosion position. As the tide subsequently rises, material returns from the on and offshore bars. The location of the offshore bar can also be seen changing its cross-shore position as the shoreline wavelength changes.

7. Conclusions

7.1. Summary

Boussinesq models for non-breaking waves are now well developed, and find good application for engineering applications. There are a number of higher order models now available. The performance of the present low order model is shown in Chapter 3, and is evaluated against the theory shown in Chapter 2. The hydrodynamic model is shown to reproduce observed wave elevations in a number of cases, and also to reproduce the depth mean velocities observed in the surf zone of a breaking wave. The model has also been applied to the case of a reflecting wave, and the accuracy of the predictions is shown with regard to the GWK experiment.

The model has then been used to study the interaction of wave shoaling and reflection in a series of numerical experiments. This demonstrates the effect of partial reflection occurring on a sloping bed and the transfer of energy between the higher harmonics in the resulting wave field. The consequent interactions between shoaling and reflection are then shown to generate a highly varying velocity skewness in the wave field, quite unlike that of either the incident or reflected wave, which must be taken into account in the development of a morphological response.

The experiments also show the contribution of wave non-linearity to the wave crest heights in the reflected field. The study of wave reflection with the Boussinesq model also shows very good performance at predicting the distribution of a standing wave. While there is no velocity data to confirm the model velocities, in the absence of wave breaking the predictions for the modelled velocity statistics are expected to be as good as for a progressive wave case.

In Chapter 3 a review of recent sediment transport formulae is given, and their predictions of sediment transport rates are compared. Predictions of friction made using Manning's law are shown to be significantly different from those using the friction factor laws for certain flows, partly due to the independence of Manning's law from the wave

characteristics. The flow predictions of McDowell's energetics approach are also shown to be different from the others given.

The influence of undertow is then shown on a set of wave fields, and the corresponding effect on bed shear stress and sediment transport rates is shown. The significance of this process is confirmed.

The morphology model is introduced in Chapter 5, applied to a sloping beach. The model is shown having a rapid response in the coupling of the morphology model to the hydrodynamic model, with the modified bed forms leading to changes in the transport rates and velocity field. The model is also shown making predictions of bed response over a long term simulation.

The extension of the model to a multiple grain size form is also shown, and a reduction in profile response due to mixed sediments is observed. This is consistent with experimental findings by Román-Blanco and Holmes, (2003). The ability of the model to track differential motion of sediment fractions is also demonstrated.

The morphology model is applied to the sea wall case in Chapter 6. The model is again shown providing long term simulations of the sea bed response. In general, the results show well defined N-type morphology patterns, with clear nodal zones of negligible sediment transport. The model is found to agree with the observation of Hughes and Fowler, (1991) that erosion is reduced under an irregular wave field compared to a regular wave field. The model also shows some agreement with the results of Powell and Lowe, (1994) in the trend of the erosion patterns. A series of sensitivity tests has then been performed with model, studying the behaviour of the model with regard to the incident wave field characteristics, and also with regard to changes in sediment characteristics. The model shows high variation with regard to all these properties.

The mixed grain-size model also demonstrates differential motion of sediment fractions for the sea wall case. As with the sloping beach model, the sea wall model predicts a reduction in profile change for a sediment mixture for nonbreaking waves.

The tidal model shows a consistent profile adjustment with tidal changes. The width of the morphological cell responds to changes in nearshore wave length, and the depth of scour responds directly to the tidal height. The profile is adjusting between the two extreme profiles that correspond to constant water depth for the high and low water values. The profile does not reach those limits, although it approaches them at slack water.

7.2. Discussion

The hydrodynamic model provides good estimates for the wave height in most of the cross-shore domain for waves of interest. The most significant shortcoming is the under-prediction of the breaking wave elevation, although the location of the breakpoint is well represented. The importance of the breaking wave elevation is dependent on the sediment model chosen. The McDowell formula uses an explicit wave height, whereas the friction factor approach is based on the wave orbital velocities. The velocity predictions of the model are generally overestimated near the break-point, but the skewness of the depth mean velocity is in good agreement with the physical data.

In general, higher order Boussinesq models can be expected to improve performance in hydrodynamic predictions. It will require further study to determine the relative benefits of computer time versus accuracy. The computational complexity of a Boussinesq model increases with the order. The numerical stencil of the present model covers 5 grid points (3 velocity and 2 elevation), but can be algebraically reduced to a tri-diagonal system. It only requires the storage of 2 time steps. The earlier higher order model of Wei *et al.*, (1995) requires storage of 3 time steps to fit a tri-diagonal system. The solver of Madsen *et al.*, (2002) uses a stencil of seven points and requires the solution to a banded matrix of 7 bands, requiring significantly more resources.

The development of the sediment model in Chapter 5 shows some useful initial results. The performance of the swash zone is disappointing however, and clearly much work need to be done to improve this. The results here are strongly affected by the

numerical filtering applied to the model, and a good choice of model will require the elimination of such filters. Otta and Acuña, (2005) show improved results in this area using a shoreline-fitting procedure. Other possibilities are a moving grid model such as that presented by Zhang, (1996), although this would need extending from the NLSW to the Boussinesq equations. Such a model would however provide an exact solution to the shoreline flow.

The morphodynamic predictions made so far with this model are.sparse. It shows a capability of generating similar features as a more complex model, but no extensive comparison has been made. The models are not applied to similar cases.

The predictions from the sea wall model in Chapter 6 are significantly improved. With the absence of filtering, there is no damping of the morphological evolution, and the bed features are clearly seen.

For the wave cases that the model is able to run, it has provided a general agreement with the erosion patterns shown by Powell and Lowe. There is clearly much variation within the model results. Unlike the algebraic model of Dean (1977), these experiments predict different steady state profiles for different initial bed slopes but otherwise identical incident waves. Since the bed further offshore has retained the initial bed slope, this can be expected to give each slope a unique wave shoaling response. Therefore the wave spectrum in the morphology cell adjacent to the sea wall is not uniform across all the profile tests, and so a uniform sediment response is not expected. This situation may change when more energetic waves, or a broader band wave spectrum is used, as this could widen the morphological cells. This is expected to result in changes further out in the seaward part of the bed profile.

The response of the model to the variation of sediment size and friction factor allows a tuning of the model to the Powell and Lowe findings. This has not been performed. The extent to which the Powell and Lowe Figure is really applicable is not clear. The diagram is based on scaled results, and the results may be true for a more restrictive band of d_{50} than stated. Powell and Whitehouse, (1998) provide a scour

diagram (from another numerical model) comparable to Powell and Lowe for a sandy sediment, and this is very different. Powell and Whitehouse also do not provide accretion predictions, due to limitations in the model they have used.

Less sediment sorting is observed in the mixed grain model for the sea wall case, compared to the sloping beach. However, the sediment is reacting to lower flow velocities in much deeper water. There are no indications of numerical instability in the sediment sorting.

There is scope for improvement of the sea wall model in two important aspects. Firstly the model does not accurately handle sediment transport immediately adjacent to the sea wall, due to the hydrodynamic assumptions. A full treatment of this is likely to need a turbulence model to account for sediment motion in this region.

Secondly, the model needs to handle a fuller range of incident wave fields and toe depths. This is related to the moving shoreline problem of the sloping beach model, and is expected to be solvable by similar methods.

The sediment model of Chapter 4 is based on recent work by various authors, but is not definitive. Recent studies of sediment transport suggest that flow acceleration may have a contribution to sediment transport. Watanabe and Sato, (2005) suggest such an improvement for sheet flow formulae. Other studies suggest a contribution to sediment mobility is caused by sediment pore-pressure variations, and flow in/exfiltration events. Karambas, (2005) suggests an improvement to the Meyer-Peter and Müller formula to account for such processes in fine sediments. Another possible contribution to the sediment model is the variation of turbulence or friction between the uprush and downrush phases.

The model still requires a full calibration against field data. Only one data set is known to the author for the sloping beach model, which is the GWK experiment of Román-Blanco and Holmes, (2003). A satisfactory shore-line is required for this.

Suitable field data for the sea wall model is also sparse. The most extensive data set is the Powell and Lowe experiment of a scaled flume discussed above. Ideally, an experiment of the magnitude of Román-Blanco and Holmes would provide such data.

7.3. Further work

Further work for the numerical model should consider the relative importance of the suggested modifications for flow turbulence and in/exfiltration. Such work may be directed to finding a suitable parameterisation, or incorporating an analytical treatment.

Further work for the numerical model should also consider an appropriate means of modelling wave breaking on reflected and standing waves.

For the sloping beach model, a robust shoreline routine needs to be found. Examples have been presented with the NLSW equations (e.g. Chadwick , 1991). There seems to be more success with these techniques in a non-conservative form however.

A suitable data set for verification remains to be identified, and a new series of experiments may well be beneficial for this. This would have the benefit of providing a consistent data set with regard to sediment size and scaling factors.

References

Abbott,M.B. and Basco,D.R., (1989) *Computational Fluid Dynamics: An Introduction for Engineers*, Longman Scientific & Technical, Harlow.

Abbott,M.B., McCowan,A.D., and Warren,I.R., (1984). "Accuracy of short wave numerical models", *Journal of Hydraulic Engineering*, **110**(10): 1287-1301.

Abbott,M.B., Petersen,H.M., and Skovgaard,O., (1978). "On the numerical modelling of short waves in shallow water", *Journal of Hydraulic Research*, **16**(3): 173-204.

Abbott,M.B. and Rodenhuis,G.S., (1972). "A numerical simulation of the undular hydraulic jump", *Journal of Hydraulic Research*, **10**(3): 239-257.

Abramowitz,M. and Stegun,I.A., (1965) *Handbook of Mathematical Functions*, Applied Mathematics Series, 55. National Bureau of Standards, US Department of Commerce, Washington, D.C., USA.

Acuña,A.P., 2005. *Concerning swahs on steep beaches*. Ph.D. Thesis, University of Plymouth, UK.

Agnon,Y., Madsen,P.A., and Schäffer,H.A., (1999). "A new approach to high-order Boussinesq models", *Journal of Fluid Mechanics*, **399**: 319-333.

Arcilla,A.S., Roelvink,J.A., O'Connor,B.A., Reniers,A., and Jimenez,J.A. (1994) "The Delta flume '93 experiment", *Proceedings of the Coastal Dynamics Conference,* UPC, Barcelona. pp488-502.

Armanini,A. and Di Silvio,G., (1988). "A one-dimensional model for the transport of a sediment mixture in non-equilibrium conditions", *Journal of Hydraulic Research*, **26**(3): 275-292.

Bagnold,R.A., (1963). "Mechanics of marine sedimentation". In: *The Sea*, M.N.Hill (Editor), Interscience, New York.

Bailard,J.A., (1981). "An energetics total load model for a plane sloping beach", *Journal Of Geophysical Research*, **86**(C11): 10938-10954.

Bailard,J.A. and Inman,D.L., (1981). "An energetics bedload model for a plane sloping beach: local transport", *Journal Of Geophysical Research*, **86**(C3): 2035-2043.

Baldock,T.E., Holmes,P., Bunker,S., and Van Weert,P., (1998). "Cross-shore hydrodynamics within an unsaturated surf zone", *Coastal Engineering*, **34**(3-4): 173-196.

Barr,B.C., Slinn,D.N., Pierro,T., and Winters,K.B., (2004). "Numerical simulation of turbulent, oscillatory flow over sand ripples", *Journal Of Geophysical Research - Oceans*, **109**(C9): C09009.

Beji,S. and Battjes,J.A., (1993). "Experimental investigations of wave propagation over a bar", *Coastal Engineering*, **19**(1-2): 151-162.

Boussinesq,J., (1872). "Théorie des ondes et des remous qui se propagent le long d'un canal rectangulaire horizontal", *Journal de Mathématique Pures et Appliquées*, **deuxiéme série, 17**: 55-108.

Bruun,P. (1954) *Coast Erosion and the Development of Beach Profiles*, Technical Memo, No. 44, U.S. Army Corps of Engineers, Beach erosion board.

Bullock,G., Obhrai,C., Muller,G., Wolters,G., and Peregrine,D.H. (2004) "Laboratory measurement of wave impacts", Ed. Melby, J. A. *Proceedings of the 3rd International Conference on Coastal Structures.*, A.S.C.E., Portland OR,USA. pp343-355.

Butt,T. and Russell,P., (1999). "Sediment transport mechanisms in high energy swash", *Marine Geology*, **161**: 361-375.

Butt,T., Russell,P., and Turner,I., (2001). "The influence of swash infiltration–exfiltration on beach face sediment transport: onshore or offshore?", *Coastal Engineering*, **42**(1): 35-52.

Chadwick,A.J., (1991). "An unsteady flow bore model for sediment transport in broken waves, Part I: The development of the numerical model", *Proceedings of the Institution of Civil Engineers, Part 2*, **91**: 719-737.

Cox,D.T., Mase,H., and Sakai,T. (1991) *An Experiment on the Effect of Fluid Acceleration on Seabed Stability*, Report 91-HY-01, Kyoto University. Japan.

Dean,R.G. (1977) *Equilibrium Beach Profiles: US Atlantic and Gulf Coasts.*, Ocean Engineering Report No. 12, University of Delaware, Department of Civil Engineering. Newark (Delaware).

DEFRA, (2003) *Beach Lowering in Front of Coastal Structures*, Report FD1916/TR1.

Dingemans,M.W., (1997) *Water waves propagation over uneven bottoms. Part 2 - Nonlinear wave propagation*, Wiley, New York.

Dodd,N., (1998). "A numerical model of wave run-up, overtopping and regeneration.", *Journal of Waterway Port Coastal and Ocean Engineering - A. S. C. E.*, **124**(2): 73-81.

Engelund,F. and Fredsøe,J., (1976). "A sediment transport model for straight alluvial channels", *Nordic Hydrology*, **7**: 293-306.

Fredsøe,J. and Deigaard,R., (1992) *Mechanics of Coastal Sediment Transport*, World Scientific Press, Singapore.

Freilich,M.H. and Guza,R.T., (1984). "Nonlinear effects on shoaling surface gravity waves", *Philosophical Transactions of the Royal Society, Series A*, **311**: 1-41.

Glaister,P. (1987) *Difference Schemes for the Shallow Water Equations.*, Vol. 9/97. Numerical Analysis Report, University of Reading.

Gobbi,M.F. and Kirby,J.T., (1999). "Wave evolution over submerged sills: tests of a high-order Boussinesq model", *Coastal Engineering*, **37**(1): 57-96.

Horn,D.P., Baldock,T.E., and Baird,A.J. (1998) "Field measurements of swash induced pressure gradients within a sandy beach", *Proceedings 26th International Conference Coastal Engineering,* A.S.C.E. pp2812-2825.

Hudson,J., Damgaard,J., Dodd,N., Chesher,T., and Cooper,A., (2005). "Numerical approaches for 1D morphodynamic modelling", *Coastal Engineering*, **52**(8): 691-707.

Hughes,S.A. and Fowler,J.E. (1991) "Wave indced scour prediction at vertical walls.", Ed. Kraus, N. C., Gingerich, K. J., and Kriebel, D. L. *Coastal Sediments '91,* A.S.C.E. pp1886-1900.

Inman,D.L. and Bowen,A.J. (1963) "Flume experiments on sand transport by waves and currents", *Proceedings of the 8th Conference on Coastal Engineering,* A.S.C.E., New York.

Irie,I. and Nadaoka,K. (1984) "Laboratory reproduction of seabed scour in front of breakwaters", *Proceedings of the 19th International Conference on Coastal Engineering,* Houston, pp1715-1731.

Karambas,Th.V. (2005) "Prediction of sediment transport in the swash zone by using a nonlinear wave model", *Coastal Engineering 2004: Proceedings of the 29th International Conference, Vol 2,* Lisbon,World Scientific, Singapore. pp1959-1970.

Karunarathna,H., Chadwick,A.J., and Lawrence,J., (2005). "Numerical experiments of swash oscillations on steep and gentle beaches", *Coastal Engineering*, **52**(6): 497-511.

Kennedy,A.B., Chen,Q., Kirby,J.T., and Dalrymple,R.A., (2000). "Boussinesq modeling of wave transformation, breaking, and runup. I: 1D", *Journal of Waterway Port Coastal and Ocean Engineering - A. S. C. E.*, **126**(1): 39-47.

Kennedy,A.B. and Fenton,J.D., (1997). "A fully-nonlinear computational method for wave propagation over topography", *Coastal Engineering*, **32**(2-3): 137-161.

Kleinhans,M.G. and van Rijn,L.C., (2002). "Stochastic Prediction of Sediment Transport in Sand-Gravel Bed Rivers", *Journal of Hydraulic Engineering*, **128**: 412-425.

Korteweg,D.J. and de Vries,G., (1895). "On the change of form of long waves advancing in a rectangular canal, and on a new type of long stationary waves.", *Philosophical Magazine*, **Series 5**(39): 422-433.

Kothe,D.B., Mjolsness,R.C., and Torrey,M.D. (1991) *Ripple: A Computer Program for Incompressible Flows with Free Surfaces.*, LA-12007-MS. Los Alamos National Laboratory Report, University of California, U.S. Dept. of Energy.

Kraus,N.C. and Smith,J.M. (1994) *SUPERTANK Laboratory Data Collection Project*, TR CERC-94-3, US Army Corps of Engineers, Waterways Experimental Station.

Kriebel,D.L. and Dean,R.G., (1985). "Numerical simulation of time-dependent beach and dune erosion", *Coastal Engineering*, **9**(3): 221-245.

Larsen,J. and Dancy,H., (1983). "Open boundaries in short wave simulations - A new approach", *Coastal Engineering*, **7**: 285-297.

Larson,M. (1988) *Quantification of beach profile change*, Report 1008, Department of Water Resources, University of Lund. Lund, Sweden.

Lawrence,J. and Chadwick,A.J., (2005). "Modelling wave reflection on sloping foreshores with sea walls", *Proceedings of the Institution of Civil Engineers - Maritime Engineering*, **158**: 15-24.

Lawrence,J., Chadwick,A.J., and Fleming,C. (2001) "A phase-resolving model of sediment transport on coarse grained beaches", Ed. Edge, B. L. *Coastal Engineering 2000, Proceedings of the 27th International Conference, Vol. 1,* Sydney, Australia,A.S.C.E. pp624-636.

Lawrence,J., Karunarathna,H., Chadwick,A.J., and Fleming,C. (2003) "Cross-shore sediment transport on mixed coarse grain sized beaches: Modeling and measurements", Ed. Smith, J. M. *Coastal Engineering 2002: Proceedings of the 28th International Conference, Vol 3,* Cardiff,World Scientific, Singapore. pp2565-2577.

Long,W., Hsu,T.-J., and Kirby,J.T. (2005) "Modeling cross-shore sediment transport processes with a time domain Boussinesq model", Ed. Smith, J. M. *Coastal Engineering 2004: Proceedings of the 29th International Conference, Vol 2,* Lisbon,World Scientific, Singapore. pp1874-1886.

Longuet-Higgins,M.S., (1953). "Mass transport in waver waves", *Philosophical Transactions of the Royal Society, Series A*, **245**(903): 535-581.

Luth,H.R., Klopman,G., and Kitou,N. (1993) *Kinematics of Waves Breaking Partially on an Offshore Bar*, H1573, Delft Hydraulics.

Madsen,P.A., Bingham,H.B., and Liu,H., (2002). "A new Boussinesq method for fully nonlinear waves from shallow to deep water", *Journal of Fluid Mechanics*, **462**: 1-30.

Madsen,P.A., Murray,R., and Sørenson,O.R., (1991). "A new form of the Boussinesq equations with improved linear dispersion characteristics", *Coastal Engineering*, **15**: 371-388.

Madsen,P.A. and Sørenson,O.R., (1992). "A new form of the Boussinesq equations with improved linear dispersion characteristics. Part 2: a slowly varying bathymetry", *Coastal Engineering*, **18**: 183-204.

Madsen,P.A., Sørenson,O.R., and Schäffer,H.A., (1997a). "Surf zone dynamics simulated by a Boussinesq type model. Part I. Model description and cross-shore motion of regular waves", *Coastal Engineering*, **32**(4): 255-287.

Madsen,P.A., Sørenson,O.R., and Schäffer,H.A., (1997b). "Surf zone dynamics simulated by a Boussinesq type model. Part II: surf beat and swash oscillations for wave groups and irregular waves", *Coastal Engineering*, **32**(4): 289-319.

Madsen,P.A. and Warren,I.R., (1984). "Performance of a numerical short-wave model", *Coastal Engineering*, **8**(1): 73-93.

Mase,H. (1994) "Uprush-backrush interaction dominated and long wave dominated swash oscillations", *Proceeding of International Symposium: Waves - Physical and Numerical Modelling,* Vancouver. pp316-325.

Masselink,G. and Li,Q., (2001). "The role of swash infiltration in determining the beachface gradient: a numerical study", *Marine Geology*, **176**: 139-156.

McCowan,A.D. (1987) "The range of application of Boussinesq type numerical short wave models", *22nd IAHR Congress,* Lausanne, pp378-384.

McDougal,W.G., Kraus,N.C., and Ajibowo,H., (1996). "The effects of seawalls on the beach: Part II, Numerical modeling of SUPERTANK seawall tests", *Journal of Coastal Research*, **12**(3): 702-213.

McDowell,D.M., (1989). "A general formula for estimation of the rate of transport of non-cohesive bed-load", *Journal of Hydraulic Research*, **27**(3): 355-361.

Mei,C.C., (1989) *The Applied Dynamics of Ocean Surface Waves*, 2nd Edition, World Scientific Press, Singapore.

Meyer-Peter,E. and Müller,R. (1948) *Formulas for Bed-load Transport*, Report of 2nd Meeting, International Association for Hydraulic and Structural Research, Stockholm.

Nielsen,P., (1992) *Coastal Bottom Boundary Layers and Sediment Transport*, World Scientific Publishing, Singapore.

Nwogu,O., (1996). "Alternative forms of Boussinesq equations for nearshore wave propagation", *Journal of Waterway Port Coastal and Ocean Engineering - A. S. C. E.*, **119**(6): 618-638.

Otta,A.K. and Acuña,A.P. (2005) "Swash boundary and cross-shore variation of horizontal velocity on a slope", *Coastal Engineering 2004: Proceedings of the 29th International Conference, Vol 2,* World Scientific, Singapore. pp1616-1628.

Ozanne,F., 1998. *Performance of a Boussinesq model for shoaling and breaking waves.* Ph.D. Thesis, University of Plymouth, UK.

Ozanne,F., Chadwick,A.J., Huntley,D.A., Simmonds,D.J., and Lawrence,J., (2000). "Velocity predictions for shoaling and breaking waves with a Boussinesq-type model", *Coastal Engineering*, **24**(1-2): 51-80.

Packwood,A.R., 1980. *Surf and run-up on Beaches.* Ph.D. Thesis, University of Bristol.

Pender,G. and Li,Q., (1995). "Comparison of two hiding function formulations for non-uniform sediment transport calculations", *Proceedings of the Institution of Civil Engineers - Water, Maritime & Energy*, **112**: 127-135.

Pender,G. and Li,Q., (1996). "Numerical prediction of graded sediment transport", *Proceedings of the Institution of Civil Engineers - Water, Maritime & Energy*, **118**: 237-245.

Peregrine,D.H., (1967). "Long waves on a beach", *Journal of Fluid Mechanics*, **27**(4): 815-827.

Powell,K. and Lowe,J.P. (1994) "The scouring of sediments at the toe of sea walls", *Proceedings of the Hornafjordor International Coastal Symposium,* Iceland.

Powell,K. and Whitehouse,R.J.S. (1998) "The occurrence and prediction of scour at coastal and estuarine structures.", *33rd MAFF conference of River and Coastal Engineers,* Keele University, UK.

Rahman,M., (1995) *Water Waves: Relating Modern Theory to Advanced Engineering Applications*, Clarendon Press, Oxford.

Rakha,K.A., Deigaard,R., and Brøker,I., (1997). "A phase-resolving cross shore sediment transport model for beach profile evolution.", *Coastal Engineering*, **31**: 231-261.

Rakha,K.A. and Kamphuis,J.W., (1997). "A morphology model for an eroding beach backed by a seawall.", *Coastal Engineering*, **30**: 53-75.

Roelvink,J.A. and Brøker,I., (1993). "Cross-shore profile models", *Coastal Engineering*, **21**(1-3): 163-191.

Román-Blanco,B.L.d.S. and Holmes,P. (2003) "Further insight on behaviour of mixed snad and gravel beaches - Large scale experiments on profile development", Ed. Smith, J. M. *Coastal Engineering 2002: Proceedings of the 28th International Conference, Vol 3,* Cardiff,World Scientific, Singapore. pp2651-2663.

Russell,R.C.H. and Inglis,C. (1953) *The influence of a vertical wall on a beach in front of it*, Hydraulics Research Station. Wallingford.

Schäffer,H.A., Madsen,P.A., and Deigaard,R., (1993). "A Boussinesq model for waves breaking in shallow water", *Coastal Engineering*, **20**: 185-202.

Shields,A. (1936) *Anwendung der Ähnlichkeitsmechanik und der Turbulenzforschung auf die Geschiebebewegung.* Mitteilungen der Preußischen Versuchsanstalt für Wasserbau und Schiffbau, Berlin.

Soulsby,R., (1997) *Dynamics of Marine Sands: A Manual for Practical Applications*, Thomas Telford Publications, London.

Soulsby,R. and Whitehouse,R.J.S. (1997) "Threshold of sediment motion in coastal environments", *Proceedings of Pacific Coasts and Ports '97 Conference, Centre for Advanced Engineering,* Christchurch, NZ. pp149-154.

Stive,M.J.F. (1980) "Velocity and pressure field of spilling breakers", *Proceedings of the 17th Coastal Engineering Conference,* pp547-566.

Swart,D.H. (1974) *Offshore sediment transport and equilibrium beach profiles.* Publication 131, Delft Hydraulics Laboratory.

Ting,F.C.K. and Kirby,J.T., (1994). "Observation of undertow and turbulence in a laboratory surf zone", *Coastal Engineering*, **24**(1-2): 51-80.

van Rijn,L.C., (1984). "Sediment Transport, Part1: Bedload Transport", *Journal of the Hydraulics Division, Proceedings of the A. S. C. E.*, **110**(HY10): 1431-1456.

van Rijn,L.C., (1993) *Principles of Sediment Transport in Rivers, Estuaries and Coastal Seas*, Aqua Publications, Amsterdam.

Watanabe,A. and Sato,S. (2005) "A sheet-flow transport rate formula for asymmetric, forward-leaning waves and currents", *Coastal Engineering 2004: Proceedings of the 29th International Conference, Vol 2,* World Scientific, Singapore. pp1703-1714.

Wei,G. and Kirby,J.T., (1995). "Time-dependent numerical code for extended Boussinesq equations", *Journal of Waterway Port Coastal and Ocean Engineering - A. S. C. E.*, **121**(5): 251-261.

Wei,G., Kirby,J.T., Grilli,S.T., and Subramanya,R., (1995). "A fully nonlinear Boussinesq model for surface waves. I. Highly nonlinear, unsteady waves", *Journal of Fluid Mechanics*, **294**: 71-92.

Whalin,R.W. (1971) *The limit of applicability of linear wave refraction theory in a convergence zone*, H-71-3, U.S. Army Corps of Engineers, Waterways Expeimental Station, Vicksburg MS, USA.

Witting,J.M., (1984). "A unified model for the evolution of nonlinear water-waves", *Journal of Computational Physics*, **56**(2): 203-236.

Xie,S., (1985). "Scouring patterns in front of vertical breakwaters", *Acta Oceanologica Sinica*, 4(1): 153-164.

Zhang,J.E., 1996. *I. Run-up of ocean waves on beaches.* Ph.D. Thesis, California Institute of Technology.

A. Appendix

A.1. Cnoidal wave theory

Unlike the NLSW equations, the Boussinesq equations have a permanent wave solution. Rahman, (1995), describes the following process. It is convenient to transform the Boussinesq equations (Equations 18) by applying $P = u.d = u(h+\eta)$ which gives the following set of equations:

$$\frac{\partial \eta}{\partial t} + (h+\eta)\frac{\partial u}{\partial x} = 0$$
$$\frac{\partial u}{\partial t} + u\frac{\partial u}{\partial x} + g\frac{\partial \eta}{\partial x} - \frac{h^2}{3}\frac{\partial^3 u}{\partial x^2 \partial t} = 0 \qquad \text{(A1)}$$

These in turn may be non-dimensionalised by taking a series of scalings:

$$\left.\begin{aligned} X &= kx \\ T &= kCt \\ h &= a.h' \\ u &= \frac{a}{h}Cu' \\ \text{where } C^2 &= g.h \end{aligned}\right\} \qquad \text{(A2)}$$

where $k = 2\pi/L$ is the wave number and $C^2 = gh$ is the wave celerity squared. h', u' are scaled water depth and velocity , which results in the following formulae:

$$\frac{\partial \eta'}{\partial T} + \frac{\partial}{\partial X}((1+\varepsilon\eta')u') = 0$$
$$\frac{\partial u'}{\partial T} + \varepsilon u'\frac{\partial u'}{\partial X} + \frac{\partial \eta'}{\partial X} - \frac{\gamma^2}{3}\frac{\partial^3 u'}{\partial X^2 \partial T} = 0 \qquad \text{(A3)}$$

where η' is the scaled elevation, $\varepsilon = A/h$ and $\gamma = k.h$. ε is the same as in Equation 4, and γ is related to the μ of Equation 5 by $\gamma^2 = 4\pi^2\mu$.

Substituting $u' = \partial\phi/\partial X$ (i.e. describing u' with a velocity potential), and eliminating η', a single equation for ϕ may be obtained:

$$\frac{\partial^2\phi}{\partial T^2}-\frac{\partial^2\phi}{\partial X^2}=\frac{\gamma^2}{3}\frac{\partial^4\phi}{\partial X^2\partial T^2}-\varepsilon\frac{\partial}{\partial T}\left[\left(\frac{\partial\phi}{\partial X}\right)^2+\frac{1}{2}\left(\frac{\partial\phi}{\partial T}\right)^2\right]=0 \tag{A4}$$

For a progressive wave, a solution is sought of the form $\phi=f(\zeta)$ where $\zeta=X-cT$. Substituting for ϕ in the above, the following ordinary differential equation is obtained (using a subscript notation to denote differentiation thus $\frac{\partial\Psi}{\partial\xi}\equiv\Psi_\xi$)

$$(c^2-1)f_{\zeta\zeta}=\frac{\gamma^2}{3}c^2f_{\zeta\zeta\zeta\zeta}+\varepsilon.c\left(1+\frac{c^2}{2}\right)\left(f_\zeta^2\right)_\zeta=0 \tag{A5}$$

This equation implies c = 1+O(ε,γ^2), so terms in c on the RHS may be approximated by 1. This equation may then be integrated to yield the following:

$$(c^2-1)f_\zeta+A_1=\frac{\gamma^2}{3}f_{\zeta\zeta\zeta}+\varepsilon\left(\frac{3}{2}\right)\left(f_\zeta^2\right)=0 \tag{A6}$$

The substitution $\eta'=-f_T=f_\zeta$ may now be made. For clarity however, the dash will however be omitted until Equation A19. The equation becomes:

$$(c^2-1)\eta+A_1=\frac{\gamma^2}{3}\eta_{\zeta\zeta}+\varepsilon\left(\frac{3}{2}\right)\left(\eta^2\right)=0 \tag{A7}$$

This may be multiplied by η_ζ and integrated again to yield:

$$(c^2-1)\frac{\eta^2}{2}+A_1\eta+A_2-\varepsilon\left(\frac{3}{2}\right)\left(\eta^3\right)=\frac{\gamma^2}{6}\eta_\zeta^2 \tag{A8}$$

or

$$-\eta^3+\frac{(c^2-1)}{\varepsilon}\eta^2+B_1\eta+B_2=\frac{\gamma^2}{3\varepsilon}\eta_\zeta^2 \tag{A9}$$

noting the change in the integration constants. The LHS of this is simply a cubic polynomial in η, so the equation may be represented as

$$\begin{aligned}(\eta-\eta_1)(\eta-\eta_2)(\eta_3-\eta) &=\frac{\gamma^2}{3\varepsilon}\eta_\zeta^2\\ &=P_3(\eta)\end{aligned} \tag{A10}$$

Since ε, γ and η' are always real, the RHS of this always positive or zero. Accordingly, η_1, η_2, η_3 may be chosen such that $\eta_3 > \eta_2 > \eta_1$, noting the sign of η_3. A general sketch of the cubic is show in Figure A1. It can be seen that η must lie between η_2 and η_3, inferring that $\eta_3 - \eta_2$ is in fact the wave height.

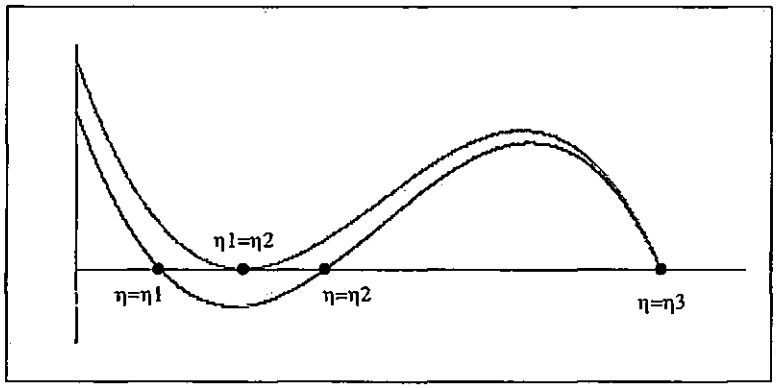

Figure A1 Roots of cubic equation

To find the expression for η, the substitution

$$\eta = \eta_3 \cos^2\theta + \eta_2 \sin^2\theta$$
$$\theta = \theta(\zeta) \tag{A11}$$

is made, leading to:

$$\eta_\zeta = (\eta_3 - \eta_2)(-2\cos\theta\sin\theta)\theta_\zeta \tag{A12}$$

Substituting Equations A11 and A12 into Equation A10 yields:

$$\begin{aligned} 4\theta_\zeta^{\,2}(\eta_3-\eta_2)^2(\cos^2\theta\sin^2\theta) &= \frac{3\varepsilon}{\gamma^2}\left(\eta_3\cos^2\theta+\eta_2\sin^2\theta-\eta_1\right) \\ &\left(\eta_3\cos^2\theta+\eta_2\sin^2\theta-\eta_2\right)\left(\eta_3-\eta_3\cos^2\theta+\eta_2\sin^2\theta\right) \\ &= \frac{3\varepsilon}{\gamma^2}\left((\eta_3-\eta_1)-(\eta_3-\eta_2)\sin^2\theta\right)(\eta_3-\eta_2)\cos^2\theta.(\eta_3-\eta_2)\sin^2\theta \end{aligned} \tag{A13}$$

Cancelling common factors, and defining $m=(\eta_3-\eta_2)/(\eta_3-\eta_1)$ yields:

$$\theta_\zeta^{\,2} = \frac{3\varepsilon}{4\gamma^2}(\eta_3-\eta_1)(1-m\sin^2\theta) \tag{A14}$$

Since $\eta_2 > \eta_1$, $1 > m > 0$. This expression may be solved by a separation of variables, and leads to an *incomplete elliptic integral of the first kind.* (Abramowitz and Stegun,1965)

$$\int_0^{\theta} \frac{d\theta'}{\left(1-m\sin^2\theta'\right)^{1/2}} = \pm\frac{(3\varepsilon)^{1/2}}{2\gamma}(\eta_3-\eta_1)^{1/2}(\zeta-\zeta_0) \tag{A15}$$

This equation arises in the calculus of elliptic equations, and may be solved using elliptic theory. For

$$\xi = \mathrm{F}(\psi, m) = \int_0^{\psi} \frac{d\sigma}{\left(1-m\sin^2\sigma\right)^{1/2}}, \tag{A16}$$

define

$$\psi = \mathrm{F}^{-1}(\xi, m) = \mathrm{am}(\xi, m) \tag{A17}$$

'am' is known as the *Jacobi amplitude*, and 'm' is the *modulus*. Furthermore

$$\left.\begin{aligned}\sin(\psi) &= \sin(\mathrm{am}(\xi,m)) \equiv \mathrm{Sn}(\xi,m)\\ \cos(\psi) &= \cos(\mathrm{am}(\xi,m)) \equiv \mathrm{Cn}(\xi,m)\end{aligned}\right\} \tag{A18}$$

where 'Sn, Cn' are the *Jacobi elliptic* functions. These functions are clearly periodic. The period is in fact $4K$ where $K = K(m) = F(\pi/2,m)$ is known as the *complete elliptic integral of the first kind.* Also $\mathrm{Sn}^2(u) + \mathrm{Cn}^2(u) = 1$.

For the Boussinesq equations then, Equation A15 is solved to give

$$\theta = \mathrm{am}\left(\frac{(3\varepsilon)^{1/2}}{2\gamma}(\eta_3-\eta_1)^{1/2}(\zeta-\zeta_0), m\right) \tag{A19}$$

This may be substituted into Equation A11 and the following is obtained (reverting now to η' notation):

$$\eta' = \eta_2' + (\eta_3'-\eta_2')\,\mathrm{Cn}^2\left(\frac{(3\varepsilon)^{1/2}}{2\gamma}(\eta_3'-\eta_1')^{1/2}(\zeta-\zeta_0), m\right) \tag{A20}$$

$\eta'_3 - \eta'_2$ is the wave height, H, but η'_1 and m are still to be determined.

Since the Cn function is periodic, it can be seen that the wavelength of the non-dimensional formulation is given by

$$\frac{(3\varepsilon)^{1/2}}{2\gamma}(\eta_3'-\eta_1')^{1/2}\lambda' = 2\mathrm{K}(m)$$
$$\Rightarrow \lambda' = \frac{4\gamma\,\mathrm{K}(m)}{[(3\varepsilon)(\eta_3'-\eta_1')]^{1/2}} \tag{A21}$$

Over a wavelength, since η' is the perturbation of fluid depth from the mean, it is known that

$$\int_0^{\lambda'} \eta' d\zeta = 0 \tag{A22}$$

Substituting from Equation A11 gives

$$\int_0^{\pi} \left(\eta_3' \cos^2\theta + \eta_2' \sin^2\theta\right)\frac{d\zeta}{d\theta}d\theta = 0 \tag{A23}$$

By using symmetry of the *sin* function, this can be rewritten as

$$\int_0^{\pi/2} \frac{\eta_1' + (\eta_3'-\eta_1')(1-m\sin^2\theta)}{(1-m\sin^2\theta)^{1/2}}d\theta = 0 \tag{A24}$$

However,

$$\int_0^{\pi/2} (1-m\sin^2\theta)d\theta = \mathrm{E}(m) \tag{A25}$$

is simply the *complete elliptic integral of the second kind*, (Abramowitz and Stegun,1965) so Equation A24 may be written as

$$\eta_1'\,\mathrm{K}(m) + (\eta_3'-\eta_1')\,\mathrm{E}(m) = 0 \tag{A26}$$

and so

$$\eta_1' = -(\eta_3'-\eta_1')\frac{\mathrm{E}(m)}{\mathrm{K}(m)} = -\frac{(\eta_3'-\eta_2')}{m}\frac{\mathrm{E}(m)}{\mathrm{K}(m)} = -\frac{H}{m}\frac{\mathrm{E}(m)}{\mathrm{K}(m)} \tag{A27}$$

This may be substituted into Equation A21 to give.

$$\lambda' = \frac{4\gamma\,\mathrm{K}(m)}{(3\varepsilon)^{1/2}}\left(\frac{m}{H}\right)^{1/2} \tag{A28}$$

Substituting also back into Equation A26,

$$\eta_3' = -\eta_1'\left(\frac{\mathrm{K}(m)}{\mathrm{E}(m)} - 1\right) = \frac{H}{m}\left(1 - \frac{\mathrm{E}(m)}{\mathrm{K}(m)}\right) \tag{A29}$$

and also it can be found that

$$\eta_2' = \eta_3' - H = \frac{H}{m}\left(1 - \frac{\mathrm{E}(m)}{\mathrm{K}(m)}\right) - H = \frac{H}{m}\left(1 - m - \frac{\mathrm{E}(m)}{\mathrm{K}(m)}\right) \tag{A30}$$

Equation A9 gives an expression for c which can be restated as

$$c^2 = 1 + \varepsilon(\eta_1' + \eta_2' + \eta_2') \tag{A31}$$

and now substituting into Equations A27, A29, A30 yields

$$c^2 = 1 + \varepsilon\frac{H}{m}\left(2 - m - \frac{3\,\mathrm{E}(m)}{\mathrm{K}(m)}\right) \tag{A32}$$

Knowing c and λ', the dimensionless wave period p' can also be found:

$$p' = \frac{\lambda'}{c} = \frac{\dfrac{4\gamma}{(3\varepsilon)^{1/2}}\left(\dfrac{m}{H}\right)^{1/2}}{\left[1 + \varepsilon\dfrac{H}{m}\left(2 - m - \dfrac{3\,\mathrm{E}(m)}{\mathrm{K}(m)}\right)\right]^{1/2}} \tag{A33}$$

Reversing the scaling of Equation A2 can now recover the physical forms of these equations.

Equation A20 in physical dimensions has the form:

$$\begin{aligned}\eta &= \eta_2 + (\eta_3 - \eta_2)\,\mathrm{Cn}^2\left(\frac{\sqrt{3}}{2}\frac{(\eta_3 - \eta_1)^{1/2}}{h^{3/2}}(x - ct), m\right) \\ &= \eta_2 + H\,\mathrm{Cn}^2\left(\frac{2K}{\lambda}(x - ct), m\right)\end{aligned} \tag{A34}$$

The wavelength is now

$$\lambda = 4\,\mathrm{K}(m)H\left[\frac{mh}{3H}\right]^{1/2} \tag{A35}$$

The celerity is given by

$$c^2 = gh\left[1 + \frac{H}{h}\frac{1}{m}\left(2 - m - \frac{3\,\mathrm{E}(m)}{\mathrm{K}(m)}\right)\right] \tag{A36}$$

and lastly the period may be written as

$$T=\left(\frac{h}{g}\right)^{1/2}\frac{4\mathrm{K}(m)(mh/3H)^{1/2}}{\left[1+\frac{H}{h}\frac{1}{m}\left(2-m-\frac{3\mathrm{E}(m)}{\mathrm{K}(m)}\right)\right]} \tag{A37}$$

Equation A35 relates λ,h,H and m. In practice, m must be found using an iterative method to satisfy this equation, given the wave case of interest. The necessary elliptic integral evaluations are available in software such as MATLAB and MAPLE. Considering Equation A36, the RHS of this equation will be negative for the range $0 < m < m_{LIM}$ for some $m_{LIM} < 1$. Accordingly, m must be sufficiently large (or the wavelength must be sufficiently long) for the celerity equation to have a real solution. Another consequence of this equation is that wave celerity is now a function of wave height, water depth and wavelength.

Considering the case of $m \to 0$. Then $H = \eta_3-\eta_2 \to 0$, and $c^2 \to gh$. Also, $\mathrm{Cn}(u,0) = \cos(u)$, and $\mathrm{K}(0)=\pi/2$. Therefore Equation A34 reduces to:

$$\eta = \eta_2 + H\cos^2\left(\frac{\pi}{\lambda}(x-ct)\right) \tag{A38}$$

which, since η_2 = -a = -H/2, may be written:

$$\eta = \frac{H}{2}\cos\left(\frac{2\pi}{\lambda}(x-ct)\right) \tag{A39}$$

and the waveform is the linearised sinusoidal wave with wavespeed c=√(gh) and amplitude $H/2$.

A.2. Cnoidal wave reflection

Left and right travelling linear waves may be combined to form the well known standing wave solution. Similar behaviour for a Cnoidal wave may also found. The following is developed in Mei (1989).

Considering again Equation A4:

$$\frac{\partial^2\phi}{\partial T^2}-\frac{\partial^2\phi}{\partial X^2}=\frac{\gamma^2}{3}\frac{\partial^4\phi}{\partial X^2\partial T^2}-\varepsilon\frac{\partial}{\partial T}\left[\left(\frac{\partial\phi}{\partial X}\right)^2+\frac{1}{2}\left(\frac{\partial\phi}{\partial T}\right)^2\right]=0 \tag{A40}$$

Firstly, introduce the change of scale $\tau = \varepsilon T$, $\sigma = X - T$. $1/\varepsilon$ is the (dimension-less) scale of time variation. The equation may now be rewritten as

$$(\phi_\sigma)_\tau + \frac{3}{4}(\phi_\sigma{}^2)_\sigma + \frac{\gamma^2}{6\varepsilon}\phi_{\sigma\sigma\sigma} = O(\varepsilon, \gamma^2) \tag{A41}$$

Seeking a potential flow solution for this, ϕ_t may be replaced by ζ, and this may now be written as:

$$\zeta_\tau + \frac{3}{2}\zeta\zeta_\sigma + \frac{\gamma^2}{6\varepsilon}\zeta_{\sigma\sigma\sigma} \cong 0 \tag{A42}$$

This is the well known Korteweg-de Vries equation. Since the Cnoidal wave is a solution of Equation A4, it must also be a solution of the Korteweg de-Vries equation.

Still considering Equation A4, a solution of the form $\Phi = \phi^{(0)}(x,t;\tau) + \varepsilon\phi^{(1)}(x,t;\tau)$ is sought. This leads to the equations:

$$\phi^{(0)}_{tt} - \phi^{(0)}_{xx} = 0 \tag{A43}$$

$$\phi^{(1)}_{tt} - \phi^{(1)}_{xx} = \frac{1}{3}\frac{\gamma^2}{\varepsilon}\phi^{(0)}_{xxtt} - \left[\left(\phi^{(0)}_x\right)^2 + \frac{1}{2}\left(\phi^{(0)}_t\right)^2\right]_t - 2\phi^{(0)}_{tt} \tag{A44}$$

Equation A43, being the wave equation has a general solution of

$$\phi^{(0)} = \phi^+(\sigma^+;\tau) + \phi^-(\sigma^-;\tau) \tag{A45}$$

for $\sigma^+ = X - T$, $\sigma^- = X + T$. These are the low order left and right waves of the solution.

Equation A44 may be expanded in terms of $\phi^{(0)}$, and becomes

$$\begin{aligned} -4\frac{\partial^2\phi^{(1)}}{\partial\sigma^+\partial\sigma^-} = \; & 2\frac{\partial}{\partial\tau}\frac{\partial\phi^+}{\partial\sigma^+} + 3\frac{\partial\phi^+}{\partial\sigma^+}\frac{\partial^2\phi^+}{\partial\sigma^{+2}} + \frac{1}{3}\frac{\gamma^2}{\varepsilon}\frac{\partial^4\phi^+}{\partial\sigma^{+4}} \\ & -2\frac{\partial}{\partial\tau}\frac{\partial\phi^-}{\partial\sigma^-} - 3\frac{\partial\phi^-}{\partial\sigma^-}\frac{\partial^2\phi^-}{\partial\sigma^{-2}} - \frac{1}{3}\frac{\gamma^2}{\varepsilon}\frac{\partial^4\phi^-}{\partial\sigma^{-4}} \\ & +\frac{\partial^2\phi^+}{\partial\sigma^{+2}}\frac{\partial\phi^-}{\partial\sigma^-} - \frac{\partial^2\phi^-}{\partial\sigma^{-2}}\frac{\partial\phi^+}{\partial\sigma^+} \end{aligned} \tag{A46}$$

It is required that the solution for this does not grow linearly for σ^+ or σ^-. Such a solution is found if the first and second lines of Equation A46 are zero independently. That is to say:

$$\frac{\partial}{\partial\tau}\frac{\partial\phi^+}{\partial\sigma^+}+\frac{3}{2}\frac{\partial\phi^+}{\partial\sigma^+}\frac{\partial^2\phi^+}{\partial\sigma^{+2}}+\frac{1}{6}\frac{\gamma^2}{\varepsilon}\frac{\partial^4\phi^+}{\partial\sigma^{+4}}=0$$
$$\frac{\partial}{\partial\tau}\frac{\partial\phi^-}{\partial\sigma^-}+\frac{3}{2}\frac{\partial\phi^-}{\partial\sigma^-}\frac{\partial^2\phi^-}{\partial\sigma^{-2}}+\frac{1}{6}\frac{\gamma^2}{\varepsilon}\frac{\partial^4\phi^-}{\partial\sigma^{-4}}=0 \qquad \text{(A47)}$$

Now applying $\zeta^+=-\phi^+_t=\phi^+_{\sigma+}$ and $\zeta^-=-\phi^-_t=\phi^-_{\sigma-}$, the set of equations

$$\frac{\partial\zeta^+}{\partial\tau}+\frac{3}{2}\zeta^+\frac{\partial\zeta^+}{\partial\sigma^+}+\frac{1}{6}\frac{\gamma^2}{\varepsilon}\frac{\partial^3\zeta^+}{\partial\sigma^{+3}}=0$$
$$\frac{\partial\zeta^-}{\partial\tau}+\frac{3}{2}\zeta^-\frac{\partial\zeta^-}{\partial\sigma^-}+\frac{1}{6}\frac{\gamma^2}{\varepsilon}\frac{\partial^3\zeta^-}{\partial\sigma^{-3}}=0. \qquad \text{(A48)}$$

is obtained, showing that each wave separately satisfies the Korteweg-de Vries equation. The wave $\zeta^{(0)}=\zeta^+(\sigma^+;\tau)+\zeta(\sigma^-;\tau)$ may therefore be constructed by superposition, which is accurate again to the leading order.

Considering a wave tank in the domain $0 < X < \pi$, the elevation solution given by

$$\zeta^+=F(-\sigma^+;t),\ \zeta^-=F(\sigma^-,\tau), \qquad \text{(A49)}$$

has the corresponding velocity solution

$$u(0)=-F(-\sigma^+;t)+F(\sigma^-,\tau). \qquad \text{(A50)}$$

Since the wave reflects at the tank wall, the solution requires that $u^{(0)}$ vanishes at $X=\pi$, or $-F(t-\pi;\tau)+F(t+\pi;\tau)=0$. This is satisfied when F is periodic in σ (or X) with a period of 2π. The Cnoidal wave of unit height satisifies these requirements, and in the form of Equation A20 may be written:

$$F=f_2+(f_3-f_2)\,\mathrm{Cn}^2\left(\frac{(3\varepsilon)^{1/2}}{2\gamma}(f_3-f_1)^{1/2}(\sigma+\Omega t),m\right) \qquad \text{(A51)}$$

Comparing with Equations A27, A28 it is found that

$$f_1=-\frac{\mathrm{E}(m)}{m\,\mathrm{K}(m)}, \text{ and} \qquad \text{(A52)}$$

$$\Omega=-\frac{1}{m}\left(1-\frac{3}{2}\frac{\mathrm{E}(m)}{\mathrm{K}(m)}\right)-\frac{1}{2}, \text{ and} \qquad \text{(A53)}$$

$$2\pi = \frac{4\gamma \mathrm{K}(m)}{(3\varepsilon)}(m)^{1/2}$$
$$\Rightarrow \frac{\varepsilon}{\gamma^2} = \frac{4m\mathrm{K}(m)^2}{3\pi^2} \qquad \text{(A54)}$$

Since this formulation is in dimensionless units, a reverse scaling must again be applied. Knowing the Ursell number

$$\frac{\varepsilon}{\gamma^2} = \frac{A}{h}\left(\frac{L}{h}\right)^2 \frac{1}{\pi^2}, \qquad \text{(A55)}$$

Equation A53 may be used to find Ω, and Equation A54 to find m.